DEVELOPMENT OF COMPUTER-BASED FIRST-PRINCIPLES KINETIC MODELS FOR AQUEOUS PHASE ADVANCED OXIDATION PROCESSES

A Thesis
Presented to
The Academic Faculty

by

Xin Guo

In Partial Fulfillment
of the Requirements for the Degree
Doctor of Philosophy in the
School of Civil and Environmental Engineering

Georgia Institute of Technology
August 2015

DEVELOPMENT OF COMPUTER-BASED FIRST-PRINCIPLES KINETIC MODELS FOR AQUEOUS PHASE ADVANCED OXIDATION PROCESSES

Approved by:

Dr. John C. Crittenden, Advisor
School of Civil and Environmental Engineering
Georgia Institute of Technology

Dr. Sotira Yiacoumi
School of Civil and Environmental Engineering
Georgia Institute of Technology

Dr. Yongsheng Chen
School of Civil and Environmental Engineering
Georgia Institute of Technology

Dr. Yuhang Wang
Earth and Atmospheric Sciences
Georgia Institute of Technology

Dr. Ching-Hua Huang
School of Civil and Environmental Engineering
Georgia Institute of Technology

Date Approved: April 29, 2015

ACKNOWLEDGEMENTS

First of all, I would like to thank my adviser, Dr. John C. Crittenden, very much for his long-term support, professional guidance, and belief in my abilities. I would also like to thank other committee members at Georgia Tech: Dr. Yongsheng Chen, Dr. Ching-Hua Huang, Dr. Sotira Yiacoumi, and Dr. Yuhang Wang for their continuous encouragement and supports.

My appreciation extends to the IT support from CEE IT services from Georgia Tech: Winston Yang. Following individuals helped me with my research, computer skill development, and career schedule: Dr. Daisuke Minakata from Michigan Technological University for his suggestion and guidance on my research; Wei Cai and Hai Shang from Google Inc. and Xian Qin from McKinsey & Company for their technical advices, supports, and their friendship.

I appreciate faculty, students, and staff at Brook Bayer Institute of Sustainable Systems encouraged me and helped me with business prospect: Dr. Michael Chang, Dr. Arka Pandit, Jean-Ann James, Liz Minne, Chen Chen, Xuewei Yu, Martha Lindsay, and Susan Ryan. I would also express my great appreciation to my friends at Georgia Tech: Dr. Zhongming Lu, Yuzhong Zhang, Ziyi Jiang, Xiaofei Zeng, Xinxin Zhai, Yufei Zou.

I would like to acknowledge the following foundations, institutes and assistantships for their funding supports: National Science Foundation; Brook Bayer Institute of Sustainable Systems; and High Tower Chair and Georgia Research Alliance at Georgia Tech.

My deepest gratitude goes to my family: my mother, father, sister, brother, uncle, aunt, and grandparents. My parents and family always supports my decision and encourages me to move forward.

TABLE OF CONTENTS

LIST OF TABLES

LIST OF FIGURES

LIST OF ABBREVIATIONS

AOP	Advanced Oxidation Process
ChV	Chronic Toxicity Value
DCA	Dichloroacetic Acid
DIC	Direct Interaction Coefficients
DRG	Directed Relation Graph
GCM	Group Contribution Method
MCA	Monochloroacetic Acid
MTBE	Methy Tert-butyl Ether
ODE	Ordinary Differential Equation
RT	Relative Toxicity
SD	Sample Deviation
TCE	Trichloroethylene
PEG	Polyethylene Glycol
TOC	Total Organic Carbon
KMC	Kinetic Monte Carlo
MWD	Molecular Weight Distribution
LMWP	Low Molecular Weight Product
EG	Ethyleneglycol
PDI	Polydispersitivity

SUMMARY

Advanced oxidation processes (AOPs) are attractive technologies to remove organic compounds in water. AOPs produces highly reactive hydroxyl radicals that can react with organic contaminants and further degrade these compounds with the radical initiated chain reactions. These chain reactions are very complicated and various intermediates and byproducts are produced during the degradation processes. These intermediates and byproducts are of great concern since they may have adverse effect on human health. So there is need to have a detailed and quantitative insight into the degradation mechanisms and fates of intermediates and byproducts of organic compounds in AOPs.

A number of studies have investigated the degradation mechanisms of organic compounds in AOPs. However, these studies have the following limitations: first, these studies conduct experiments to determine the degradation mechanisms, which are extreme time consuming and prohibitive to be applied for all organic contaminants in water; second, the degradation mechanisms that are proposed in these studies contain lumped reactions, which can prevent us from obtaining detailed insight into the degradation process; third, the kinetic models developed in these studies are required to solve ordinary differential equations, which might be too stiff to be solved for complicated degradation mechanisms.

In this study, several computer-based first-principles kinetic models have been developed to overcome the above limitations. These computer-based first-principles kinetic models can automatically predict the degradation mechanisms for given parent compounds in aqueous phase AOPs and calculate the concentration profiles of all species

involved in the degradation mechanisms. To be specific, we developed a computer-based first-principles kinetic model with ODE solver, which can successfully simulate the degradation process for small parent compounds. We also developed a computer-based kinetic Monte Carlo (KMC) model that can solve the generated pathway without solving ODEs. Hence, the difficulty of stiffness encountered by traditional ODE based kinetic models can be avoided. This KMC model can successfully simulate the degradation processes of both small and large parent compounds. Last, we developed an on-the-fly KMC model that can have improved computational efficiency as compared with the KMC model. Our approach is sufficiently general to be applied to a wide range of contaminants.

CHAPTER 1

INTRODUCTION

1.1 Significance and Objectives

Advanced oxidation processes (AOPs) are effective technologies for destroying toxic organic contaminants in water. AOPs produce hydroxyl radicals at room temperature and pressure. These hydroxyl radicals initially react with organic compounds and further mineralize these compounds into carbon dioxide and water with the radical-initiated chain reactions. These chain reactions are mechanistically complex. As a result, various intermediates and byproducts are produced. Some of these intermediates and byproducts (e.g., volatile acids, such as acetic or formic acids) have smaller second order reaction rate constants with hydroxyl radicals than parent compounds. Accordingly, these compounds require extra time to be destroyed. In addition, some of these intermediates and byproducts may pose potential risks to human health (Rosenfeldt et al., 2004; Huber et al., 2003). Consequently, there is a need for detailed understanding of the degradation mechanisms and the fates of intermediates and byproducts produced during AOPs.

A number of studies have investigated the degradation mechanisms for both small compounds and large contaminants during AOPs. For example, the degradation mechanisms of trichloroethylene (TCE) (Li et al., 2007), acetone (Stefan et al., 1996; Stefan et al., 1999), 1,4-dioxane (Stefan et al., 1998), methy tert-butyl ether (MTBE) (Stefan et al., 2000; Cooper et al., 2009), poly(ethylene glycol) (PEG) (Santos et al;., 2009), polyacrylamide (Vijayalakshmi et al., 2009), polyvinyl alcohol (Lin et al., 2013), poly(acrylic acid) (Ulanski et al., 1995), and poly(vinyl methyl ether) (Janik et al., 2000)

in AOPs have been studied. In addition, kinetic models for the degradation of TCE (Li et al., 2007), acetone (Stefan et al., 1999), and PEG (Ghafoori et al., 2012) have also been developed. Although these studies have shed light on the degradation mechanisms during AOPs, they are limited in the following aspects. First, experimental studies that propose degradation mechanisms are time consuming and would be cost prohibitive for the huge number of compounds that are used in commerce (Richardson, 2009). Second, some studies just propose degradation mechanisms but do not develop kinetic models to predict the degradation process (Stefan et al., 1998; Stefan et al., 2000; Cooper et al.,, 2009; Vijayalakshmi et al., 2009; Lin et al., 2013; Ulanski et al., 1995; Janik et al., 2000). Other studies have developed kinetic models but used lumped reactions for simplification (Li et al., 2007; Stefan et al., 1999; Ghafoori et al., 2012). Both of these two kinds of studies might prevent us from gaining quantitative insight into detailed degradation processes of important byproducts and intermediates produced during AOPs. Third, all of the kinetic models that are mentioned above require numerical algorithms to solve ordinary differential equations (ODEs), which might be too stiff to be solved for complicated mechanisms (Vinu et al., 2012). For example, the degradation mechanism of PEG in UV/H_2O_2 process includes 522,057 species and 696,183 reactions, which might not be solved by most of the ODE solvers (Guo et al., 2014b).

Computer-based first-principles kinetic model is an attractive method to overcome the above limitations. This model is able to automatically predict the reaction mechanisms for given parent compounds based on the known reaction rules discovered from the past experimental observations. This model can also calculate the concentration profiles of all species involved in the reaction process without any data fitting. The idea

of computer-based first principles kinetic model has been successfully applied in various areas, including gas phase combustion (Van Geem et al., 2006), atmosphere chemistry (Khan et al., 2009), lubricant chemistry (Pfaendtner et al., 2008), and pyrolysis (Broadbelt et al., 1994). However, as far as the authors know, no one has developed computer-based first-principles kinetic model for AOPs.

Recent years, several useful computer tools have been developed to study the degradation mechanism and fates of intermediates and byproducts for aqueous phase AOPs. Li et al. (Li et al., 2009) has developed a pathway generator, which can automatically predict the degradation pathway for given parent compounds in AOPs based on pre-defined reaction rules, including hydrogen-atom abstraction reaction from a C-H bond or O-H bond, HO• addition reaction to a C=C bond of an aliphatic compound, oxygen addition reaction to organic radicals, bimolecular decay of peroxyl radical reaction, HO_2• elimination reaction, β scission reaction, 1,2-H shift reaction, hydrolysis reaction and so forth. The implementation of the pathway generator is based on graph theory: the species are represented as graphs and the reaction rules are represented as the manipulation of graphs. The pathway generator algorithms check the reaction potential of each species according to the reaction rules. Once a reaction rule is matched for a species, it reacts according to the rule and new species is generated and added into the species pool. This pathway generator has been validated with the experimental data.

Daisuke et al. (Daisuke et al., 2009) has developed a Group Contribution Method (GCM) to predict reaction rate constants for aqueous phase hydroxyl radical reactions. The predicted reaction rate constants by the GCM are generally within 0.5-2 times of the experimental values (Daisuke et al., 2009). Daisuke et al. (Daisuke et al., 2011a; Daisuke

et al., 2011b; Daisuke et al., 2014) also developed linear free energy relationships (LFERs) to predict the reaction rate constants for various kinds of reaction involved in AOPs, including hydroxyl radical reaction, oxygen addition, uni- and bi- molecular peroxyl radical decay. The LFERs relate the logarithm of aqueous phase HO• reaction rate constants with free energies of activation for neutral compounds. The aqueous phase free energy of activation is calculated using *ab* initio quantum mechanical methods for the gaseous phase and a solvation method to consider the impact of water.

Lu et al. (Lu et al., 2006) has developed a directed relation graph (DRG) method to remove unimportant species and reactions from the reaction mechanism, thus the computational efficiency to solve the reaction mechanisms can be improved. To be specific, the DRG method represents the reaction mechanisms as graphs: the species are represented as dots and reactions are represented as arrows. For each reaction in the mechanism, the DRG method first calculates the direct interaction coefficient (DIC), which is defined as the ratio of the rate of this reaction to the overall consumption rate of a reactant of interest. Then, the DRG method reduces reactions by comparing the DIC values with a uniform criterion set by users and eliminating reactions that have DIC values smaller than the criterion. For example, a 0.1% of DRG criterion removes reactions that have rates smaller than 0.1% of overall consumption rate of reactant of interest from the mechanism.

Gillespie (Gillespie et al., 1971) has developed a kinetic Monte Carlo (KMC) solver that can solve reaction mechanisms without solving ODEs. Hence, the difficulty of stiffness encountered by the conventional ODEs-based empirical model can be avoided. The KMC solver has been successfully applied for various polymerization chemical

reactions, including the depolymerization of poly(veratryl β-guaiacyl ether) (McDermott et al., 1990), the hydrolytic depolymerization of cellobiose and amylose (Pinto et al., 1991), the inverse emulsion polymerization of acrylamide (Platkowski et al., 1999), and the pyrolysis of poly(styrene peroxide) (Vinu et al., 2012).

Considering all these computer tools that have been developed, it now appears to be feasible to integrate these tools into computer-based first-principles kinetic models for the degradation of organic compounds using AOPs. This study developed several computer-based first-principles kinetic model to simulate the degradation process of AOPs and investigate the fates of intermediates and byproducts. First, we developed a computer-based first-principles kinetic model with the ODE solver. This model can successfully simulate the degradation process of small parent compounds in AOPs. Second, we developed a computer-based kinetic Monte Carlo (KMC) model with the KMC solver. This KMC model can simulate the degradation process of both small and large parent compounds, since this KMC model does not require to solve ODEs and can avoid the stiffness problem. Last, we developed an on-the-fly KMC model that can further improve the computational efficiency for the simulation as compared with the KMC model.

This study will help researchers and engineers to quantitatively evaluate the performance of AOPs and have a detailed insight into the fates of intermediates and byproducts. Additionally, the pathway generator can be used to guide the design of experiments that are going to discover pathways leading to important intermediates and byproducts. For the engineering practice, this study will assist engineers to estimate the removal efficiency of certain contaminants and optimize the operational variables, such

as reaction time, chemical dosages, light intensity, etc. For teaching, our model will also benefit students by providing them with a comprehensive interdisciplinary training module that includes detailed reaction pathways, reaction rate constant predictions, and numerical analyses for solving complicated systems with the ODE and KMC solver. This activity will help engineering students who do not have sound analytical and organic chemistry backgrounds to foster concepts of environmentally-responsible water and wastewater treatment engineering.

1.2 Structure of This Dissertation

This dissertation consists of the introductory part, three main chapters, and appendices. After this introductory chapter, Chapter 2 discusses development of a computer-based first-principles kinetic model to simulate the degradation process of aqueous phase AOPs. The work from this chapter has been published in Guo et al. (Guo et al., 2014a). In Chapter 3, a computer-based kinetic Monte Carlo model has been developed. The work from this chapter has been published in Guo et al. (Guo et al., 2014b). Chapter 4 addresses the development of on-the-fly kinetic Monte Carlo model. The work from this chapter will be submitted in Guo and Crittenden (Guo et al., 2015). Appendices cover the detailed computational codes, data, procedures of calculations, and development process of simplified pseudo steady-state and pseudo steady-state model for AOPs have been presented.

CHAPTER 2

COMPUTER-BASED FIRST-PRINCIPLES KINETIC MODELING OF DEGRADATION PATHWAYS AND BYPRODUCT FATES IN AQUEOUS PHASE ADVANCED OXIDATION PROCESSES

2.1 Abstract

In this study, a computer-based first-principles kinetic model is developed to predict the degradation mechanisms and fates of intermediates and byproducts produced during aqueous phase advanced oxidation processes (AOPs) for various organic compounds. The model contains a rule-based pathway generator to generate the reaction pathways, a reaction rate constant estimator to estimate the reaction rate constant for each reaction generated, a mechanistic reduction module to reduce the generated mechanisms, an ordinary differential equations (ODEs) generator and solver to solve the generated mechanisms and calculate the concentration profiles for all species, and a toxicity estimator to estimate the toxicity of major species and calculate time-dependent profiles of relative toxicity (i.e. concentration of species divided by toxicity value). We predict concentration profiles of acetone and trichloroethylene (TCE) and their intermediates and byproducts in photolysis with hydrogen peroxide (i.e. UV/H_2O_2) and validate with experimental observations. The predicted concentration profiles for both parent compounds are consistent with experimental data. The calculated profiles of 96-hr green algae chronic toxicity show that the overall toxicity decreases during the degradation process. These generated mechanisms also provide detailed and quantitative insights into the pathways for the formation and consumption of important intermediates and

byproducts produced during AOPs. Our approach is sufficiently general to be applied to a wide range of contaminants.

2.2 Introduction

Advanced oxidation processes (AOPs) can be used for removing organic compounds in water. AOPs produce hydroxyl radicals at room temperature and pressure. These hydroxyl radicals initially react with organic compounds and further degrade these compounds in the radical-initiated chain reactions. These chain reactions are mechanistically complex. As a result, various intermediates and byproducts are produced. Some of these intermediates and byproducts (e.g., volatile acids, such as acetic or formic acids) have smaller second order reaction rate constants with hydroxyl radicals than organic parent compounds. Accordingly, these compounds require extra oxidation to be removed. In addition, some of these intermediates and byproducts may pose potential risks to human health (Rosenfeldt et al., 2004; Huber et al., 2003). Consequently, there is a need for detailed understanding of the degradation mechanisms and the fates of intermediates and byproducts produced during AOPs.

A number of studies have investigated degradation mechanisms of organic compounds during AOPs. For example, acetone and trichloroethylene (TCE) degradation using photolysis of hydrogen peroxide (i.e. UV/H_2O_2) have been examined (Stefan et al., 1996; Stefan et al., 1999; Li et al., 2007). Kinetic models for the degradation of acetone and TCE have been developed based on the experimental observations. The degradation of 1,4-dioxane and methy tert-butyl ether (MTBE) using UV/H_2O_2 process have also been examined experimentally (Stefan et al., 2000; Stefan et al., 1998; Cooper et al., 2009).

Although these studies focused on degradation mechanisms during AOPs, they are limited in the following aspects: first, experimental studies that propose degradation mechanisms are time consuming and would be cost prohibitive if one were to examine the pathways of all compounds that are used in commerce since there are a large number of emerging organic compounds being found every year (Richardson et al., 2009). Second, some studies just proposed degradation mechanisms but did not develop kinetic models to predict the degradation process (Stefan et al., 2000; Stefan et al., 1998), and other studies developed kinetic models but used lumped reactions for simplification (Stefan et al., 1996; Stefan et al., 1999; Li et al., 2007). Both of these two kinds of studies might prevent us from gaining quantitative insight into detailed degradation processes of important byproducts and intermediates produced during AOPs.

One attractive method for overcoming these limitations is to develop a computer-based first-principles kinetic model. This model automatically predicts reaction mechanisms for a given compound that is based on pre-defined reaction rules. The predicted mechanisms contain all elementary reactions occurring in the reaction process, which contrasts with the lumped models. The computer-based first-principles kinetic model also numerically solves ordinary differential equations and obtains concentration profiles of all byproducts and intermediates. Computer-based first-principles kinetic models have been successfully used for studying gas phase combustion (Van Geem et al., 2006), atmosphere chemistry (Khan et al., 2009), lubricant chemistry (Pfaendtner et al., 2008), and pyrolysis (Broadbelt et al., 1994). However, as far as the authors know, no one has developed computer-based first-principles kinetic model for AOPs.

In recent years, several computer-aided tools (Li et al., 2009; Minakata et al., 2009; Minakata et al., 2011a; Minakata et al., 2011b; Minakata et al., 2014) have been developed to investigate the degradation mechanisms of organic compounds in AOPs, and it now appears to be feasible to develop a computer-based first-principles kinetic model for the degradation of organic compounds using AOPs. In this study, we summarize our recent progresses to achieve this goal and highlight some of the remaining obstacles to be overcome. And we developed a proof-of-concept for the degradation of acetone and TCE in the UV/H2O2 AOP and validated the approach by comparing the predict results to experimental data.

2.3 Materials and Methods

2.3.1 Overall methodology

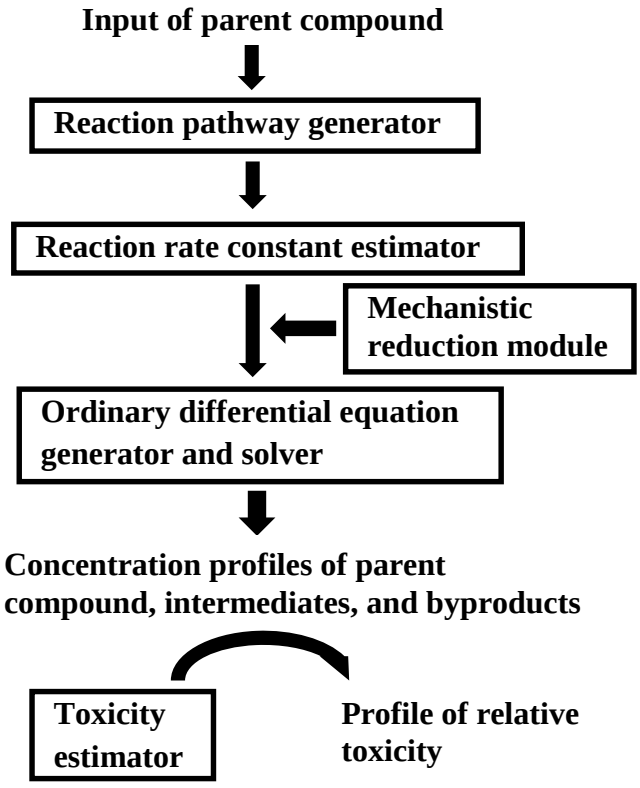

Figure 2.1. Structure and flow of a computer-based first-principles kinetic model.

Figure 2.1 displays a basic flow diagram of the overall methodology. The first component of the computer-based kinetic model is a pathway generator which was developed previously (Li et al., 2009). This pathway generator uses a computer algorithm to generate all elementary reactions that are based on pre-defined reaction rules. The second component can predict the reaction rate constant for each elementary reaction. Several robust tools, including Group Contribution Method (GCM) (Minakata et al., 2009) and Linear Free Energy Relationships (Minakata et al., 2011a; Minakata et al., 2011b), have been developed to predict the reaction rate constants for aqueous phase hydroxyl radical reactions. Prediction tools for rate constants of other reaction types in aqueous phase AOPs (e.g. oxygen addition reaction, bimolecular decay of peroxyl radical, HO_2• elimination, and β-scission reaction) have also been developed (Minakata et al., 2014). For this study, we use the GCM for hydroxyl radical reaction rate constants that do not have experimental value. For other reactions, we use literature-reported values otherwise we estimate rate constants based on the similar reactions in literature. The third component is a mechanistic reduction module, which can eliminate unimportant reactions and species and improve computational efficiency. In this study, we use the Directed Relation Graph (DRG) method (Lu et al., 2005) for the mechanistic reduction module. The DRG method first quantifies the importance of each elementary reaction by calculating the ratio of the rate of this reaction to the overall consumption rate of a reactant of interest. This ratio is named as direct interaction coefficients (DIC) that is calculated with the following equation.

$$\mathrm{DIC}_{A\to B} = \frac{r_{A\to B}}{\sum_{i\in N} r_{A\to i}} \tag{2-1}$$

where A→B is the elementary reaction for reactant A and product B, $r_{A\to B}$ is the reaction rate of reaction A→B, and N is the cluster that contains all products which can be produced from species A. Then, the DRG method reduces the mechanisms by comparing DIC value of each reaction with a uniform criterion set by users and eliminating all reactions that have DIC values smaller than this criterion. For example, a 0.1% of DRG criterion removes reactions that have rates smaller than 0.1% of overall consumption rate of reactant of interest from the mechanism. To validate the DRG method, we used the DRG method to reduce the degradation mechanism of methane generated by the pathway generator and compared the concentration profiles of major species for full and reduced mechanism. The detailed validation process can be found in the Supporting Information. The forth component is ordinary differential equations (ODEs) generator and solver. The ODEs generator can assemble the generated reactions and estimated rate constants into ODEs that describe the mass balance of all species. Then, the ODEs solver solves the generated ODEs to obtain concentration profiles of all species. The final component is a toxicity estimator that can estimate the toxicity of stable intermediates and byproducts. Several tools from the EPA P2 Framework (Office of pollution prevention and toxics, 1998), including Ecological Structure Activity Relationship (ECOSAR) (William et al., 1998), Persistent Bioaccumulative and Toxic (PBT) Profiler (Office of Pollution Prevention and Toxics, 2013), and OncoLogic (United States Environmental Protection Agency, 1990), are available for the toxicity estimation. In this study, we used ECOSAR to estimate the 96-hr green algae chronic toxicity (ChV) for parent organic compounds and intermediates and byproducts, since the 96-hr green algae ChV is the most sensitive indicator for the aquatic toxicity in ECOSAR. Based on the estimated 96-hr green algae

ChV and calculated concentration profiles, we can calculate the overall relative toxicity (RT) that evaluates the overall aquatic toxicity of the system consisted of all stable species, which including parent compound, stable intermediates and byproducts. The RT can be calculated with the following equation:

$$\mathrm{RT} = \sum_{i=1}^{n} \frac{C_i}{ChV_i} \tag{2-2}$$

where n is the number of stable species, i refers to the sets of all stable species, ChV_i is the 96-hr green algae chronic toxicity, and C_i is the concentration. We also investigated the RT with respect to the drinking water equivalent lever (DWEL) and 10^{-4} cancer risk concentration to assess the non-carcinogenic effect and carcinogenic effect, respectively.

2.3.2 Mechanism generation and selection for the degradation of acetone

The degradation mechanism of acetone in UV/H_2O_2 process was generated by the computer-based first-principles kinetic model. The experimental conditions are described by Stefan *et al* (Stefan et al., 1999). The initial concentrations of acetone and hydrogen peroxide were 1.1 mM and 15.0 mM, respectively. The initial pH was 5.9. The UV had output from 200 nm to 300 nm and the overall light intensity was 7.79×10^{-6} Einstein/L s. The reactor was completely mixed batch reactor (CMBR).

The reactions in the degradation mechanism of acetone were generated by the pathway generator. The generator enumerates all the major elementary reaction types that have been found to occur during AOPs (Li et al., 2009), including hydrogen abstraction, oxygen addition, HO_2• elimination, β scission, 1,2-H shift, and hydrolysis. The generator also includes some overall reactions, such as bimolecular decays of peroxyl radical, due to lack of experimental studies that elucidate elementary steps. The current version of

pathway generator does not include the reaction between pyruvic acid and hydrogen peroxide to produce acetic acid, because this reaction is rarely seen in aqueous phase AOPs. However, Stefan *et al.* (Stefan et al., 1999) reported that this reaction might have significant impact on the degradation of acetone specifically. Consequently, we manually added this reaction into the generated mechanisms. It should be noted that some minor reactions (e.g. photolysis of organic acids and dimerization of the carboxyl radical) are also reported from other studies (Cooper et al., 2009; Ervasti et al., 2006). However, these reactions are not included in the pathway generator due to their slow reaction rates and minor contribution to the overall reactions as compared with competing reactions.

The reaction rate constants for the generated elementary reactions were primarily obtained by two ways: (1) directly from literature (Stefan et al., 1996; Stefan, et al., 1999; Neta et al., 1990; Neta et al., 1996; Buxton et al., 1988; Von Sonntag et al., 1991) or (2) estimated by the GCM (Minakata et al., 2009). The GCM predicts hydroxyl radical reaction rate constants within 0.5-2 times of the experimental values. The rate constants for reactions except hydroxyl radicals are estimated based on similar reactions which have experimental determined rate constants. Estimating the rate constants based on similar reactions might have large errors. Table A1 in Appendix A contains all reaction rate constants and how they were obtained or estimated.

To investigate whether important reaction rate constants are accurate enough, we performed a classic local sensitivity analysis to the generated degradation mechanisms of acetone in UV/H_2O_2 process. During the local sensitivity analysis, the time-dependent sensitivity coefficient, $\left(\frac{k_j}{C_i}\frac{\partial C_i}{\partial k_j}\right)_t$, was calculated, where *Ci* is the concentration of species *i*; k_j is the reaction rate constant of reaction *j*; *t* is the time point. To measure the

impact of one specific reaction rate constant, k_j, on the overall simulation results, we calculated overall sensitivity coefficient, $\sum_t \sum_i \left(\frac{k_j}{C_i} \frac{\partial C_i}{\partial k_j} \right)_t$, by summing over $\frac{k_j}{C_i} \frac{\partial C_i}{\partial k_j}$ for all major species and various time points spanning the whole degradation process. A reaction rate constant with high overall sensitivity coefficient indicates that this reaction rate constant is important to the overall simulation results. Table A2 in Appendix A shows the sensitivity analysis results for the generated degradation mechanism of acetone in UV/H_2O_2 process. From this table, we can see that reactions that have significant impacts (i.e. overall sensitivity coefficient > 0.05) on the simulation results of the degradation of acetone are majorly consisted of two reaction categories: (1) H-abstraction reactions by hydroxyl radical, and (2) special reactions that involve the radical reactions between H_2O_2, HO·, HO_2·/O_2^-·, and CO_2^-·. The reaction rate constants of both two reaction categories can be obtained either directly from literature or estimated by the group contribution method (GCM) (Minakata et al., 2009) with small uncertainty (generally within 0.5-2 times of the experimental values). Besides these two reaction categories mentioned above, the reaction between pyruvic acid and hydrogen peroxide and the oxygen addition reaction to ·CH_2COCH_3 also have significant impact on the simulation results. The reaction rate constants of these two reactions can also be found from literature. Table A2 also shows the reaction rate constants that are estimated based on similar reactions generally have minor impacts (i.e. overall sensitivity coefficient < 0.05) on the simulation results.

Since the local sensitivity analysis requires baseline values for all reaction rate constants before the analysis and can only reflect the importance of each reaction rate constant in a small range around the baseline value, these baseline values may have

impact on the sensitivity analysis results. As a consequence, we applied multiple times of local sensitivity analysis under various baseline values of reaction rate constant of each type of reaction. These varied baseline values cover the possible range of each type of reaction rate constant as shown in Table 2.1. We found that the sensitivity analysis results are same for various baseline values of reaction rate constants within the possible ranges.

Table 2.1. Possible ranges of different types of reaction rate constants in AOPs

Reaction type	Possible range of reaction rate constant	Reference
H-abstraction reaction by hydroxyl radical	10^7 $M^{-1}s^{-1}$ to 10^9 $M^{-1}s^{-1}$	Buxton et al., 1988
H-abstraction reaction by carbon-centered radical	10 $M^{-1}s^{-1}$ to 10^3 $M^{-1}s^{-1}$	Neta et al., 1996
Oxygen addition to carbon-centered radical	10^8 $M^{-1}s^{-1}$ to 10^{10} $M^{-1}s^{-1}$	Neta et al., 1996
Bimolecular decay of peroxyl radical	10^8 $M^{-1}s^{-1}$ to 10^9 $M^{-1}s^{-1}$ for primary and secondary preroxyl radical; 10^4 $M^{-1}s^{-1}$ to 10^5 $M^{-1}s^{-1}$ for tertiary preroxyl radical	Neta et al., 1990
HO_2• elimination reaction	10 s^{-1} to 10^5 s^{-1}	Neta et al., 1990
β scission reaction	10^4 s^{-1} to 10^7 s^{-1}	Li et al., 2009
1,2-H shift reaction	10^4 s^{-1} to 10^7 s^{-1}	Li et al., 2009

The mechanisms were simplified using the DRG method. For the purpose of generating mechanisms with appropriate size and quality, we tried various criteria (ε) for the DRG method and investigated the impact of ε on the sizes and quality of the generated mechanisms. Table 2.2 shows the growth of the numbers of species and reactions versus the DRG criterion ε. Not surprisingly, the number of species and

reactions increase as ε decreases since smaller ε increases the number of species that need to be included. We used the overall sample deviation (SD) to measures the relative error between experimental data and calculated data. The overall SD is calculated as below

$$\text{overall SD} = \sqrt{\frac{1}{N-1}\sum_{i=1}^{N}\left[(C_{exp,i} - C_{cal,i}) / C_{exp,i}\right]^2} \qquad (2\text{-}3)$$

where N is the number of total data points; $C_{exp,i}$ and $C_{cal,i}$ are the experimental and calculated concentrations of species (i.e. hydrogen peroxide, acetone, formic acid, acetic acid, oxalic acid, pyruvic acid, and pyruvic aldehyde), respectively; and the index i refers to the set of all major species and times for which experimental data are available. As shown in Table 2.2, the overall SD decreases from 0.79 to 0.68 as the number of species and reactions increase. This decrease of overall SD means the addition of species and reactions into the generated mechanisms can diminish the relative error between experimental data and simulation results. As we want to select a mechanism with a relative small size and a high quality, we chose the mechanism corresponding to $\varepsilon = 10^{-3}$ (59 species and 103 reactions) for further analysis.

Table 2.2. Changes in size and overall SD of the generated acetone and TCE degradation mechanisms as a function of ε

ε	Number of species	Number of reactions	Overall SD
Acetone degradation			
10^{-1}	47	92	0.79
10^{-2}	48	94	0.79
10^{-3}	59	103	0.68
10^{-4}	59	107	0.68
5×10^{-5}	59	107	0.68
4×10^{-5}	119	185	0.68
3×10^{-5}	119	185	0.68
2×10^{-5}	119	192	0.68
TCE degradation			
10^{-1}	16	15	N.A.
10^{-2}	41	89	0.62
10^{-3}	41	89	0.62
10^{-4}	68	127	0.62
10^{-5}	111	202	0.62
10^{-10}	113	262	0.62
10^{-11}	120	368	0.62
10^{-12}	120	370	0.62

The ODEs for the kinetic model were generated by the ODE generator and solved with a stiff ODE solver, named backward differentiation formula method (i.e. Gear's method [Hindmarsh et al., 1974]) to obtain the concentration profiles of all species.

2.3.3 Mechanism generation and selection for the degradation of TCE

We next generated the degradation mechanism of TCE in UV/H_2O_2 process. The experimental conditions are described by Li *et al*. (Li et al., 2007) The initial concentrations of TCE and hydrogen peroxide were 1.08 mM and 10.4 mM, respectively. The initial pH was 5.9. The UV had output from 200 nm to 300 nm and the overall light intensity was 7.79×10^{-6} Einstein/L s. The reactor was completely CMBR.

The elementary reactions in TCE degradation mechanism were generated with the pathway generator and the reaction rate constant for each elementary reaction was obtained with the same way that was used in the case of acetone as described above. It is noted that current version of the pathway generator does not predict photolysis reactions of TCE, and this may significantly impact the degradation process. Consequently, we manually added the photolysis reactions to the mechanism.

To investigate whether important reaction rate constants are accurate enough, we performed a classic local sensitivity analysis to the generated degradation mechanisms of TCE with the same way that was used in the case of acetone. Table A3 in Appendix A shows the sensitivity analysis results for the generated degradation mechanism of TCE in UV/H_2O_2 process. From this table, we can see that reactions that have significant impacts (i.e. overall sensitivity coefficient > 0.05) on the simulation results of the degradation of TCE are majorly consisted of four reaction categories: (1) H-abstraction reactions by hydroxyl radical, (2) special reactions that involves the radical reactions between H_2O_2, HO•, HO_2•/O_2^-•, and CO_2^-•, (3) addition reaction of hydroxyl radical to unsaturated bond, and (4) β-scission reaction of oxyl radical. The reaction rate constants of all these four reaction categories can be obtained either directly from literature or estimated by the group contribution method (GCM) with small uncertainty (generally within 0.5-2 times of the experimental values). Table A3 also shows the reaction rate constants that are estimated based on similar reactions generally have minor impacts (i.e. overall sensitivity coefficient < 0.05) on the simulation results.

The mechanism was reduced using the DRG method. As was the case of acetone, we also tried various criteria of DRG method (ε) to investigate the impact of ε on the size

and quality of the generated degradation mechanism for TCE. Table 2.2 shows that the number of species and reactions in the generated mechanisms increase as ε decrease. Table 2.2 also shows the impact of the criteria of DRG method (ε) on the quality of the predicted concentration profiles, which was evaluated by the overall SD value calculated by equation (2-3). When $\varepsilon = 10^{-1}$ (or higher), the overall SD is not available because some experimental observed species [i.e. dichloroacetic acid (DCA) and monochloroacetic acid (MCA)] are eliminated from the generated mechanism under a high ε. When $\varepsilon \leq 10^{-2}$, the overall SD remains at 0.62, which means that the increase of the size of the mechanism does not significantly affect the relative error between experimental data and simulation results. On the basis of all data presented in Table 2.2, the generated mechanism corresponding to $\varepsilon = 10^{-2}$ (41 species and 89 reactions) was chosen to be further analyzed, because this mechanism has small size and contains all significant reactions and species. The ODEs for the kinetic model were solved with the Gear's method.

2.4 Results and Discussion

In this section, the degradation mechanisms of acetone and TCE are validated with experimental data and quantitatively analyzed to elucidate the detailed pathways for the formation and consumption of important intermediates and byproducts.

2.4.1 Computational results and analysis for the degradation of acetone

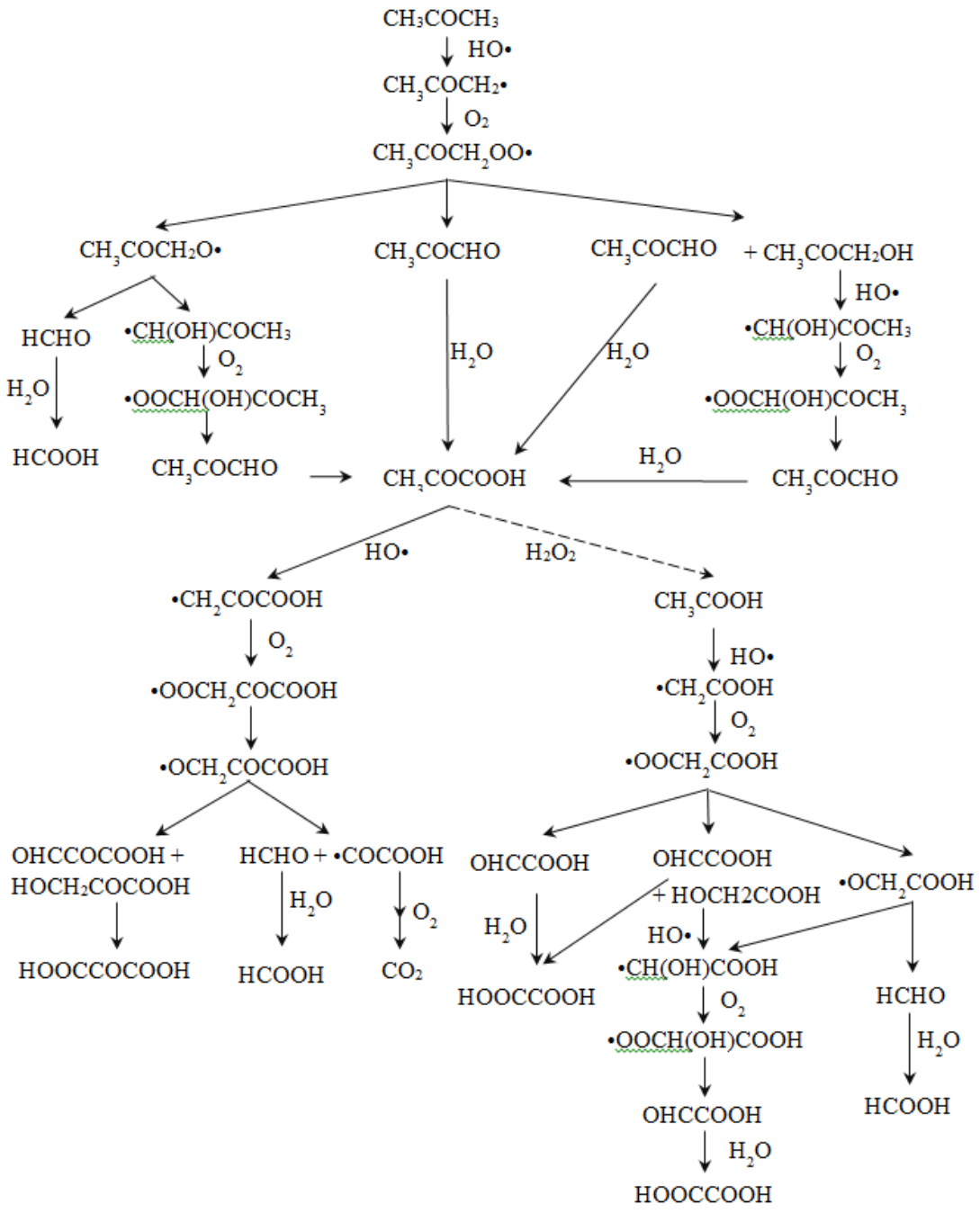

Figure 2.2. Generated degradation mechanism of acetone in UV/H_2O_2 process corresponding to $\varepsilon = 10^{-3}$. Dashed lines represent manually added reactions. Solid lines represent generated reactions by the pathway generator.

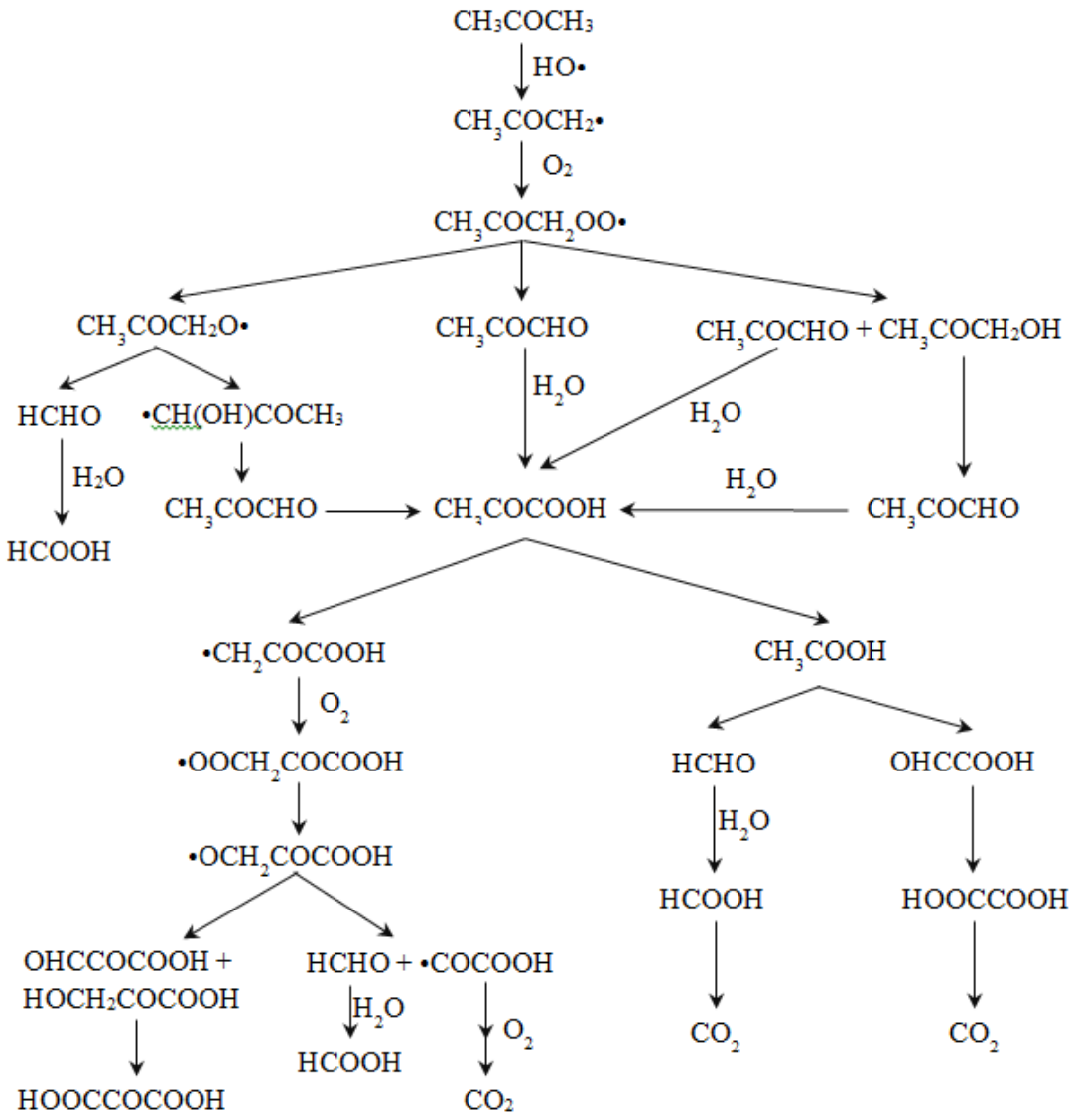

Figure 2.3. The experimentally determined degradation pathways of acetone in UV/H_2O_2 process adapted from Stefan *et al* (Stefan et al., 1999).

Figure 2.2 shows generated degradation mechanism of acetone. This mechanism covers most reactions and species experimentally determined by Stefan *et al*.[4] as shown in Figure 2.3.

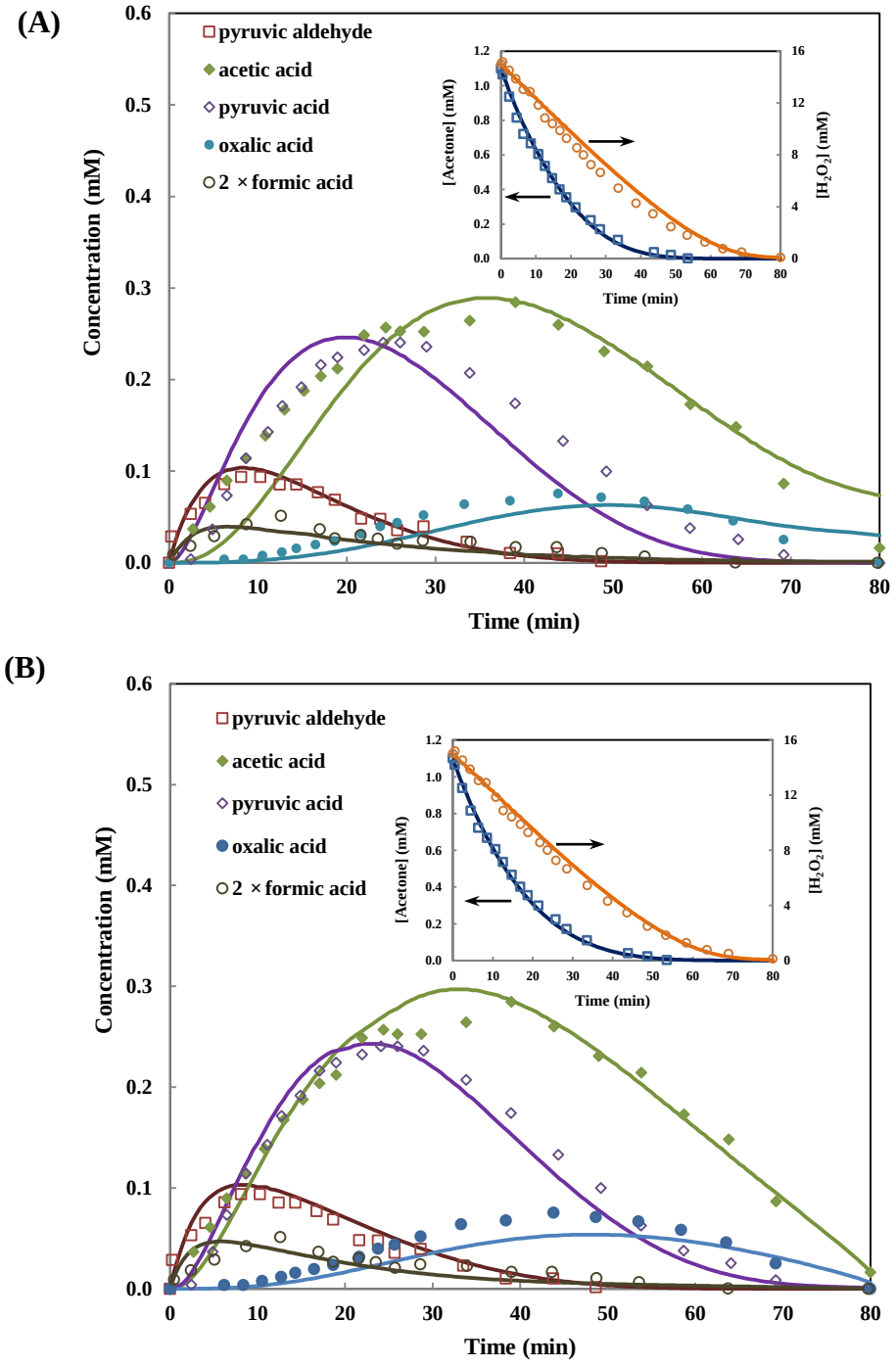

Figure 2.4. Comparison of concentration profiles of major species between experimental data (Stefan et al., 1999) and predicted data for the degradation of acetone during UV/H_2O_2 process. (A) Without optimization, and (B) with optimization.

Table 2.3 SD values of major species for the degradation of acetone and TCE in UV/H_2O_2 process

Parent compound	Major species	SD values for model without data fitting	SD values for model with data fitting
Acetone	Acetone	0.21	0.10
	Hydrogen peroxide	0.15	0.13
	Pyruvic aldehyde	0.23	0.23
	Pyruvic acid	0.49	0.22
	Acetic acid	0.39	0.21
	Oxalic acid	0.47	0.24
	Formic acid	0.40	0.25
TCE	TCE	0.17	0.07
	Hydrogen peroxide	0.15	0.15
	Formic acid	0.26	0.12
	Oxalic acid	0.35	0.17
	DCA	0.47	0.25
	MCA	0.36	0.19

Figure 2.4 (A) shows the predicted concentration profiles of major species (i.e. hydrogen peroxide, acetone, formic acid, oxalic acid, acetic acid, pyruvic aldehyde, and pyruvic acid) predicted by the acetone degradation mechanism corresponding to the DRG criterion (ε) of 10^{-3} and the experimental data that was reported by Stefan *et al* (Stefan et al., 1999). Given that the model simulation is a first-principle prediction, the calculated concentration profiles are in reasonably good agreement with the experimental data. To quantitatively evaluate the discrepancy between predicted concentration profile and experimental concentration profile for each major species, Table 2.3 calculates the SD value of each major species by equation 2-4.

$$\mathrm{SD}_j = \sqrt{\frac{1}{N_j - 1}\sum_{i=1}^{N_j}\left[(C_{exp,i} - C_{cal,i}) / C_{exp,i}\right]^2} \qquad (2\text{-}4)$$

where index j refers to certain major species j, N_j is the number of data points of major species j; $C_{exp,i}$ and $C_{cal,i}$ are the experimental and calculated concentrations of major species j, respectively; and the index i refers to the set of all times for which experimental data are available. From Table 2.3, we can see that the pyruvic acid has the largest SD (i.e. largest discrepancy between experimental and calculated data), followed by oxalic acid, acetic acid, and formic acid. The reason for these large SD values might be that the reaction rate constants for various elementary reaction channels between pyruvic acid and hydroxyl radical (i.e. reaction 2-5 to 2-8) were not estimated correctly by the GCM. The uncertainties in the rate constants not only impact the concentration profile of pyruvic acid, but also impact the concentration profiles of oxalic acid, acetic acid and formic acid since these species are byproducts of pyruvic acid. The sensitivity analysis results also confirm that the model is highly sensitive to the reaction rate constants between pyruvic acid and hydroxyl radical as shown in Table A-1 in Appendix A. It should be noted that Schaefer *et al* (Schaefer et al., 2012). has reported an experimental value for the overall reaction rate constant between hydroxyl radical and pyruvic acid. However, this value cannot be used in our elementary reaction pathway.

$$CH_3COCOOH + HO\bullet \longrightarrow \bullet CH_2COCOOH + H_2O \quad (2\text{-}5)$$

$$CH_3COCOO^- + HO\bullet \longrightarrow \bullet CH_2COCOO^- + H_2O \quad (2\text{-}6)$$

$$CH_3COCOOH + HO\bullet \xrightarrow{H_2O} \bullet OC(OH)(CH_3)COOH + H_2O \quad (2\text{-}7)$$

$$CH_3COCOO^- + HO\bullet \xrightarrow{H_2O} \bullet OC(OH)(CH_3)COO^- + H_2O \quad (2\text{-}8)$$

To improve the simulation results, we optimized reaction rate constants of reaction 2-5 to 2-8 using the Genetic Algorithm with the following objective function

$$\mathrm{SD} = \sqrt{\frac{1}{N-1}\sum_{i=1}^{N}\left[(C_{exp,i} - C_{cal,i}) / C_{exp,i}\right]^2} \qquad (2\text{-}9)$$

where N is the number of total data points; $C_{exp,i}$ and $C_{cal,i}$ are the experimental and calculated concentrations of major species (i.e. experimentally observable species, including hydrogen peroxide, acetone, formic acid, acetic acid, oxalic acid, pyruvic acid, and pyruvic aldehyde), respectively; and the index i refers to the set of all major species and times for which experimental data are available. The optimized rate constants for reaction 2-5 to 2-8 are listed in Table 2.4. Figure 2.4(B) shows that the improved simulation results as compared with experimental data (Stefan et al., 1999). From Figure 2.4(B), we can see that the accuracy of simulation results is improved by optimizing reaction rate constants of reaction 2-5 to 2-8. Table 2.3 also confirms this improvement of accuracy by showing that the SD values for the improved simulation results of pyruvic acid, acetic acid, oxalic acid, and formic acid decrease by almost a factor of two as compared with simulation results without optimization.

Table 2.4. Estimated and optimized reaction rate constants for the degradation of acetone and TCE

Reaction	Estimated rate constant ($M^{-1}s^{-1}$)	Optimized rate constant ($M^{-1}s^{-1}$)
Acetone degradation		
$CH_3COCOOH + \bullet OH \rightarrow \bullet CH_2COCOOH + H_2O$	5.43×10^7	7.2×10^7
$CH_3COCOO^- + \bullet OH \rightarrow \bullet CH_2COCOO^- + H_2O$	5.43×10^7	1.1×10^8
$CH_3COCOOH + \bullet OH \rightarrow CH_3O^{\bullet}C(OH)COOH$	10^5	4×10^3
$CH_3COCOO^- + \bullet OH \rightarrow CH_3O^{\bullet}C(OH)COO^-$	10^5	6×10^3
TCE degradation		
$ClHC{=}C(Cl)O^{\bullet} + H_2O \rightarrow ClCH_2COOH + Cl^{\bullet}$	$0.005s^{-1}$	$0.0056s^{-1}$
$OHC\text{-}CHCl_2 + H_2O \xrightarrow{HO\bullet} Cl_2CHCOOH$	7.81×10^8	4.69×10^8
$OHC\text{-}C(O)Cl + H_2O \rightarrow OHCCOOH + HCl$	$0.005s^{-1}$	$0.004s^{-1}$
$OHCCOOH + H_2O \xrightarrow{HO\bullet} HOOCCOOH$	2.86×10^7	3.28×10^7
$Cl_2CH\text{-}C(O)Cl + H_2O \rightarrow Cl_2CHCOOH + HCl$	$0.005s^{-1}$	$0.0068s^{-1}$

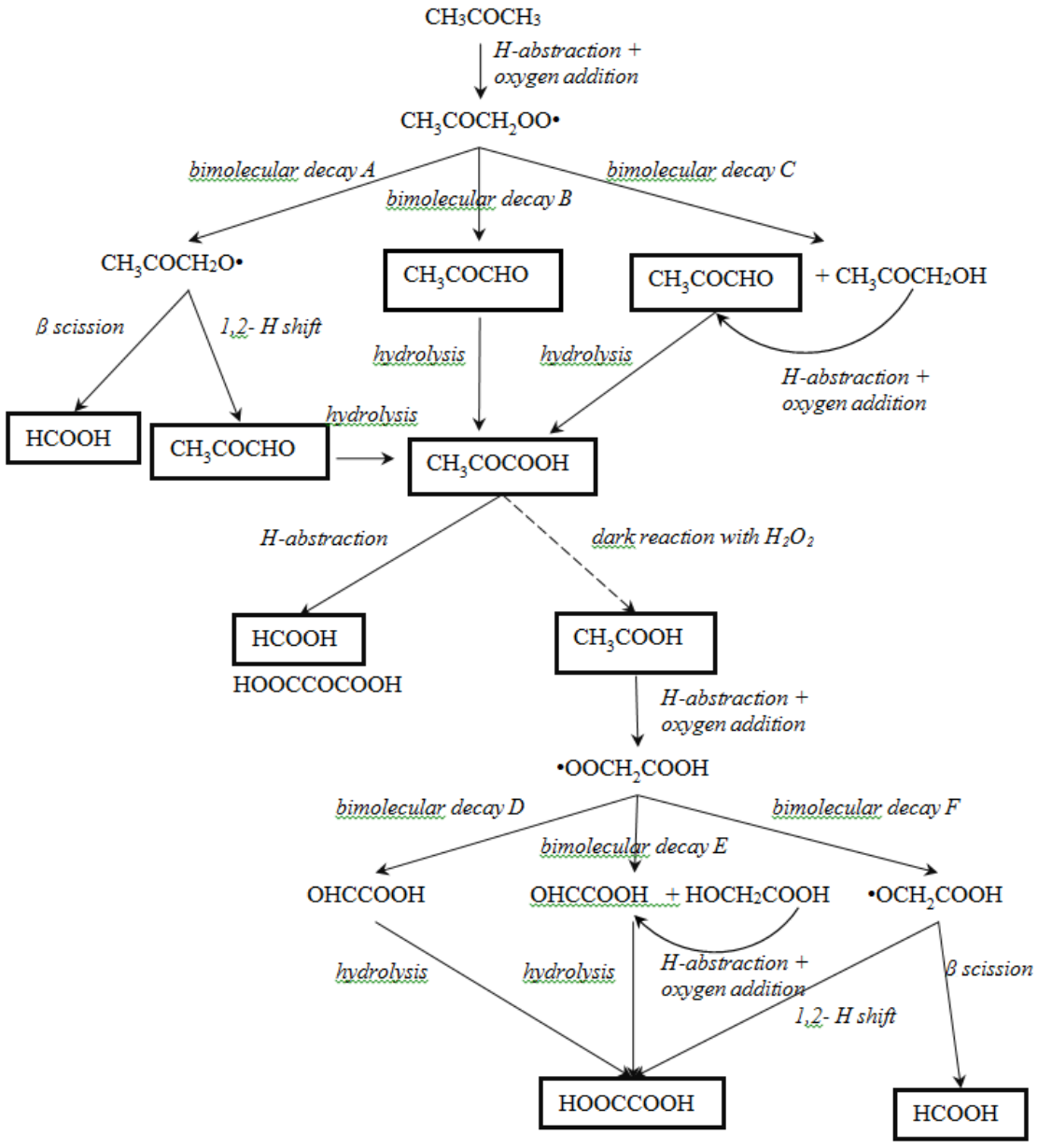

Figure 2.5. Dominant transformation pathways among major intermediates for the degradation of acetone during UV/H_2O_2 process. Solid lines represent generated reactions by the pathway generator. Marked species are key intermediates and byproducts of interest.

According to the study of Stefan *et al.* (Stefan et al., 1999), five species, including pyruvic aldehyde, pyruvic acid, acetic acid, oxalic acid, and formic acid, were identified and quantified as major intermediates that significantly contribute to overall acetone degradation. With the computer-based first-principle kinetic model, we are able to quantitatively elucidate the dominant transformation pathways among these major intermediates as shown in Figure 2.5. First, pyruvic aldehyde is generated from acetone by three pathways corresponding to the branching bimolecular decay channels (i.e. bimolecular decay A, B, and C in Figure 2.5) of peroxyl radical, $CH_3COCH_2OO\bullet$, which is generated by the H-abstraction of acetone followed by oxygen addition. Among these three bimolecular decay channels, bimolecular decay C, which is known as Russell reaction (Russell, 1957), is dominant for the formation of pyruvic aldehyde with a contribution of 56%. The contributions of bimolecular decay A followed by 1,2-H shift reaction and bimolecular decay B are 30% and 14%, respectively, which is consistent with the results of Schaefer *et al.*[29] It should be noted that according to von Sonnatag *et al.* (von Sonnatag et al., 1991), $CH_3COCH_2OO\bullet$ also has the possibility to produce peroxide $CH_3COCH_2OOCH_2COCH_3$ via reaction 2-10. However, this reaction is at least 10^3 times slower than competing reactions (i.e. bimolecular decay A, B, and C in Figure 2.5). Thus, this reaction is eliminated by the DRG reduction.

$$2CH_3COCH_2OO\bullet \longrightarrow CH_3COCH_2OOCH_2COCH_3 + O_2 \qquad (2\text{-}10)$$

Pyruvic aldehyde is degraded by the hydrolysis reaction to produce pyruvic acid. Second, pyruvic acid is only produced from pyruvic aldehyde as mentioned above. Pyruvic acid is degraded by two pathways: (1) H-abstraction reaction, which leads to the production of the formic acid, and (2) dark reaction with hydrogen peroxide, which produces the acetic

acid. The contributions of these two pathways for the consumption of pyruvic acid are almost identical. Although Stefan *et al* (Stefan et al., 1999). proposed that pyruvic acid is also degraded by H-abstraction from hydrated pyruvic acid/pyruvate (i.e. reaction 2-7 and 2-8), we find these reactions are at least 10^4 times slower than competing reactions. Thus, these reactions are removed by the DRG reduction. Third, acetic acid is only produced from pyruvic acid as mentioned above. Although Stefan *et al* (Stefan et al., 1999). proposed other potential pathways for the formation of acetic acid (e.g. reaction 2-11 and 2-12), we find that these pathways are at least 10^3 times slower than competing reactions and these reactions are removed by the DRG reduction.

$$CH_3C(O)OO\bullet + CH_3COCH_2OO\bullet \longrightarrow CH_3COOH + CH_3COCHO + O_2 \quad (2\text{-}11)$$

$$\bullet CH_2COCOOH \longrightarrow CH_2=C=O \xrightarrow{H_2O} CH_3COOH \quad (2\text{-}12)$$

Acetic acid is degraded to produces oxalic acid by three pathways corresponding to the branching bimolecular decay channels (i.e. bimolecular decay D, E, and F in Figure 2.5) of peroxyl radical, $\bullet OOCH_2COOH$, which is generated by the H-abstraction of acetic acid followed by oxygen addition. The ratio of the contributions of these three formation pathways is 2:2:1. Similar to $CH_3COCH_2OO\bullet$, $\bullet OOCH_2COOH$ also has the possibility to produce peroxide $HOOCCH_2OOCH_2COOH$. However, this reaction pathway is at least 10^3 times slower than competing reactions (i.e. bimolecular decay D, E, and F in Figure 2.5) and is eliminated by the DRG reduction. Forth, oxalic acid is only produced from acetic acid as mentioned above and only degraded to carbon dioxide and water. Fifth, formic acid is produced by three pathways: (1) from $CH_3COCH_2OO\bullet$ by bimolecular decay A followed by β scission; (2) from $\bullet OOCH_2COOH$ by bimolecular decay F followed by β scission; and (3) from pyruvic acid by H- abstraction initiated reactions.

The first pathway dominates at early degradation stage (0-30 min) and the second pathway dominates at late degradation stage (30-80 min). The third pathway is over one order slower than the other two pathways. Formic acid is only degraded to carbon dioxide and water.

2.4.2 Computational results and analysis for the degradation of TCE

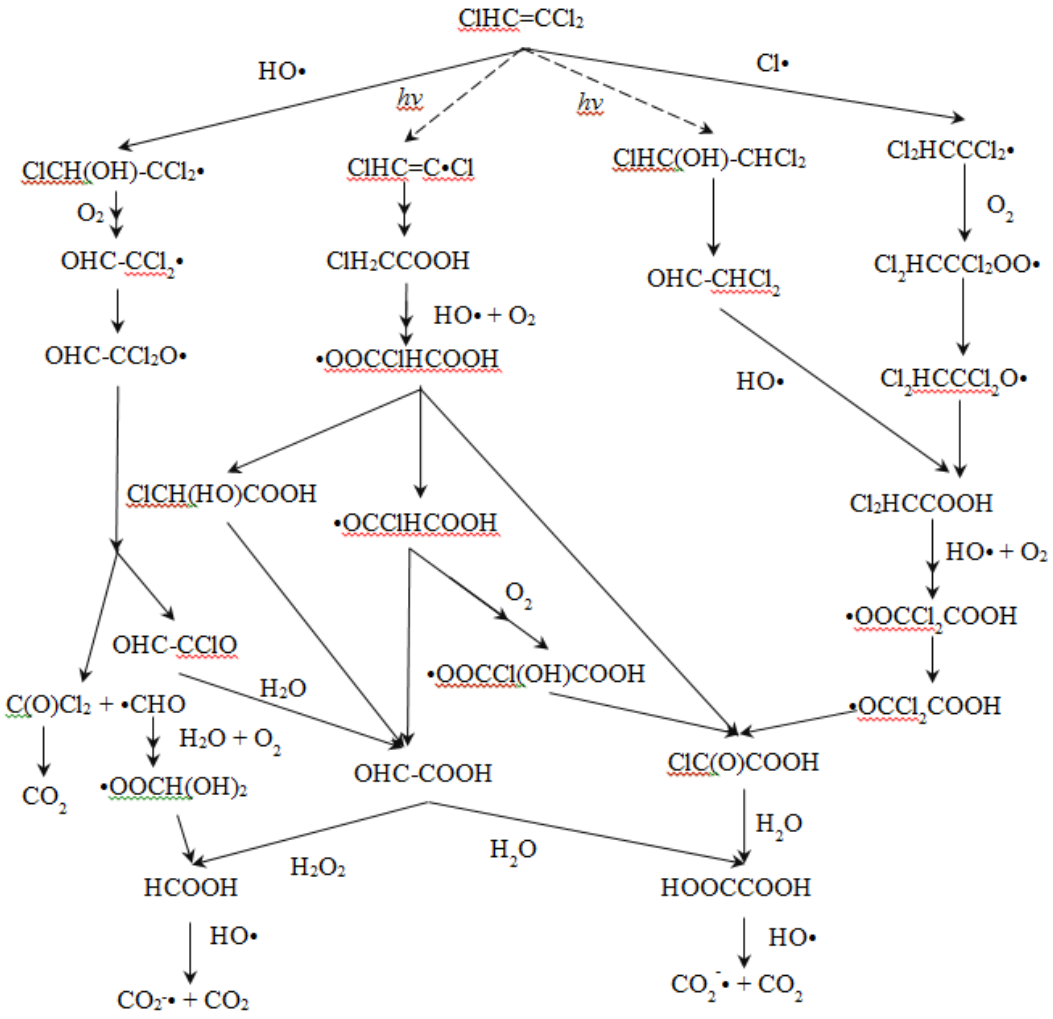

Figure 2.6. Generated degradation mechanism of TCE in UV/H_2O_2 process corresponding to $\varepsilon = 10^{-2}$. Dashed lines represent manually added reactions. Solid lines represent generated reactions by the pathway generator.

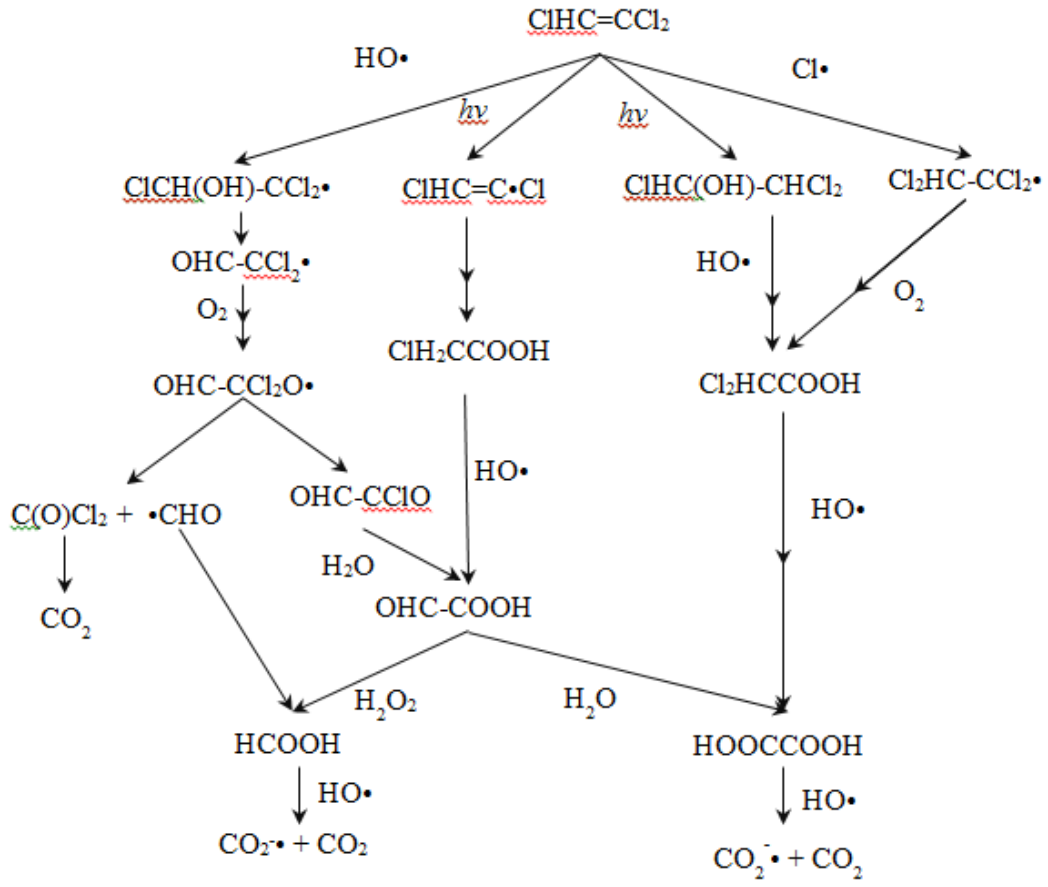

Figure 2.7. The experimentally determined degradation pathways of TCE in UV/H_2O_2 process adapted from Li *et al* (Li et al., 2007).

Figure 2.6 shows generated degradation mechanism of TCE, which covers most reactions and species experimentally determined by Li *et al* (Li et al., 2007) as shown in Figure 2.7.

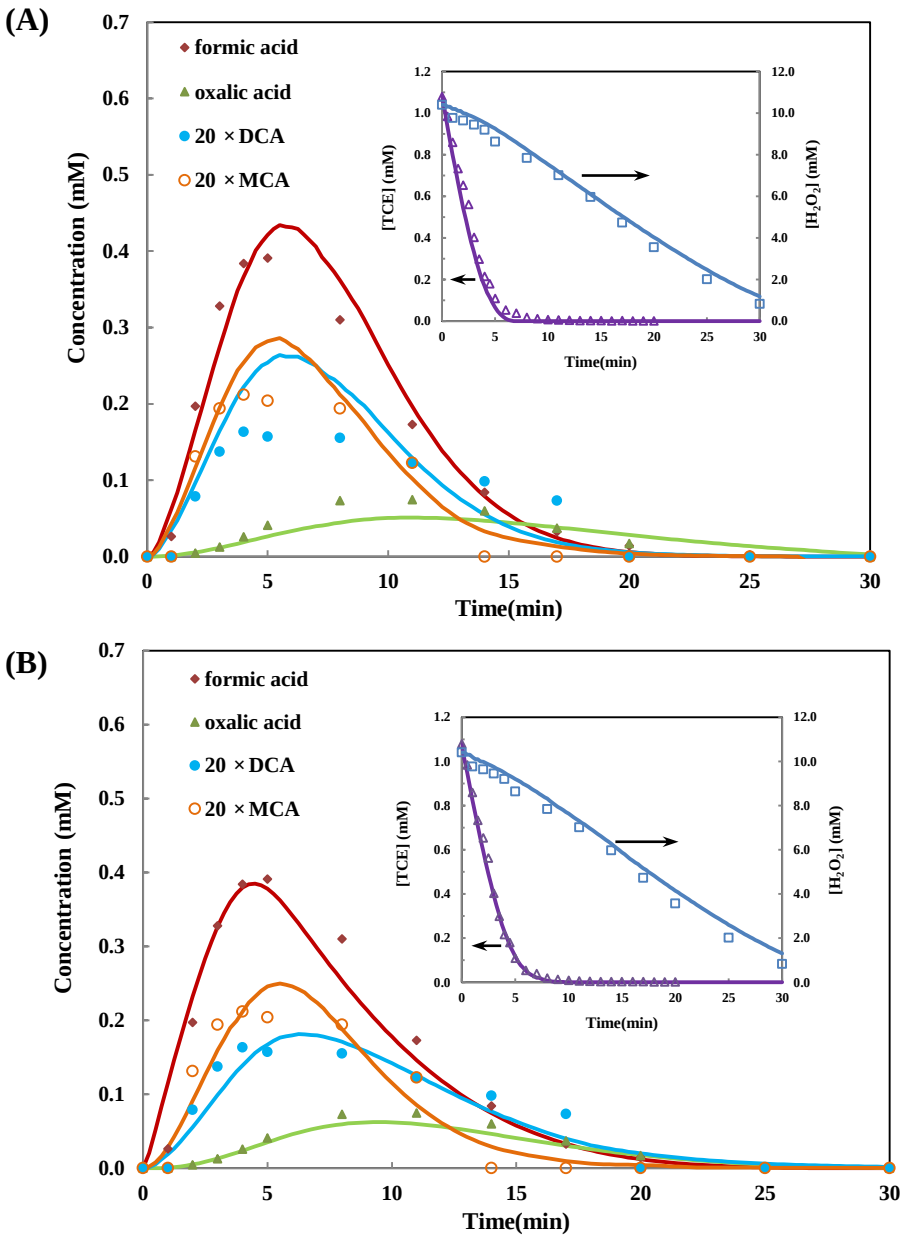

Figure 2.8. Comparison of concentration profiles of major species between experimental data[5] and predicted data for the degradation of TCE during UV/H_2O_2 process. (A) Without optimization, and (B) with optimization.

Figure 2.8 (A) shows that the calculated concentration profiles of major species (i.e. hydrogen peroxide, TCE, oxalic acid, DCA, MCA, and formic acid) are in good agreement with the experimental data without any parameter fitting. The SD value for each major species is also calculated in Table 2.3, where we can see that the DCA has the

largest SD, followed by MCA, and oxalic acid. The reason for these large SD values might be that the reaction rate constants for the formation of DCA (i.e. reaction 2-13 and 2-14), MCA (i.e. reaction 2-15), and oxalic acid (i.e. reaction 2-16 and 2-17) were either incorrectly estimated by GCM or estimated based on similar reactions. Both of these two estimations might bring uncertainty that can impact the concentration profiles of DCA, MCA, and oxalic acid. The sensitivity analysis result also confirms that the model is highly sensitive to these reaction rate constants as shown in Table A.2 in Appendix A.

$$OHC\text{-}CHCl_2 + H_2O \xrightarrow{HO^\bullet} Cl_2CHCOOH \quad (2\text{-}13)$$

$$Cl_2CH\text{-}C(O)Cl + H_2O \rightarrow Cl_2CHCOOH + HCl \quad (2\text{-}14)$$

$$ClHC{=}C(Cl)O^\bullet + H_2O \rightarrow ClCH_2COOH + Cl^\bullet \quad (2\text{-}15)$$

$$OHC\text{-}C(O)Cl + H_2O \rightarrow OHCCOOH + HCl \quad (2\text{-}16)$$

$$OHCCOOH + H_2O \xrightarrow{HO^\bullet} HOOCCOOH \quad (2\text{-}17)$$

To improve the simulation results, we optimized reaction rate constants for reaction 2-13 to 2-17. The details of the optimization process is the same with the case of acetone. The optimized rate constants for reaction 2-13 to 2-17 are listed in Table 2.4. Figure 2.8(B) shows that the improved simulation results agree better with experimental data (Li et al., 2007) as compared with simulation results without optimization. Table 2.3 also confirms this improvement of accuracy by showing that the SD values for the improved simulation results of DCA, MCA, and oxalic acid decrease by almost a factor of two as compared with simulation results without optimization.

TCE can be degraded by three ways, including hydroxyl radical addition, photolysis reactions, and chloride radical addition. Based on net rate analysis results, we

find that TCE is majorly degraded by hydroxyl radical addition with a contribution of 90%. The photolysis reactions degrade TCE with a contribution more than 9% and the chloride radical addition has a contribution less than 1%.

The photolysis reaction rate is calculated by the following equations

$$r_{UV,i} = -\Phi_i \sum_{\lambda=200}^{300} \left[\mathrm{I}_\lambda f_{i,\lambda} \left(1 - e^{-A_\lambda}\right) \right]$$

$$A_\lambda = 2.303b \left(\varepsilon_{TCE,\lambda} C_{TCE} + \varepsilon_{H_2O_2,\lambda} C_{H_2O_2} + \varepsilon_{HO_2^-,\lambda} C_{HO_2^-} + \sum_{all\ organic\ acid} \varepsilon_{acid,\lambda} C_{acid} \right) \quad (2\text{-}18)$$

$$f_{i,\lambda} = 2.303b\varepsilon_{i,\lambda} C_i \,/\, A_\lambda$$

where Φ_i is the quantum yield of compound *i*, mole/einstein; I_λ is the volume-averaged UV intensity at wavelength λ, einstein/L·s; $f_{i,\lambda}$ is the fraction of light absorbed by each species, dimensionless; A_λ is the solution absorbance at wavelength λ, dimensionless; b is the mean path length of the UV light in the solution, cm; ε_λ is the molar absorption coefficient for each species, $M^{-1}cm^{-1}$; C_i is the concentration of each species, M. It should be noted that we did not consider the UV photolysis of organic acid since they are insignificant. However, the UV absorption of these organic acids was included due to their large extinction coefficients.

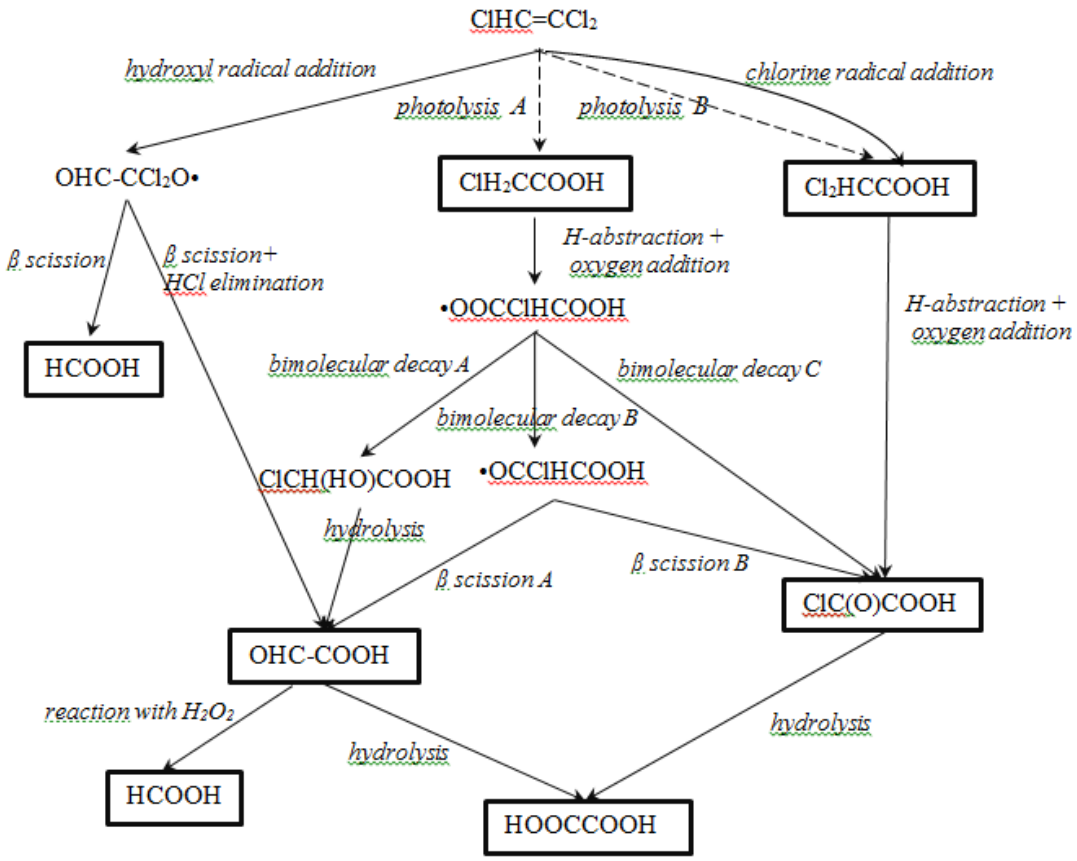

Figure 2.9. Dominant transformation pathways among major intermediates for the degradation of TCE during UV/H_2O_2 process. Solid lines represent generated reactions by the pathway generator. Marked species are key intermediates and byproducts of interest.

According to Li *et al.* (Li et al., 2007), six species, including DCA, MCA, chloroglyoxalic acid, glyoxalic acid, oxalic acid, and formic acid, were identified as major intermediates that significantly contribute to overall TCE degradation. We quantitatively analyzed the dominant formation and consumption pathways for all of these major intermediates as shown in Figure 2.9. First, the generation of DCA from TCE is dominated by the photolysis of TCE (i.e. photolysis B in Figure 2.9), which produces 10 times more DCA than the comparable generation pathway initiated by the chlorine radical addition of TCE. DCA is degraded to chloroglyoxalic acid via H-abstraction

followed by oxygen addition. Second, MCA can only be generated from TCE by the photolysis of TCE (i.e. photolysis A in Figure 2.9), which is consistent with the experimental observation (Li et al., 2007). MCA is degraded by three pathways corresponding to the branching bimolecular decay channels (i.e. bimolecular decay A, B, and C in Figure 2.9) of the peroxyl radical, •OOCClHCOOH, which is generated by the H-abstraction of MCA followed by oxygen addition. The contributions of these three bimolecular decay channels are the same. These bimolecular decay channels produce chloroglyoxalic acid and glyoxalic acid in the subsequent reactions. Third, chloroglyoxalic acid is generated by three ways: (1) from •OOCClHCOOH through bimolecular decay B followed by β scission B; (2) from •OOCClHCOOH through bimolecular decay C; and (3) from DCA through H-abstraction followed by oxygen addition. The ratio of the contributions of these three formation pathways of chloroglyoxalic acid is 2:2:1. Chloroglyoxalic acid undergoes hydrolysis to produce oxalic acid. Forth, glyoxalic acid is mostly produced both from MCA via bimolecular decay A followed by hydrolysis and from TCE via hydroxyl radical addition followed by β scission + HCl elimination. The contributions of these two formation pathways for the glyoxalic acid are identical. In addition, glyoxalic acid can also be produced from MCA through bimolecular decay B followed by β scission A. This pathway is at least 10^4 times slower than the other two formation pathways mentioned above. The major degradation pathway for glyoxalic acid is the hydrolysis to produce oxalic acid, which is 10 times faster than the degradation pathway with hydrogen peroxide to produce formic acid. Fifth, oxalic acid is formed from two pathways: the hydrolysis of glyloxalic acid and the hydrolysis of chloroglyoxaclic acid. The contributions of these two reactions are identical.

Oxalic acid is degraded by hydroxyl radical attack and is mineralized to carbon dioxide and water. Finally, the formation of formic acid is dominated by the hydroxyl radical addition to TCE followed by β scission, which is over 100 times faster than the competing formation pathway involving the reaction between glyoxalic acid and hydrogen peroxide. Formic acid is degraded by reaction with hydroxyl radical to produce carbon dioxide and water.

2.4.3 Toxicity estimation for the degradation of acetone and TCE in UV/H_2O_2 process

In this section, we investigated the overall relative toxicity with respect to 96-hr green algae chronic toxicity, drinking water equivalent lever, and 10^{-4} cancer risk concentration to assess the aquatic toxicity, non-carcinogenic effect, and carcinogenic effect, respectively.

2.4.3.1 96-hr green algae chronic toxicity

The detailed description and calculated overall relative toxicity of 96-hr green algae chronic toxicity (ChV) can be found in the manuscript. Table 2.5 and Table 2.6 show the predicted ChV of major species for the degradation of acetone and TCE in UV/H_2O_2 process. Figure 2.10 and Figure 2.11 show the calculated overall relative toxicity profile with respect to 96-hr green algae ChV for the degradation of acetone and TCE, respectively.

Table 2.5 96-hr green algae ChV of major species predicted by ECOSAR for the degradation of acetone in UV/H_2O_2 process.

Speices	96-hr Green Algae ChV (mg/L)
Acetone	76
Pyruvic aldehyde	592.5
Pyruvic acid	495.4
Acetic acid	484.7
Oxalic acid	1050
Formic acid	83

Table 2.6 96-hr green algae ChV of major species predicted by ECOSAR for the degradation of TCE in UV/H_2O_2 process

Speices	96-hr Green Algae ChV (mg/L)
Trichloroethylene (TCE)	2.9
Formic acid	83
Oxalic acid	1050
Monochloroacetic acid (MCA)	529
Dichloroacetic acid (DCA)	556

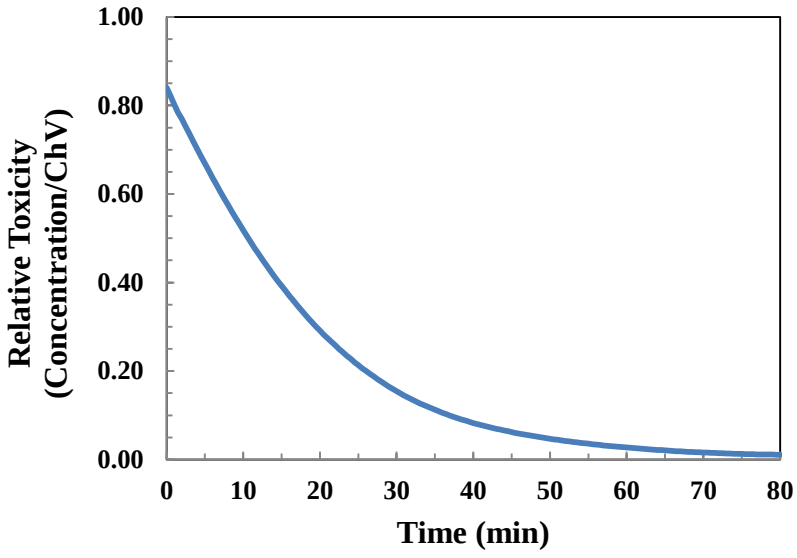

Figure 2.10. Calculated profile of overall relative toxicity with respect to 96-hr green algae ChV for the degradation of acetone in UV/H_2O_2 process.

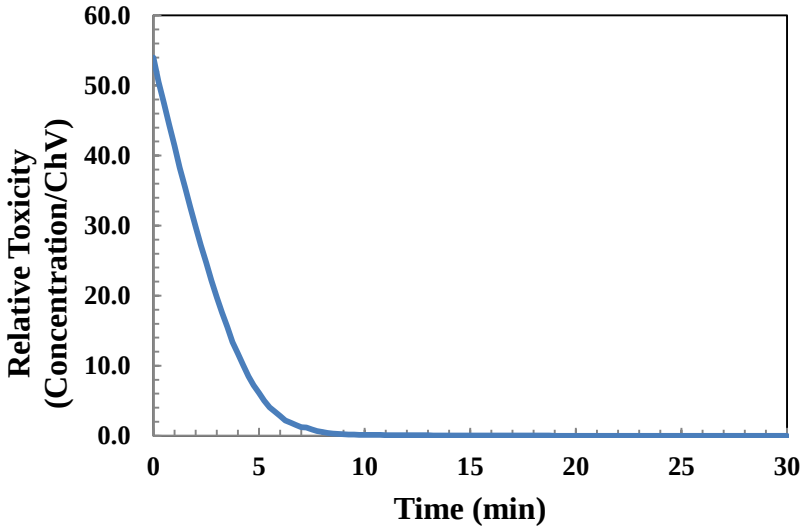

Figure 2.11. Calculated profile of overall relative toxicity with respect to 96-hr green algae ChV for the degradation of TCE in UV/H_2O_2 process.

2.4.3.2 Drinking water equivalent level

Drinking water equivalent level (DWEL) is a lifetime exposure concentration protective of adverse non-cancer health effects from drinking water (U.S. EPA, 2012). Table 2.7 shows the DWEL of major species for the degradation of TCE in UV/H_2O_2 process. These DWEL are obtained from the 2012 edition of the drinking water standard and health advisories (U.S. EPA, 2012). With equation (2-19), we can calculate the overall relative toxicity (RT) profile with respect to DWEL.

$$RT = \sum_{i=1}^{n} \frac{C_i}{DWEL_i} \qquad (2\text{-}19)$$

where n is the number of stable species, i refers to the sets of all stable species, and C_i is the concentration. Figure 2.12 shows the calculated overall relative toxicity profile with respect to DWEL. As the major species for the degradation of acetone in UV/H_2O_2 are not included in the EPA drinking water standards and health advisories, the DWEL of

these species and the overall relative toxicity with respect to DWEL for acetone degradation are not available.

Table 2.7 Drinking water equivalent level (DWEL) of major species for the degradation of TCE in UV/H_2O_2 process

Speices*	DWEL (mg/L)
Trichloroethylene (TCE)	0.2
Monochloroacetic acid (MCA)	0.35
Dichloroacetic acid (DCA)	0.1

* Oxalic acid and formic acid are not included in the EPA drinking water standards and health advisories.

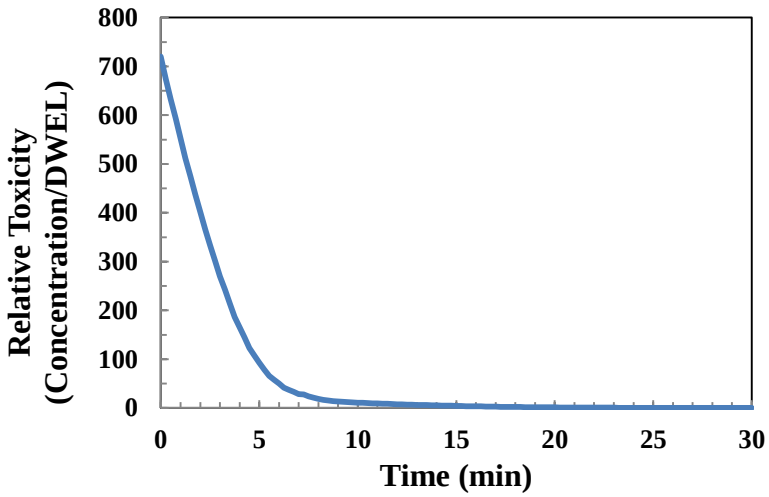

Figure 2.12. Calculated profile of overall relative toxicity with respect to DWEL for the degradation of TCE in UV/H_2O_2 process.

2.4.3.3 10^{-4} cancer risk concentration

10^{-4} cancer risk concentration is the concentration of a chemical in drinking water corresponding to an excess estimated lifetime cancer risk of 1 in 10,000 (U.S. EPA, 2012). Table 2.8 shows the 10^{-4} cancer risk concentrations of major species for the degradation of TCE in UV/H_2O_2 process. These 10^{-4} cancer risk concentrations are obtained from the 2012 edition of the drinking water standard and health advisories (U.S. EPA, 2012). With equation (2-20), we can calculate the overall relative toxicity (RT) profile with respect to 10^{-4} cancer risk concentration.

$$RT = \sum_{i=1}^{n} \frac{C_i}{10^{-4}\ \text{Cancer Risk Concentration}_i} \qquad (2\text{-}20)$$

where n is the number of stable species, i refers to the sets of all stable species, and C_i is the concentration. Figure 2.13 shows the calculated overall relative toxicity profile with respect to 10^{-4} cancer risk concentration. As the major species for the degradation of acetone in UV/H_2O_2 are not included in the EPA drinking water standards and health advisories, the 10^{-4} cancer risk concentration of these species and the overall relative toxicity with respect to 10^{-4} cancer risk concentration for acetone degradation are not available.

Table 2.8 10^{-4} cancer risk concentration of major species for the degradation of TCE in UV/H_2O_2 process

Speices*	10^{-4} cancer risk concentration (mg/L)
Trichloroethylene (TCE)	0.003
Monochloroacetic acid (MCA)	-
Dichloroacetic acid (DCA)	0.1

* Oxalic acid and formic acid are not included in the EPA drinking water standards and health advisories. The 10^{-4} cancer risk concentration of MCA is not available.

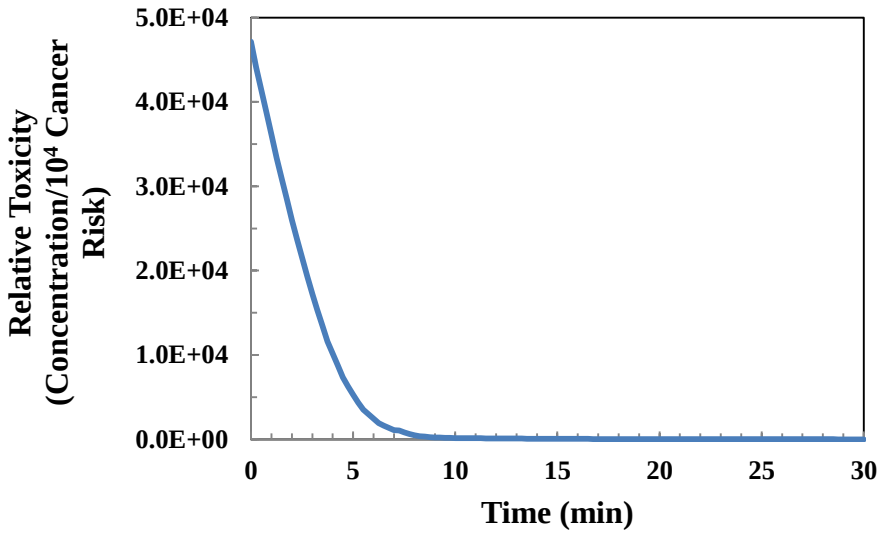

Figure 2.13. Calculated profile of overall relative toxicity with respect to 10^{-4} cancer risk concentration for the degradation of TCE in UV/H_2O_2 process.

CHAPTER 3

COMPUTER-BASED FIRST-PRINCIPLES KINETIC MONTE CARLO SIMULATION OF POLYETHYLENE GLYCOL DEGRADATION IN AQUEOUS PHASE UV/H_2O_2 ADVANCED OXIDATION PROCESS

3.1 Abstract

We have developed a computer-based first-principles kinetic Monte Carlo (CF-KMC) model to predict degradation mechanisms and fates of intermediates and byproducts produced from the degradation of polyethylene glycol (PEG) in the presence of hydrogen peroxide (UV/H_2O_2). The CF-KMC model is comprised of a reaction pathway generator, a reaction rate constant estimator, and a KMC solver. The KMC solver is able to solve the predicted pathways successfully without solving ordinary differential equations. The predicted time-dependent profiles of averaged molecular weight, and polydispersitivity index (i.e., the ratio of the weight averaged molecular weight to the number averaged molecular weight) for the PEG degradation were validated with experimental observations. These predictions are consistent with the experimental data. The model provided detailed and quantitative insights into the time evolutions of molecular weight distribution and concentration profiles of low molecular weight products and functional groups. Our approach may be useful to predict the fates of degradation products for a wide range of complicated organic contaminants.

3.2 Introduction

Polyethylene glycol (PEG) is a soluble polymer that is widely used as surfactants, cosmetics, personal lubricants, and explosives (Santos et al., 2009; Santos et al., 2011).

Once it is used, PEG is generally discarded into municipal waste water treatment facilities. However, the conventional activated sludge-based wastewater treatment systems are not able to remove PEG effectively because of its low biodegradability (Aarthi et al., 2007). As a result, PEG may finally be released into the environment, which causes negative environmental impacts including being toxic to soil microbes and animals, reducing the soil fertility, and transporting heavy metals through the environment (Swift et al., 1993; Morlat et al., 2003).

Advanced oxidation processes (AOPs) have been successfully applied as effective technologies for PEG treatment in the aqueous phase. Hydroxyl radicals (i.e., HO•) that are produced in AOPs react rapidly with PEG and degrade PEG via the radical-involved chain reactions. Extensive experiments have been conducted on PEG degradation by various AOPs. Santos *et al.*(Santos et al., 2009) oxidized PEG using the UV/H_2O_2 process, achieving 50% decrease of the weight average molecular weight (M_w) after 30 min irradiation with light intensity of 1.63×10^{-5} Einstein/L s and hydrogen peroxide dosage of 0.15 M. Santos *et al.*(Santos et al., 2009) also identified oxalic acid, glycolic acid, and formic acid as major byproducts. Santos *et al*. (Santos et al., 2011) degraded PEG with the photo-Fenton process, reducing the M_w by 50% after 10 min treatment and observing a concomitant increase in polydispersity index (PDI) and number of average chain scission. Giroto *et al*. (Giroto et al., 2010) investigated the removal of total organic carbon (TOC) for the degradation of PEG in the photo-Fenton process under various conditions. Vijayalakshmi *et al*. (Vijayalakshmi et al., 2006) studied the photocatalytic degradation of PEG using combustion synthesized nano-size TiO_2 catalyst and Chang *et al*. (Chang et al., 2001) applied UV/O_3 process for PEG treatment.

Although various experimental studies have been reported on the degradation of PEG in AOPs, few studies have developed kinetic models that can predict the performance of AOPs for PEG degradation. Ghafoori *et al.* (Ghafoori et al., 2012a; Ghafoori et al., 2012b) developed kinetic models that can predict time-dependent profiles of the number averaged molecular weight (M_n), the number of chain scission per molecules, and the total organic carbon (TOC) removal for the PEG degradation in UV/H_2O_2 process. Although these models were able to predict the PEG degradation behavior in reasonable agreement with the experimental data, they are limited in the following two aspects. First, these models used lumped species to represent various polymer radicals. As a result, the model predictions do not include the fates of intermediates, byproducts, and functional groups that are possibly produced. Second, these models require numerical solvers to solve ordinary differential equations (ODEs), which might be too stiff to be solved for complicated mechanisms (Vinu et al., 2012).

One attractive method to overcome the limitations of conventional ODEs-based empirical model is to develop a computer-based first-principles kinetic Monte Carlo (CF-KMC) model. The CF-KMC model predicts the time-dependent fate of a given target compound and associated intermediates and byproducts based on the automated reaction pathway generator and the reaction rate constant predictor. The reaction pathway generator predicts all possible elementary reactions and intermediates and byproducts based on the known reaction rules discovered from past experimental observations. The CF-KMC model also uses a KMC solver to solve the predicted pathways without solving ODEs. Hence, difficulties such as stiffness encountered by the conventional ODEs-based empirical model can be avoided. The KMC solver has been successfully applied for

various polymerization chemical reactions, including the depolymerization of poly(veratryl β-guaiacyl ether) (McDermott et al., 1990), the hydrolytic depolymerization of cellobiose and amylose (Pinto et al., 1991), the inverse emulsion polymerization of acrylamide (Platkowski et al., 1999), and the pyrolysis of poly(styrene peroxide) (Vinu et al., 2012). There has been no attempts of the KMC solver application to the reaction systems in AOPs. It should be noted that a computer-based first-principles kinetic (CFK) model has recently been developed (Guo et al., 2014a). This CFK model also used automated reaction pathway generator and the reaction rate constant estimator to predict the degradation pathways and fates of byproducts produced during aqueous phase AOPs. However, since this CFK model required a numerical solver to solve ODEs, this CFK model can only simulate the degradation of low molecular weight target compound and might have difficulty of stiffness for solving the ODEs of the degradation of large molecular weight target compound, such as polymers.

In this study, a CF-KMC model is developed for the degradation of PEG in the UV/H_2O_2 process. Detailed mechanisms for the degradation of PEG and fates of intermediates and byproducts are generated and time-dependent profiles of weight averaged molecular weight (M_w), PDI, and molecular weight distribution (MWD) are calculated. The evolvements of low molecular weight products (LMWPs) and functional groups are also predicted. The simulation results are validated with experimental data.

3.3 Methods

3.3.1 Overall methodology

Figure 3.1 displays the major structure of CF-KMC model. The first component is a pathway generator that has been developed previously (Li et al., 2009), which can

automatically predict elementary reactions included in the degradation pathways for the aqueous phase AOPs based on the known reaction rules discovered from the past experimental observations. These reaction rules involve hydrogen-atom abstraction reaction from a C-H bond or O-H bond, HO• addition reaction to a C=C bond of an aliphatic compound, oxygen addition reaction to organic radicals, bimolecular decay of peroxyl radical reaction, HO_2• elimination reaction, β scission reaction, 1,2-H shift reaction, hydrolysis reaction and so forth.

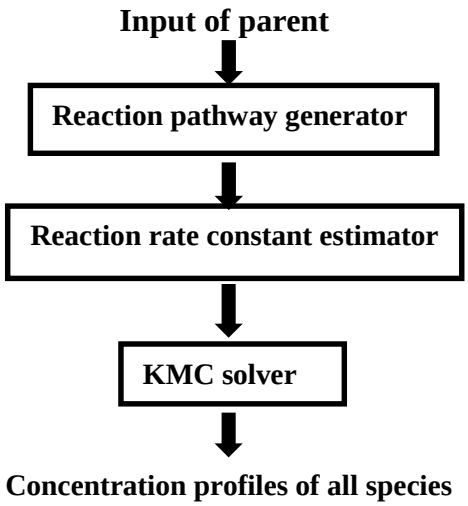

Figure 3.1. Structure and flow of a computer-based KMC model.

The second component is to estimate the reaction rate constants for each elementary reaction predicted by the pathway generator. For this study, we used a Group Contribution Method (GCM) (Minakata et al., 2009) to estimate the rate constants of aqueous phase HO• reactions (i.e., hydrogen-atom abstraction reaction by HO• and HO• addition to unsaturated bond reaction). For other reactions, the rate constants are either obtained from literature-reported values or predicted based on similar reactions in literature.

The third component is a KMC solver, which is proposed by Gillespie (Gillespie et al., 1977). The KMC solver uses populations, which are proportional to molar concentrations, to represent the amounts of species. To initiate the simulation, users need to input the initial population for all species employed in the KMC solver. Then, the KMC solver iteratively executes following four steps to simulate the reacting process at each time point. The first step is to calculate a probability of occurrence of each reaction with the following equation:

$$P_j = \frac{r_j}{\sum_{i=1}^{m} r_i} \tag{3-1}$$

where P_j is a probability of occurrence of reaction j, r_j is the rate of reaction j, and m is the number of reactions in the system. The rate of each reaction can be calculated by

$$r_j = k_j^{pop} \prod_i N_j^i \tag{3-2}$$

where k_j^{pop} is the rate constant of reaction j based on the populations of species, N_j^i is the population of reactant i in reaction j. k_j^{pop} can be obtained from the molar concentration-based rate constant, k_j^{conc}. For instance, $k_j^{pop} = \theta k_j^{conc}$ for the zero-th order reactions, $k_j^{pop} = k_j^{conc}$ for the first order reactions, and for $k_j^{pop} = \frac{k_j^{conc}}{\theta}$ for the second order reactions, where θ is the value of population corresponding to 1 mole/L of molar concentration. The second step is to select a reaction to occur based on its probability of occurrence with the following equation

$$\sum_{i=1}^{\mu-1} P_i < x_1 < \sum_{i=1}^{\mu} P_i \tag{3-3}$$

where μ is the index of the reaction that is selected, x_1 is a random number between 0 and 1. The third step is to execute the selected reaction and update the populations. During this step, the population of each reactant in the selected reaction will be decreased by one and the population of each product in the selected reaction will be increased by one. The fourth step is to calculate the time interval for the next time point with the following equation

$$\tau = \frac{1}{\sum_{i=1}^{m} r_i} \ln\left(\frac{1}{x_2}\right) \tag{3-4}$$

where τ is the time interval, x_2 is another random number between 0 and 1. A cycle of four steps is executed iteratively at each time point until the target time point is achieved. By tracking the population of each species at various time points, we can obtain the time-dependent concentration profiles of each species.

To validate the KMC solver, we solved the degradation mechanisms of acetone and trichloroethylene (TCE) in UV/H_2O_2 process by both solving the ordinary differential equation (ODE) and the KMC solver. For each parent compound, we compared the calculated concentration profiles of major species for the ODE solver and the KMC solver. From Figure 3.2 and Figure 3.3, we can find that for both acetone and TCE, the concentration profiles solved by the KMC solver match the concentration profiles solved by the ODE solver very well.

For this validation, the degradation mechanisms of both parent compounds were predicted by the pathway generator and the reaction rate constants were obtained by three ways: (1) directly obtained from literature, (2) estimated based on similar reactions and (3) estimated by group contribution method (GCM) (Minakata et al., 2009). The initial

conditions were listed in Table 3.1 and the elementary reactions can be found in Guo *et. al.* (Guo et al., 2014a)

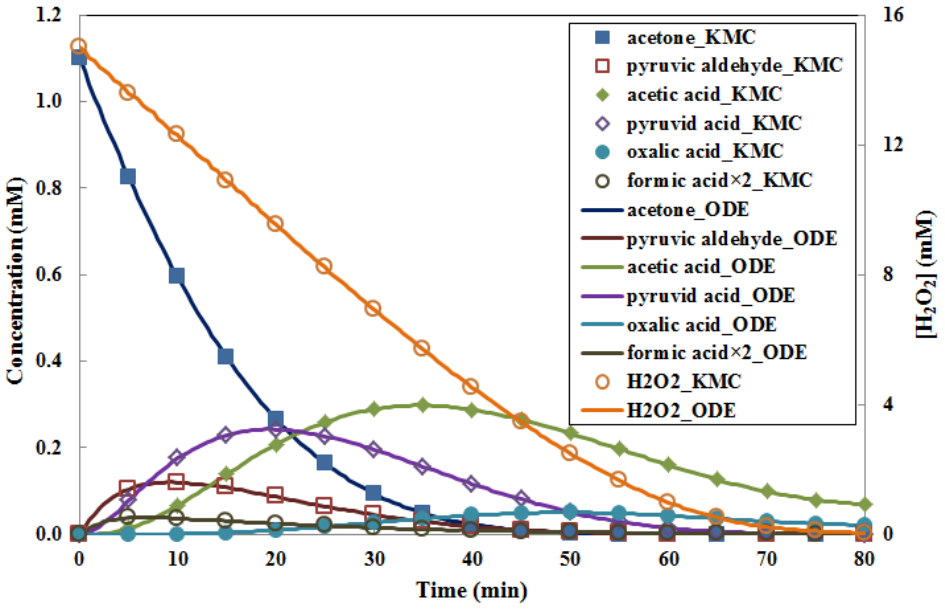

Figure 3.2. Comparison of concentration profiles of major species solved by ODE solver and KMC solver for the degradation of acetone in UV/H_2O_2 process.

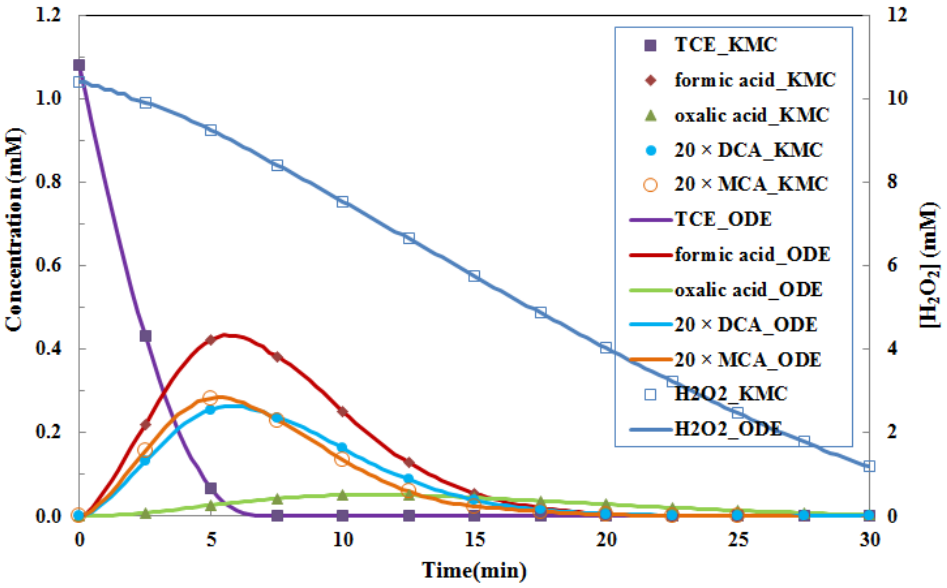

Figure 3.3. Comparison of concentration profiles of major species solved by ODE solver and KMC solver for the degradation of TCE in UV/H_2O_2 process.

Table 3.1. Initial conditions for the simulations of the degradation of acetone and TCE in UV/H_2O_2 process

Parent compound	Acetone	TCE
Initial concentration (mM)	1.1	1.08
Initial concentration of H_2O_2 (mM)	15.0	10.4
Initial pH	5.9	5.9
UV wavelength (nm)	200-300	200-300
UV intensity (Einstein/L•s)	7.79×10^{-6}	7.79×10^{-6}
Reactor type	Completely mixed batch reactor	Completely mixed batch reactor

3.3.2 Detailed information about the implementation of the computer-based first-principles KMC model

The data structure that was used in our CF-KMC model to represent one polymer molecule is shown in Figure 3.4.

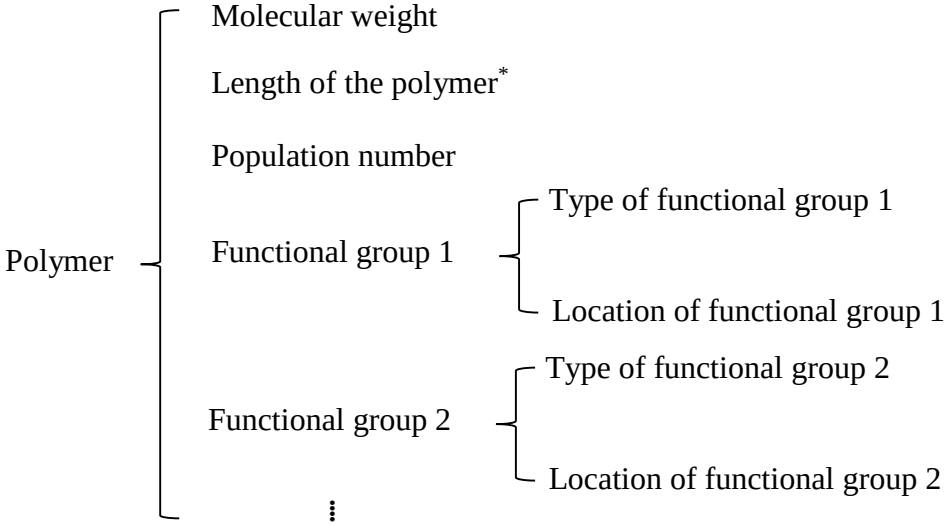

Figure 3.4. Data structure to represent polymer molecules in the CF-KMC model.
*Length of the polymer means the number of repeated monomer units that are contained in the polymer.

From the above figure, we can see that for each polymer, we store the information about molecular weight, length, population number, and types and locations of functional groups for this polymer.

The overall simulation process of the PEG degradation using the CF-KMC model is consisted of three stages. The first stage is to generate the complete degradation pathway of the PEG with the pathway generator. The pathway generator is a computer algorithm that can automatically generate the degradation pathway for the aqueous phase AOPs with reaction rules discovered by previous experiments. For the degradation of the PEG, the pathway generator can make a library that contains the generalized reaction rules for the PEG degradation as listed in the Table C.1 in Appendix C. These generalized reaction rules are discovered by previous experiments. For each polymer, the pathway generator automatically identifies the functional groups in this polymer and predicts potential reactions that can occur for these functional groups based on the generalized reaction rules. These potential reactions are stored in a reaction pool and the information (e.g., length, molecular weight, and types and locations of functional groups) about the products that are produced from these potential reactions is also stored. Then, these products are fed to the pathway generator again as the inputs and new species that can be produced from these products are generated and stored. The above process is performed iteratively until there is no more new species that can be produced. For the degradation of PEG in our study, we totally predicted 522,057 species and 696,183 reactions by the pathway generator. The detailed information about the pathway generator can be found in Li *et. al*. (Li et al., 2009)

The following example shows how we use the pathway generator to predict the degradation of a PEG molecule. First, we make the data structure of the PEG molecule as the input to the pathway generator as shown in Figure 3.5. Then, the pathway generator automatically predicts hydrogen-atom abstraction reaction pathway by HO•. As an example, we only show the situation where the 80th carbon of the polymer chain is attacked as an example. At last, the pathway generator store this predicted reaction in the reaction pool and generates the data structure of the product which has the information about the type and location of the produced functional group, inner-carbon-centered radical. This product will be fed to the pathway generator again as the input and new species will be produced. This process will be performed iteratively until no more new species are produced.

PEG

Molecular weight	3520 g/mole
Length of the polymer	80
Population number	10^7

Pathway generator

Product

Molecular weight	3551 g/mole
Length of the polymer	80
Population number	0
Type of functional group	Inner-carbon-centered radical
Location of function group	On 80^{th} carbon

Figure 3.5. Example of how the pathway generator predicts the degradation of a PEG molecule.

The second stage of the overall simulation process is to obtain the reaction rate constants for all reactions (i.e., 696,183 reactions) that are stored in the reaction pool. For hydroxyl radical reactions, we used the Group Contribution Method (GCM) to predict the reaction rate constants. For other reactions, the rate constants are either obtained from literature or estimated based on similar reactions. The detailed information about how the GCM estimates reaction rate constants can be found in Minakata *et. al*. (Minakata et al., 2009)

The third stage of the overall simulation process is to run the KMC solver to solve the generated degradation mechanism of PEG. As stated above, at each time point, the KMC solver selects one reaction to occur from the reaction pool and updates the population numbers that are stored in the data structures of the reactants and products in this selected reaction.

3.4 Results and Discussions

3.4.1 Computer-based First-principles Kinetic Monte Carlo Simulation

The degradation of PEG in the UV/H_2O_2 process was simulated by the CF-KMC model. The initial concentration of hydrogen peroxide was 0.15 M. The initial concentration and molecular weight of PEG were 0.18 mM and 3500 g/mol, respectively. The wavelength of UV light was 254 nm and the light intensity was 1.63×10^{-5} Einstein/L s. The initial pH was 5.9. The reactor type was completely mixed batch reactor (CMBR). These conditions were those that were used for the experiments by Santos *et al*. (Santos et al., 2009) and Ghafoori *et al.* (Ghafoori et al., 2012) The

elementary reactions included in the degradation mechanism of PEG in UV/H_2O_2 process were generated by the pathway generator as shown in Table C1 in Appendix C. The generated degradation mechanism has 522,057 species and 696,183 reactions. It is noted that the current version of pathway generator does not include the hydrogen-atom abstraction reaction by oxyl radical, which might have significant impact on the PEG degradation process (Kaczmarek et al., 1995). As a result, this reaction was manually added into the reaction pathway.

The reaction rate constants for elementary reactions generated above were preliminarily obtained in two ways: directly from literature or estimated by GCM (Minakata et al., 2009). The GCM predicts HO• reaction rate constants within 0.5-2 times of the experimental values. Reaction rate constants that could not be obtained by these two ways were estimated based on similar reactions which had experimental values. Table C.1 in Appendix C contains the values of all reaction rate constants and how they were obtained or estimated. To evaluate the importance of each reaction rate constant to the simulation results of the computer-based first-principles KMC model, we applied the one-at-a-time (OAT) sensitivity analysis to the generated degradation mechanism of PEG in UV/H_2O_2 process. The OAT sensitivity analysis increased each reaction rate constant by 10% in turn and calculated the sensitivity coefficient (SC) of each reaction by the following equation

$$\mathrm{SC}_i = \frac{1}{M+N}\left(\sum_{m=1}^{M}\frac{\left|M_{w,m}^{changed} - M_{w,m}^{original}\right|}{M_{w,m}^{original}} + \sum_{n=1}^{N}\frac{\left|C_n^{changed} - C_n^{original}\right|}{C_n^{original}}\right) \quad (3\text{-}5)$$

Where M is the total number of data points for averaged molecular weight (M_w); N is the total number of data points for concentrations of low molecular weight products

(LMWPs); $M_{w,m}^{original}$ is the M_w before the rate constant of reaction *i* is changed; $M_{w,m}^{changed}$ is the M_w after the rate constant of reaction *i* is changed; $C_n^{original}$ is the concentration of LMWPs before the rate constant of reaction *i* is changed; $C_n^{changed}$ is the concentration of LMWPs after the rate constant of reaction *i* is changed. A reaction rate constant with high SC indicates that this reaction rate constant is important to the overall simulation results.

Table C.2 in Appendix C shows the sensitivity analysis results for the generated degradation mechanism of PEG in UV/H_2O_2 process. From this table, we can find that the reaction rate constants that have significant impact on the simulation results (i.e. SC > 0.005) are consisted of two reaction types: (1) hydrogen abstraction reaction by hydroxyl radical and (2) special reactions that involves the radical reactions between H_2O_2, HO•, and HO_2•/O_2^-•. The reaction rate constants of these two reaction types can either be obtained directly from literature or estimated by the GCM (Minakata et al., 2009). Table C.2 also shows that the reaction rate constants that are estimated based on similar reactions have minor impacts (i.e. SC < 0.005) on the simulation results.

Because the OAT sensitivity analysis is a local sensitivity analysis that requires baseline values for all reaction rate constants before the analysis and can only reflect the importance of each reaction rate constant in a small range around the baseline value, these baseline values may have impact on the sensitivity analysis results. As a consequence, we applied multiple times of OAT sensitivity analysis under various baseline values of reaction rate constant of each type of reaction. These varied baseline values cover the possible range of each type of reaction rate constant as shown in Table 3.2. We found that the sensitivity analysis results are same for various baseline values of reaction rate constants within the possible ranges.

Table 3.2. Possible ranges of different types of reaction rate constants in AOPs

Reaction type	Possible range of reaction rate constant	Reference
H-abstraction reaction by hydroxyl radical	10^7 $M^{-1}s^{-1}$ to 10^9 $M^{-1}s^{-1}$	Buxton et al., 1988
Oxygen addition to carbon-centered radical	10^8 $M^{-1}s^{-1}$ to 10^{10} $M^{-1}s^{-1}$	Neta et al., 1996
Bimolecular decay of peroxyl radical	10^8 $M^{-1}s^{-1}$ to 10^9 $M^{-1}s^{-1}$ for primary and secondary preroxyl radical; 10^4 $M^{-1}s^{-1}$ to 10^5 $M^{-1}s^{-1}$ for tertiary preroxyl radical	Neta et al., 1990
HO_2• elimination reaction	10 s^{-1} to 10^5 s^{-1}	Neta et al., 1990
β scission reaction	10^4 s^{-1} to 10^7 s^{-1}	Li et al., 2009

The degradation pathway of PEG was solved by the KMC solver. As mentioned above, the KMC solver requires users to input initial populations of species, which might have impact on the accuracy of the simulation of the CF-KMC model (Vinu et al., 2012). To quantitatively evaluate this impact, we calculated the sample deviation (SD) for various initial populations of PEG. The SD is the relative error between M_w that is obtained from experimental measurement and CF-KMC model calculation. The SD can be calculated by

$$SD = \sqrt{\frac{1}{N-1}\sum_{i=1}^{N}\left[(M_{w,exp,i} - M_{w,cal,i}) / M_{w,exp,i}\right]^2} \quad (3\text{-}6)$$

where N is the number of data points; $M_{w,exp,\,i}$ and $M_{w,cal,\,i}$ are the experimental and calculated weight averaged molecular weight, respectively; and i refers to the set of time points where experimental data are available. Table 3.3 shows that increasing the initial population of PEG decreases the SD value (i.e., increase the accuracy of the CF-KMC

model) until the initial population equals to 5×10^5, after which the SD value does not change. In addition, Table 3.3 also shows that increasing the initial population of PEG continuously and significantly increases the CPU time for the simulation. As we want to build a CF-KMC model which is accurate and computational efficient, we chose the initial population of PEG of 5×10^5 for further analysis.

Table 3.3. Changes in SD value and CPU time of the computer-based first-principles KMC model as a function of initial population of PEG. The processor used is 64-bit 2.4 GHz Intel® Core™ 2 Duo CPU

Initial population of PEG	SD value	CPU time (min)
10^4	0.49	5.3
10^5	0.37	10.4
5×10^5	0.34	20.2
10^6	0.33	40.7
5×10^6	0.33	90.1

3.4.2 Predicted Reaction Pathways of PEG Degradation

The CF-KMC model predicted various functional groups that were produced during the degradation of PEG in the UV/H_2O_2 process. These functional groups included hydroxyl group, aldehyde group, carboxylic acid group, and ester group, which were experimentally observed by Kaczmarek *et al* (Kaczmarek et al., 1995). The major low molecular weight products (LMWPs) predicted by the CF-KMC model included formic acid, oxalic acid, glycolic acid, and ethyleneglycol (EG), which were identified by the experiment conducted by Santos *et al* (Santos et al., 2009). The CF-KMC model also predicted minor LMWPs including formaldehyde, glycolaldehyde, and glyoxalic acid. These minor LMWPs have not been measured by experiments, because they may have low concentrations due to their high reactivity toward HO•. However, the formation of these minor LMWPs have been proposed by various studies (Santos et al., 2009; McGinnis et al., 2000).

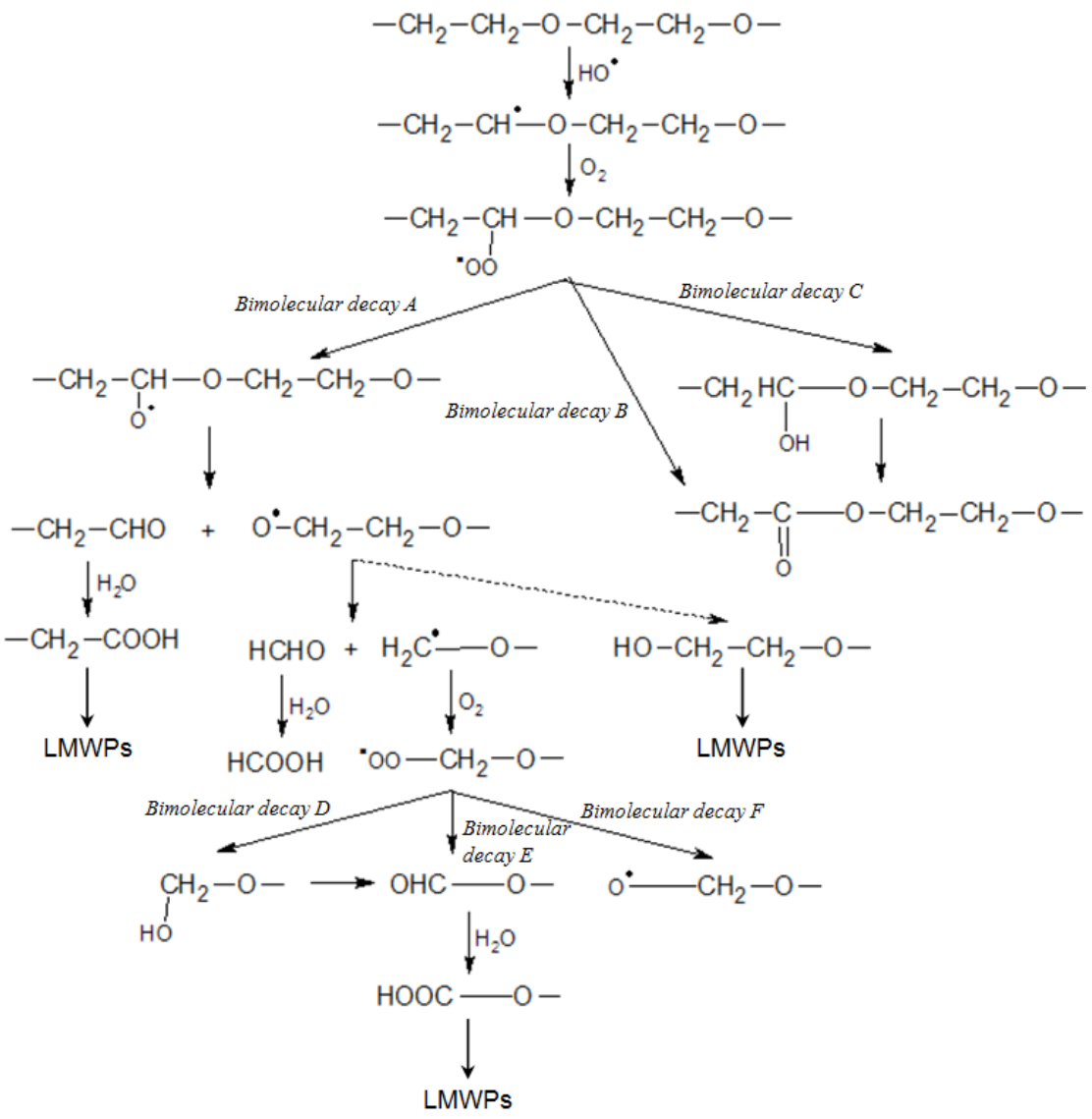

Figure 3.6. Generated degradation mechanism of PEG in UV/H_2O_2 process. Dashed lines represent manually added reactions. Solid lines represent generated reactions by the pathway generator.

Figure 3.6 shows the degradation mechanism of the PEG that is generated by the pathway generator. At the first step, the hydrogen atom in the backbone of PEG molecule is abstracted by HO•, which yields inner-carbon-centered radical. Generally, there are two ways for HO• to attack the polymer chain: HO• can randomly attack the polymer chain, which later leads to the chain cleavage occurring at random positions along the polymer chain (i.e., random scission) (Santos et al., 2009; Vijayalakshmi et al., 2006;

Kaczmarek et al., 1995); or HO• only attacks the terminal of the polymer chain and the cleavage occurs only at the end of the chain with monomers released (i.e., chain-end scission) (Ghafoori et al., 2012a). The CF-KMC model showed that the contribution of the chain-end scission scheme to the overall PEG degradation is minor, which is consisted with the conclusions of other studies (Santos et al., 2009; Kaczmarek et al., 1995).

The inner-carbon-centered radical generated by H-atom abstraction reacts rapidly with O_2 to form the inner-peroxyl radical, ─ CH_2─CH(OO•)─O─CH_2─CH_2─O─. This inner-peroxyl radical is proposed to be consumed by three bimolecular decay channels (i.e. bimolecular decay A, B, and C in Figure 3.6) corresponding to the formation of three different byproducts, respectively. First, the inner-peroxyl radical produces the inner-hydroxyl group via the Russell reaction (i.e. bimolecular decay C in Figure 3.6) (Russell, 1957). This inner-hydroxyl group is further degraded to the inner-ester bond. Second, the inner-peroxyl radical also directly produces inner-ester bond at the backbone of the polymer chain (i.e., bimolecular decay B in Figure 3.6). The generated polymer chain with inner-ester bond undergoes randomly attack by HO• again, which finally leads to the formation of various LMWPs. Third, the inner-peroxyl radical produces inner-oxyl radical, ─CH_2─CH(O•)─O─CH_2─CH_2─O─ (i.e., bimolecular decay A in Figure 3.6). The contributions of these three consumption pathways for the inner-peroxyl radical are the same.

The inner-oxyl radical, ─CH_2─CH(O•)─O─CH_2─CH_2─O─, decays through fast unimolecular fragmentation by C─O bond scission to form two sub-chains ended with aldehyde group and oxyl radical, respectively (i.e., ─CH_2─CHO and •O─CH_2─

CH_2─O─ in Figure 3.6). On one side, the end-aldehyde group, ─CH_2─CHO, further hydrolyzes to an end-carboxylic acid group ─CH_2─COOH. The polymer chain with end-carboxylic acid group is randomly attacked by HO• to produce various LMWPs. On the other side, the end-oxyl radical, •O─CH_2─ CH_2─O─, decays by two channels: first, the end-oxyl radical abstracts hydrogen-atom from the backbone of the polymer chain to form end-hydroxyl group, HO─CH_2─ CH_2─O─; second, the end-oxyl radical decays through unimolecular fragmentation by C─C bond scission to form formaldehyde and end-carbon-centered radical, •CH_2─O─, which rapidly reacts with O_2 to form the end-peroxyl radical, •OOCH_2─O─.

The end-peroxyl radical, •OOCH_2─O─, has three different bimolecular decay channels (i.e., bimolecular decay D, E, and F in Figure 3.6), which produce the end-hydroxyl group, the end-aldehyde group, and the end-oxyl radical, respectively. The degradation pathways for the polymer chain with these terminal groups have been described above. The contributions of these three consumption pathways for the end-peroxyl radical are the same.

3.4.3 Time Evolution of Averaged Molecular Weight and Polydispersitivity

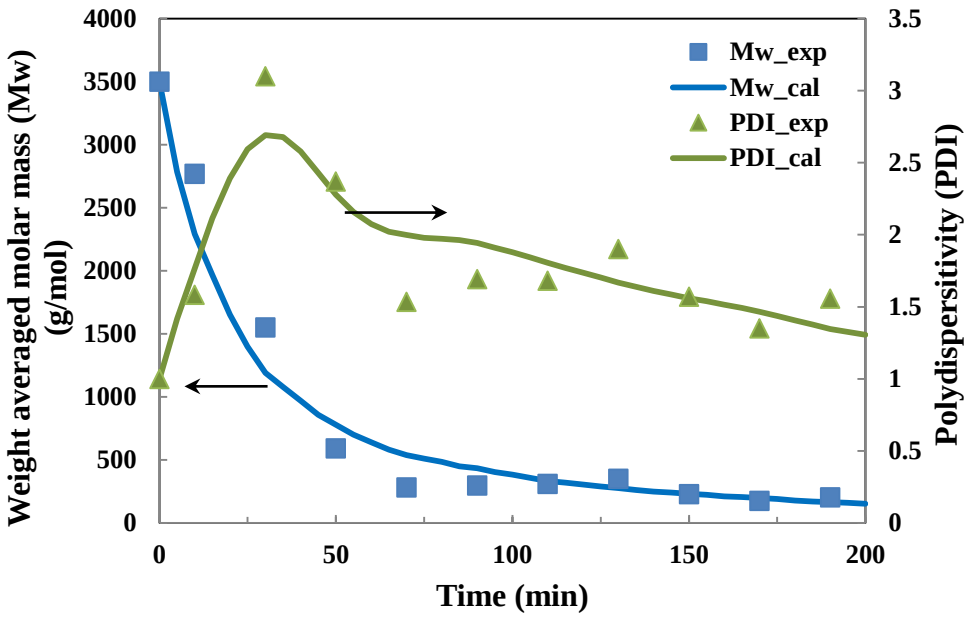

Figure 3.7. Comparison of profiles of weight averaged molecular weight and polydispersitivity between experimental data (Santos et al., 2009) and calculated data for the degradation of PEG during UV/H_2O_2 process.

Figure 3.7 shows the calculated profile of M_w and experimentally-obtained values by Santos *et al* (Santos et al., 2009). We can see that M_w exponentially decreases from 3500 g/mol to 500 g/mol during the initial 50 min oxidation, which indicates that the large PEG molecules can be degraded into small oligomers rapidly during initial stage of the UV/H_2O_2 process. Figure 3.7 also shows the calculated profile of PDI, which can be obtained by PDI = M_w/M_n, where M_n is the number averaged molecular weight and M_w is the weight average molecular weight. M_m and M_w are calculated with the following equations

$$M_n = \frac{\sum_{i=1}^{n} M_i N_i}{\sum_{i=1}^{n} N_i} \qquad M_w = \frac{\sum_{i=1}^{n} M_i^2 N_i}{\sum_{i=1}^{n} M_i N_i} \tag{3-7}$$

where n is the maximum length of PEG, M_i is the molecular weight of PEG with length i, N_i is the population number of PEG with length i. The PDI indicates the width of the

MWD. The PDI profile starts from 1, which means all PEG molecules have the same molecular weight at the beginning. Then the PDI rapidly increases to a peak value of 2.8 at around 30 min, which indicates that the PEG molecules are degraded into oligomers with a wide distribution of molecular weight. After 30 min, the PDI value gradually decreases to 1.3, which means the oligomers with various molecular weight are all gradually degraded into small molecular weight oligomers (e.g., dimer, trimer, tetramer) and the MWD of oligomers in the system become uniform again. Given that the CF-KMC model simulation is a first-principles prediction, the calculated M_w and PDI profiles are in good agreement with the experimental data. The discrepancies between the experimental data and calculated results might be caused by the inaccuracies of certain reaction rate constants that are estimated by the GCM or predicted from similar reactions that have experimental values.

To make a detailed investigation of the degradation process of PEG during the UV/H_2O_2 process, we simulated the time evolution of MWD of PEG as shown in Figure 3.8. The shape of MWD can be approximated by gamma distribution (McCoy et al., 1993) as shown in equation (3-8)

$$f(x) = \frac{x^{k-1} e^{-\frac{x}{\theta}}}{\theta^k \Gamma(k)} \qquad \Gamma(k) = \int_0^\infty x^{k-1} e^{-x} dx \tag{3-8}$$

where x is the molecular weight; $f(x)$ is the mass fraction of PEG with molecular weight x; and k and θ are the shape and scale parameters for the gamma distribution, respectively. We see that the peak of MWD shifts from large molecular weight to small molecular weight, which can be quantitatively described by the change of k for gamma distribution. In addition, we can also find that the width of MWD first increases and then decreases

during the degradation, which can be quantitatively described by the change of θ for gamma distribution. These time evolutions of MWD are consistent with the change of M_w and PDI that are mentioned above.

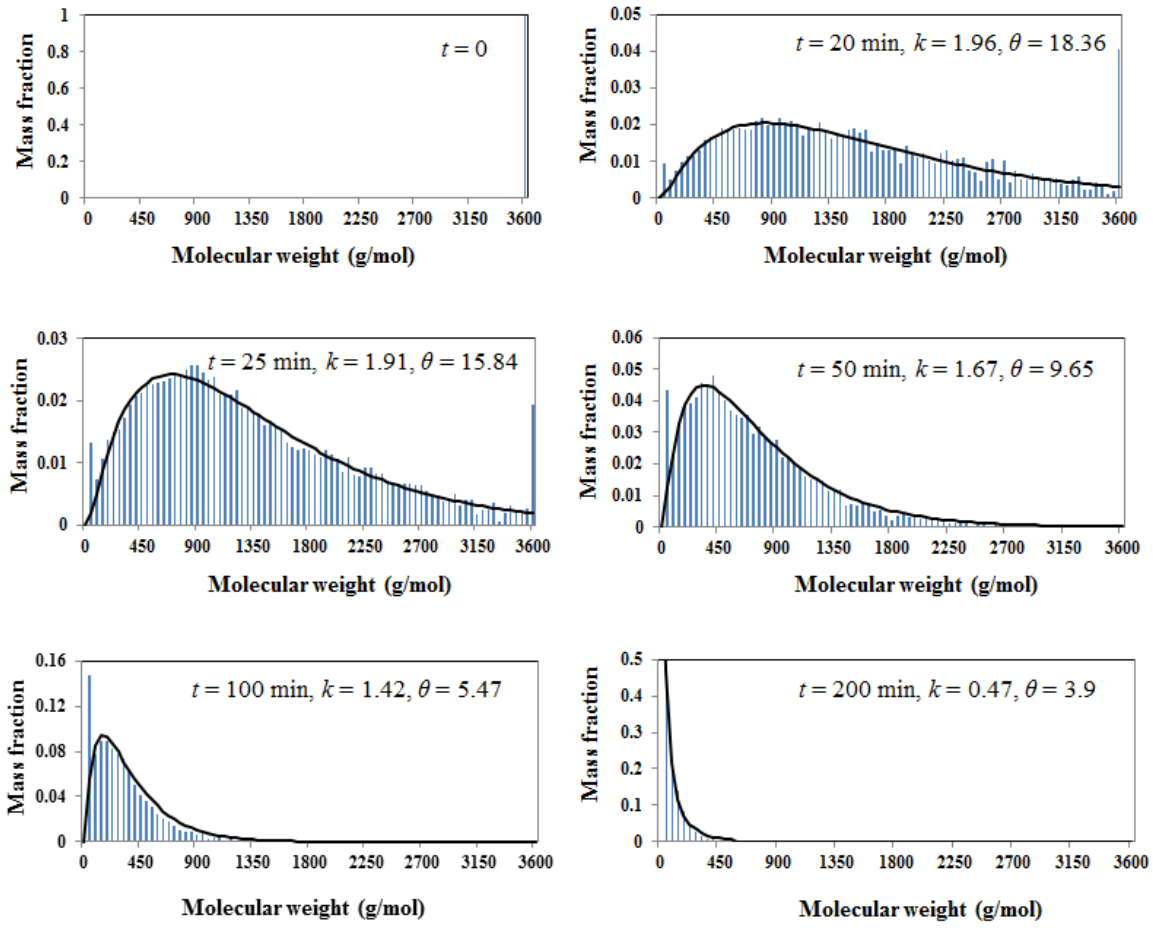

Figure 3.8. Calculated time evolution of molecular weight distribution for the degradation of PEG during UV/H_2O_2 process. Columns are the calculated mass tractions for polymers with various molecular weights. Lines are the fitted gamma distribution. *t* is the time point. *k* and θ are the shape parameter and the scale parameter for the gamma distribution, respectively.

3.4.4 Time Evolution of LMWPs

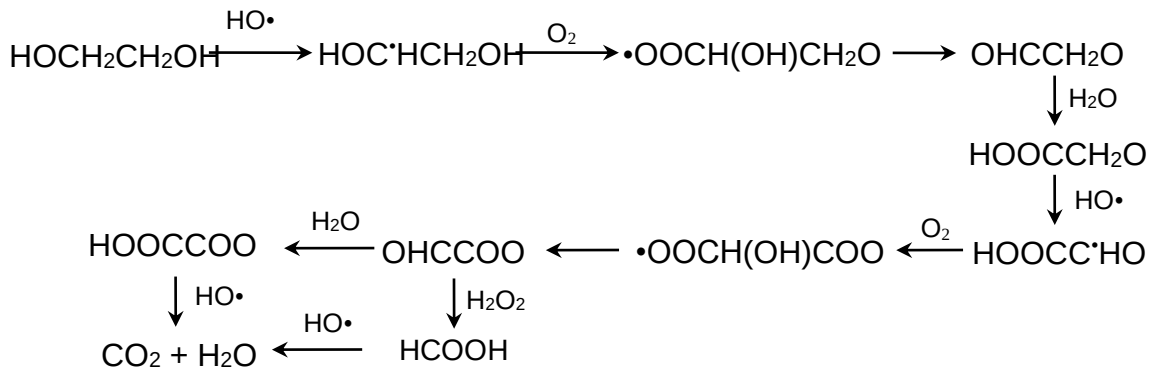

Figure 3.9. Generated degradation mechanism of ethyleneglycol in UV/H_2O_2 process.

Figure 3.9 shows the degradation pathway of one LMWP, ethyleneglycol (EG), that is generated by the pathway generator. As the first step, EG degrades through hydrogen abstraction by HO•, followed by O_2 addition to form the peroxyl radical, •OOCH(OH)CH_2OH. The •OOCH(OH)CH_2OH undergoes HO_2• elimination to form glycolaldehyde, which hydrolyzes to glycolic acid. Then, glycolic acid is degraded to glyoxylic acid by HO• induced hydrogen abstraction and O_2 addition. Glyoxylic acid has two consumption pathways: hydrolyzes to the oxalic acid and reacts with H_2O_2 to form formic acid. Both oxalic acid and formic acid are finally degraded to CO_2 and H_2O. The above description of EG degradation pathway also includes the degradation pathways of other LMWPs (i.e., glycolaldehyde, glycolic acid, oxalic acid, formic acid) as shown in Figure 3.9.

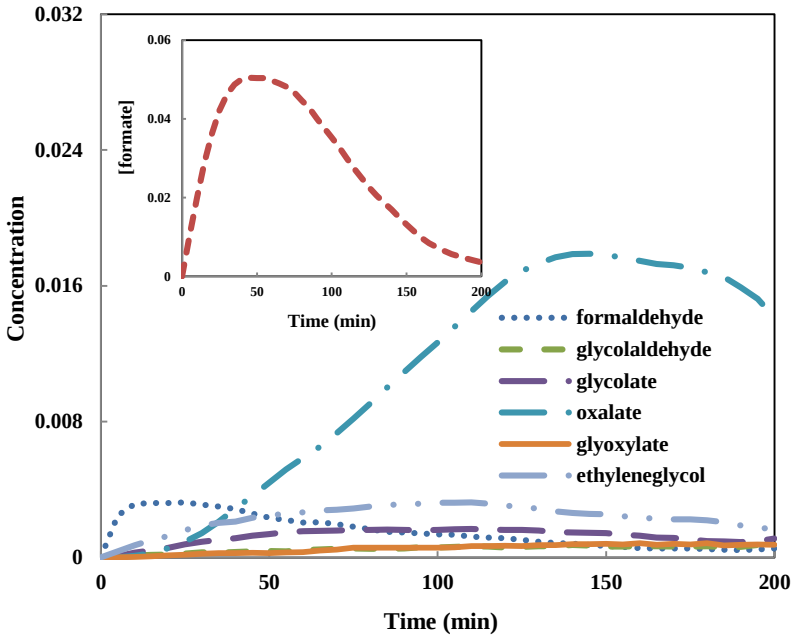

Figure 3.10. Calculated concentration profiles of LMWPs for the degradation of PEG during UV/H_2O_2 process.

Figure 3.10 shows the concentration profiles of LMWPs calculated by the CF-KMC model. Formate is dominant at early degradation stage (i.e., 0-140 min), while oxalate is dominant at a late stage (i.e., 140-200 min). This evolution of dominant LMWPs is resulted from the different formation pathways for formate and oxalate. As shown in Figure 3.9, formate is produced every time the scission of polymer chain (i.e., β scission of ─CH_2─CH(O•)─O─CH_2─CH_2─O─ followed by β scission of •O─CH_2─CH_2─O─) occurs. At early degradation stage, this scission of polymer chain occurs frequently, which produces large amount of formate on one hand. On the other hand, oxalate is produced only from the monomers of PEG. The amount of monomers of PEG is not significant until the end of the degradation stage when more polymer chains are gradually degraded into monomers.

3.4.5 Triethyleneglycol Modeling and Comparison with Literature Data

Since the experimental data of LWMPs for the degradation of PEG was not available, we validated the simulation of LMWPs with experimental data for the degradation of triethyleneglycol (Santos et al., 2009), which is generally used as a model molecule to ascertain the degradation of PEG. In this section, we simulated the degradation of triethylene glycol (3EG) in UV/H_2O_2 process with the computer-aided KMC model and calculated the concentration profiles of 3EG and LMWPs (i.e. diethylene glycol (2EG), ethylene glycol (EG), and formic acid). We compared these calculated concentration profiles with experimental data reported by Santos *et al* (Santos et al., 2009). Figure 3.11 shows that the calculated concentration profiles are in a good agreement with the experimental data. It should be noted that since Santos *et al.* (Santos et al., 2009) only reported time-dependent profiles of peak height for the high performance liquid chromatography (HPLC) for each species, we used these peak heights to represent the relative concentrations of each species in this case.

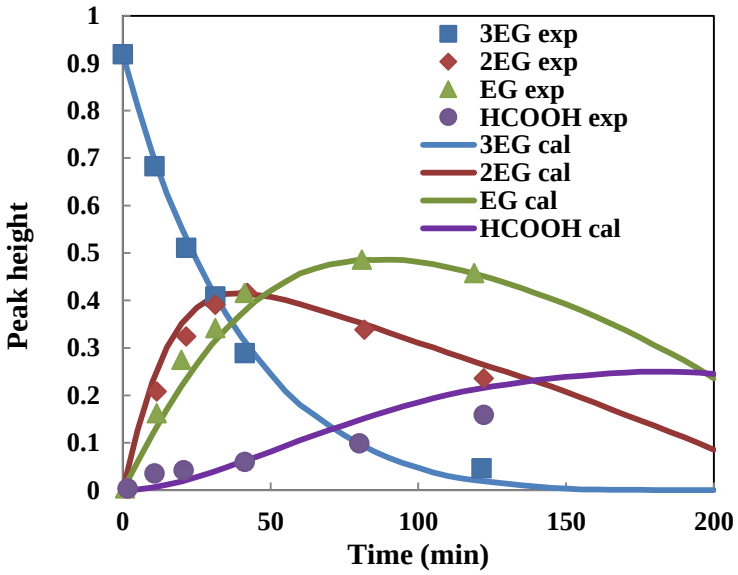

Figure 3.11. Comparison of concentration profiles of 3EG and LMWPs between experimental data (Santos et al., 2009) and predicted data for the degradation of 3EG during UV/H_2O_2 process.

The degradation pathway of 3EG was generated by the pathway generator as shown in Figure 3.12 and the reaction rate constants obtained by three ways: (1) directly obtained from literature, (2) estimated based on similar reactions and (3) GCM (Minakata et al., 2009). The experimental conditions are described by Santos *et al*. (Santos et al., 2009). The initial concentration of hydrogen peroxide was 0.15 M. The initial concentration of 3EG was 0.18 mM. The wavelength of UV light was 254 nm and the light intensity was 1.63×10^{-5} Einstein/L s. The initial pH was 5.9. The reactor type was CMBR.

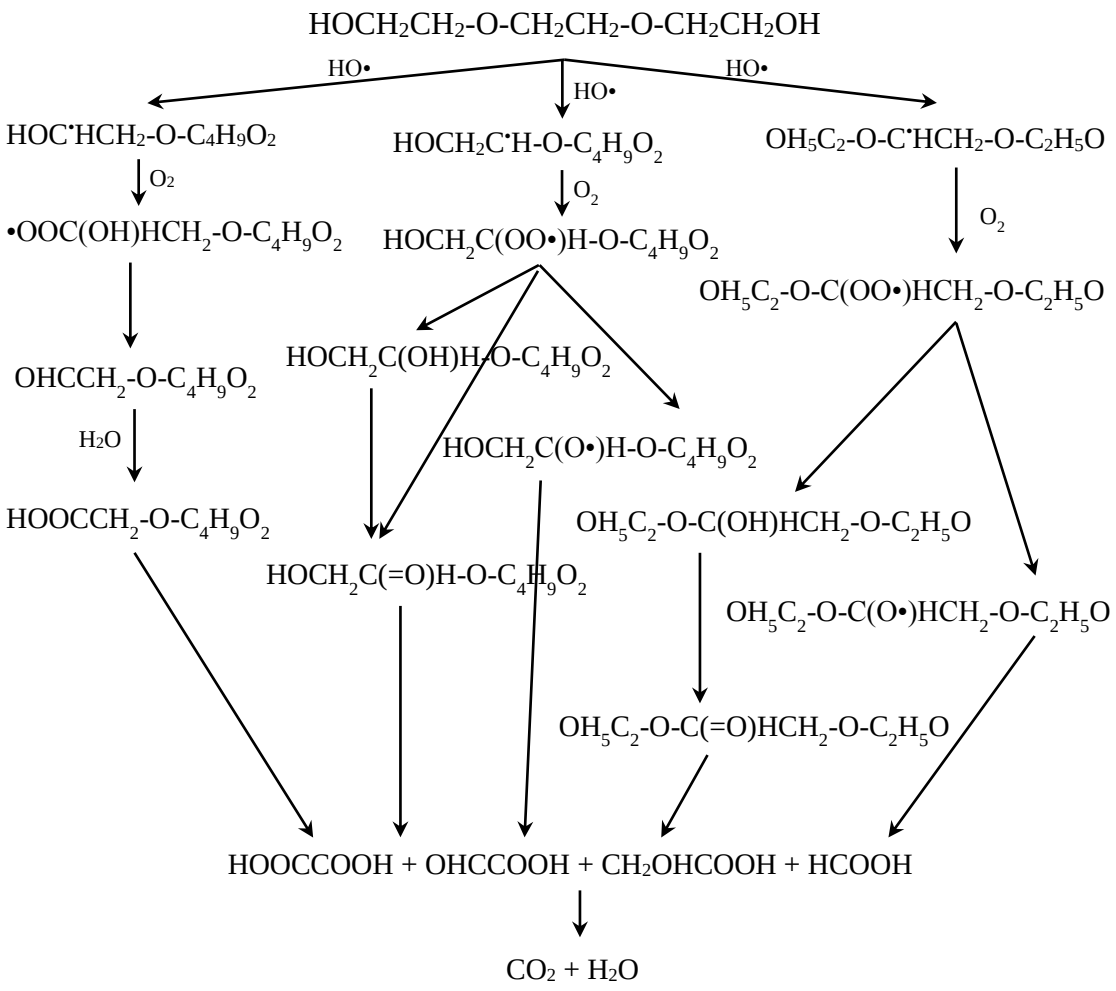

Figure 3.12. Simplified predicted degradation pathway of 3EG.

3.4.6 Time Evolution of Functional Groups

Figure 3.13(a) shows an initial increase of total concentration of the hydroxyl functional groups at an earlier degradation stage (i.e., 0-50 min of the reaction time) followed by a decrease of the concentration at the later degradation stage (i.e., 50-200 min of the reaction time). The peak total concentration of the hydroxyl functional groups is around 0.7 mM. The hydroxyl functional groups consisted of the end and inner hydroxyl groups in the polymer chains. At the beginning, the hydroxyl functional groups consisted of the end-hydroxyl group in the polymer chain as we expect, and then, the

concentration of end-hydroxyl group decreases due to the HO• attack. After 15 min, the inner-hydroxyl group became dominant. In addition, glycolaldehyde and glycolic acid are also found to be present as minor byproducts with hydroxyl functional group.

Figure 3.13(b) shows an increase of total concentration of the aldehyde functional groups in 30 min and then gradually decays. The compounds with aldehyde functional group contain end-aldehyde group in polymer chains, formaldehyde, glycolaldehyde, and glyoxalic acid. At the early degradation stage (i.e., 0-30 min of the reaction time), the aldehyde functional groups from the end-aldehyde group in polymer chain and formaldehyde are dominant. Then, the concentrations of these two aldehyde functional groups decrease, while the concentrations of the aldehyde functional groups from glycolaldehyde and glyoxalic acid gradually increase and finally become dominant.

Figure 3.13(c) shows a graduate increase of the total concentration of the carboxylic acid functional groups till 150 min and then declined. The carboxylic acid functional groups mostly arise from the end-carboxylic acid in the polymer chain. Formic acid and oxalic acid are other major sources for the carboxylic acid functional groups that appear at the early degradation stage (i.e., 0-80 min of the reaction time) and late degradation stage (i.e., 80-200 min of the reaction time), respectively. In addition, glycolic acid and glyoxylic acid are also minor compounds that contain carboxylic acid functional group.

Figure 3.13(d) shows a gradual increase of compounds with the ester functional group. All of the ester groups come from the inner-ester group in the polymer chain.

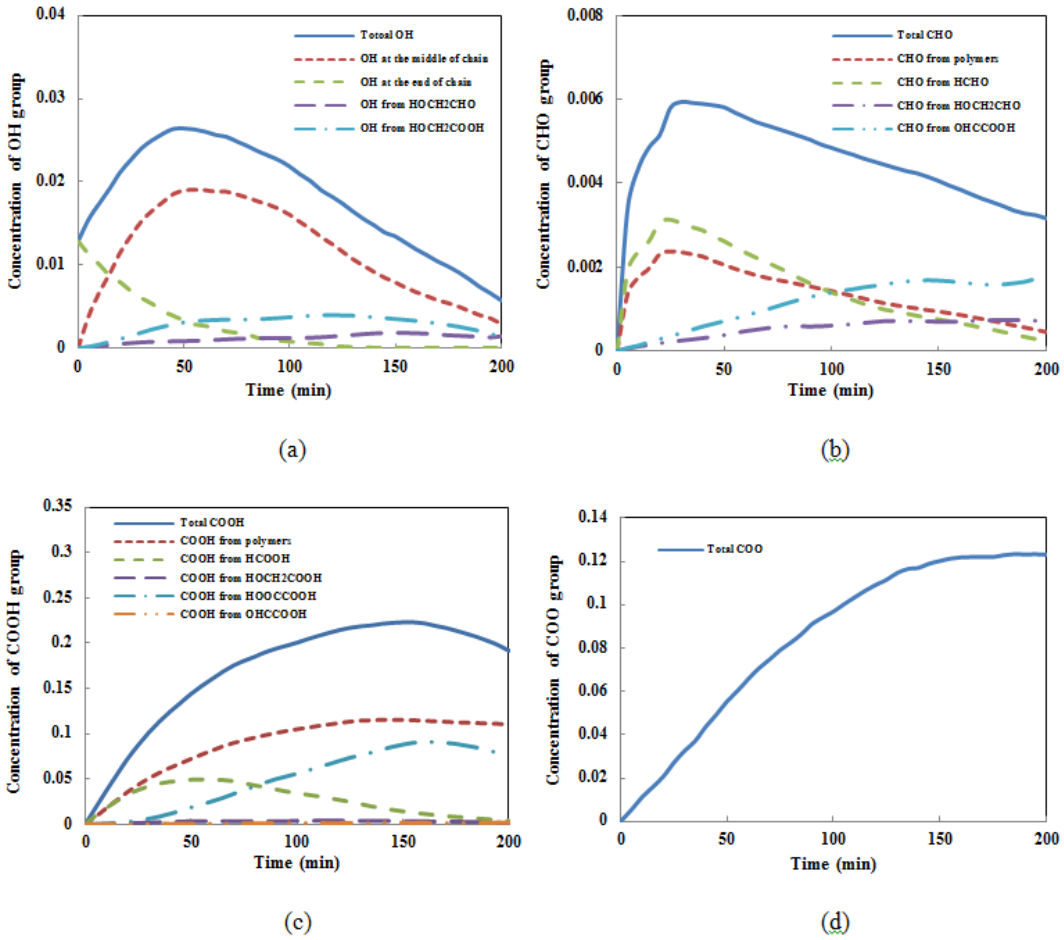

Figure 3.13. Calculated concentration profiles of (a) hydroxyl group, (b) aldehyde group, (c) carboxylic acid group, and (d) ester group for the degradation of PEG during the UV/H_2O_2 process. Concentrations are normalized by the initial carbon concentration of PEG (i.e., 28 mM)

3.4.7 Prediction of TOC

Although we do not have the experimental data about the total organic carbon (TOC), we can use our CF-KMC model to predict the change of TOC during the degradation of PEG in the UV/H_2O_2 process. Figure 3.14 shows that TOC decreases during the degradation of PEG, where TOC_0 is the initial TOC. The simulation conditions are the same as stated above.

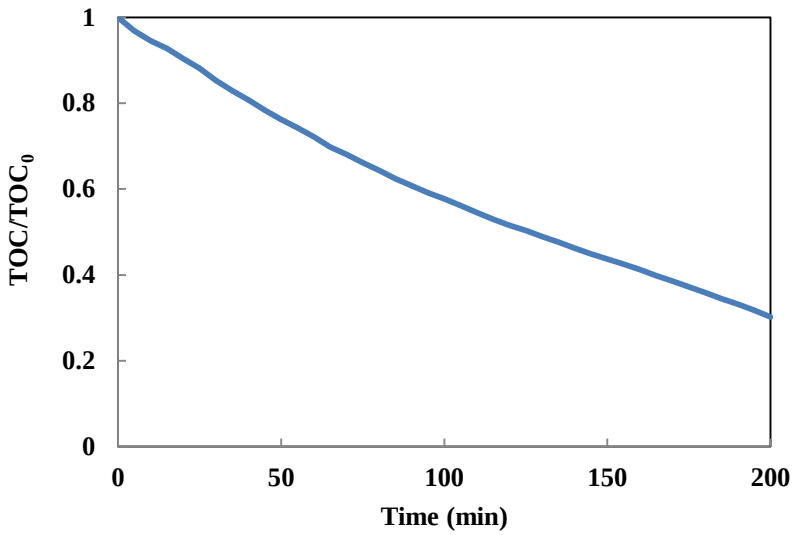

Figure 3.14. Prediction of TOC during the degradation of PEG in UV/H_2O_2 process.

3.5 Conclusion

Overall, this study has developed a CF-KMC model for the degradation of PEG in UV/H_2O_2 process. This CF-KMC model quantitatively provides detailed information about the degradation of PEG, including M_w and PDI profiles, time evolutions of MWD, LMWPs and functional groups. Since this model does not require solving ODEs, the difficulties such as stiffness can be avoided. This CF-KMC model can be extended to study the degradation of other large organic contaminants that may not be able to be solved by conventional ODEs-based models.

CHAPTER 4

ON-THE-FLY KINETIC MONTE CARLO SIMULATION OF POLYACRYLAMIDE DEGRADATION IN AQUEOUS PHASE UV/TIO_2 ADVANCED OXIDATION PROCESS

4.1 Abstraction

We have developed an on-the-fly kinetic Monte Carlo (KMC) model to predict degradation mechanisms and fates of intermediates and byproducts produced from the degradation of polyacrylamide (PAM) in the UV irradiation with photocatalyst titanium dioxide (UV/TiO_2) process. The on-the-fly KMC model is comprised of a reaction pathway generator, a reaction rate constant estimator, a KMC solver, and a mechanistic reduction module. The on-the-fly KMC model predicts and solves the degradation mechanisms simultaneously, which can simulate the degradation process with high computational efficiency and without solving ordinary differential equations. The predicted time-dependent profiles of averaged molecular weight for the PAM degradation was validated with experimental observations. The model also provided detailed and quantitative insights into the time evolutions of molecular weight distribution and size of the generated mechanism. Our approach may be useful to predict the fates of degradation products for a wide range of complicated organic contaminants.

4.2 Introduction

Advanced oxidation processes (AOPs) are attractive technologies to remove organic contaminants in water. During AOPs, highly reactive hydroxyl radicals are produced to react with organic compounds and further degrade these compounds by the

radical chain reactions. These radical chain reactions are mechanistically complex so that various kinds of intermediates and byproducts are produced. Some of these intermediates and byproducts may pose potential risks to human health (Rosenfeldt et al., 2004; Huber et al., 2003) and some of these intermediates and byproducts (i.e., volatile acids) may require longer detention time to remove. As a result, it is necessary for us to have a detailed and quantitative understanding about the degradation mechanisms and fates of intermediates and byproducts during AOPs.

Various studies have been conducted to investigate the degradation process of AOPs (Li et al., 2007; Stefan et al., 1996; Stefan et al., 1999; Stefan et al., 1998; Stefan et al., 2000; Cooper et al., 2009; Santos et al., 2009). However, these studies have the following limitations: first, the degradation mechanisms in these studies were determined by experiments, which is time consumed if the degradation mechanism is very complex or the number of parent compounds is very large; second, the kinetic models that were developed in these studies used lumped reactions for simplicity, which prevent us from obtaining a detailed insight into the degradation process; third, these kinetic models also require numerical solvers to solve ordinary differential equations (ODEs), which might be too stiff to be solved for complicated mechanism. For example, the degradation mechanism of PEG in UV/H_2O_2 process includes 522,057 species and 696,183 reactions, which might not be solved by most of the ODE solvers (Guo et al., 2014b).

To overcome these limitations, Guo *et al*. (Guo et al., 2014b) have developed the computer-based first-principles kinetic Monte Carlo (CF-KMC) model to simulate the degradation process of AOPs. Instead of conducting experiments, the CF-KMC model can automatically predict the degradation pathways in AOPs for a given parent

compound. These predicted degradation pathways are consisted of elementary reactions, which are in contrast to the lumped reactions that are used by traditional kinetic models. In addition, the CF-KMC model uses a KMC solver to solve the degradation mechanisms without solving ODEs. Hence, difficulties such as stiffness encountered by traditional ODE-based kinetic model will be avoided. The CF-KMC model successfully simulate the degradation of various parent compounds, including small contaminants (e.g., acetone and trichloroethylene) and large contaminants (e.g., polyethylene glycol), in aqueous phase AOPs. However, since the computational time for the CF-KMC model is proportional to the number of reactions that are included in the mechanism (Yang et al., 2011), the computational efficiency of the CF-KMC model to simulate extremely large degradation mechanism is still not sufficient.

One attractive method to increase the computational efficiency of the CF-KMC model is to develop an on-the-fly KMC model. This on-the-fly KMC model can predict and solve the degradation mechanism simultaneously, rather than the previous way of waiting until a full mechanism has been completed before calling the KMC solver to solving the mechanism. This on-the-fly strategy can significantly decrease the size of the mechanisms that are solved by the KMC solver, hence remarkably increase the computational efficiency. In addition, the on-the-fly KMC model also uses a mechanistic reduction module that can remove the unimportant reactions from the degradation mechanism, which can further increase the computational efficiency.

In this study, an on-the-fly KMC model is developed for the degradation of polyacrylamide (PAM) in the UV irradiation with photocatalyst titanium dioxide (UV/TiO_2) process. Detailed mechanisms for the degradation of PAM and fates of

intermediates and byproducts are generated and time-dependent profiles of number averaged molecular weight (M_n) and molecular weight distribution (MWD) are calculated. The simulation results are validated with experimental data.

4.3 Method

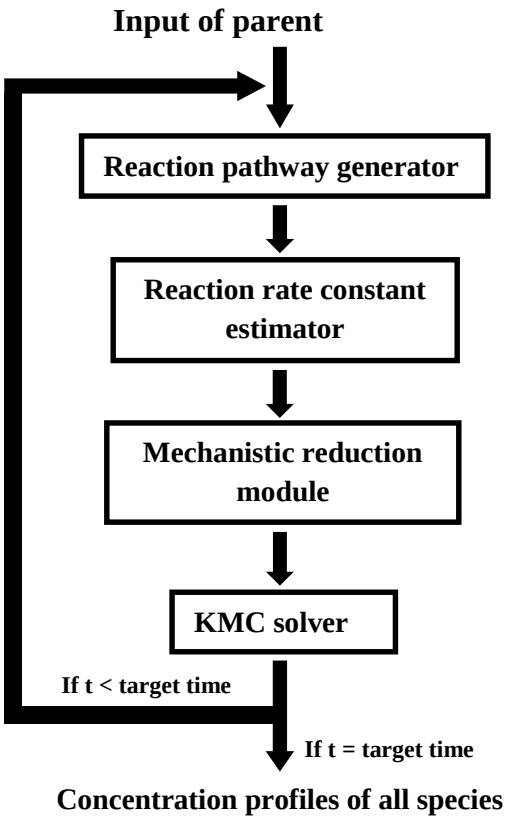

Figure 4.1. Overall structure of the on-the-fly KMC model.

Figure 4.1 shows the general structure of the on-the-fly KMC model. To begin with, the on-the-fly KMC model receives the information of a given parent compound that is provided by users and adds this parent compound into a species pool, which is the collection of all species that are existing in the system so far. At the same time, the on-the-fly KMC model also generates a reaction list to keep track of all reactions that are

generated so far. Then, the on-the-fly KMC model iteratively runs the following four modules at each time point. The first module is a pathway generator that can automatically generate elementary reactions included in the degradation pathways for the aqueous phase AOPs. At each time point, the pathway generator only predict the first generation products (i.e., products that can be directly produced from existing species by one elementary reaction step) of all species in the species pool. Then, the pathway generator adds all newly generated products into the species pool and all newly predicted reactions into the reaction list.

The second module can estimate reaction rate constant for each newly predicted reaction. Several robust tools, including Group Contribution Method (GCM) (Minakata et al., 2009) and Linear Free Energy Relationships (LFERs) (Minakata et al., 2011a; Minakata et al., 2011b; Minakata et al., 2014), have been developed to estimate reaction rate constants for various kinds of reactions for aqueous phase AOPs, including hydroxyl radical reaction, oxygen addition, disproportionation of peroxyl radicals, and unimolecular decay of peroxyl radicals. In this study, we used GCM to estimate hydroxyl radical reactions. For other reactions, the rate constants are either obtained from literature-reported values or estimated based on similar reactions in literature.

The third module is a mechanistic reduction algorithm that can eliminate unimportant reactions and species from the newly generated pathways and improve the computational efficiency of the on-the-fly KMC model. In this study, we used the Directed Relation Graph (DRG) method for the mechanistic reduction. The detailed description about DRG can be found in Lu *et al*. (Lu et al., 2005) and Guo *et al.* (Guo et al., 2014a)

The last module is a KMC solver that can solve the generated pathways without generating and solving ODEs. At each time point, the KMC solver selects one reaction to occur from the reaction list and update the concentrations of species that are involved in this selected reaction. Then, the KMC solver calculates the time interval for the next time point. The detailed description of the KMC solver can be found in Gillespie (Gillespie, 1971) and Guo *et al*. (Guo et al., 2014b)

The above four modules will be executed iteratively at each time point until the target time point is achieved. At the same time, the time-dependent concentrations of all species can also be calculated. Table 4.1 compares the computational efficiency of the on-the-fly KMC model with the traditional KMC model. From this table, we can see that for small parent compounds, the computational efficiency of both types of models are about the same, since the degradation mechanisms of small parent compounds are small and can be quickly fully generated, the on-the-fly strategy cannot significantly decrease the CPU time. For large parent compounds, we can see that the on-the-fly KMC model generally saves 60%-70% CPU time.

Table 4.1 Comparison of CPU time for on-the-fly KMC model and traditional KMC model. The processor used is 64-bit 2.4 GHz Intel® Core™ 2 Duo CPU

Parent Compound	CPU Time for on-the-fly KMC model	CPU Time for traditional KMC model
Acetone	18 sec	17 sec
TCE	13 sec	13 sec
PEG	12 min	30 min
PAM	20 min	65 min

4.4 Results and Discussions

4.4.1 Mechanism generation for the degradation of PAM

The degradation mechanism of PAM in UV/TiO_2 process was generated by the on-the-fly KMC model. The experimental conditions were described by Vijayalakshmi *et al.* (Vijayalakshmi et al., 2005) The initial concentration and number averaged molecular weight of PAM was 0.012 mM and 1.64 $\times 10^5$ g/mol, respectively. The wavelength of UV light was predominantly 365 nm and the light intensity was 1.19 $\times 10^{-5}$ Einstein/L·s. Commercial Degussa P-25 TiO_2 was used with a quantum yield of 0.04 (Sun et al., 1996). The reactor type was completely mixed batch reactor (CMBR).

The elementary reactions in the degradation mechanism of PAM were generated by the pathway generator as shown in Table D.1 in Appendix D. These elementary reactions cover most of reaction types that have been discovered to occur during aqueous phase AOPs, including hydroxyl radical H-atom abstraction, oxygen addition, β scission, and hydrolysis. The generated pathway also includes some overall reactions, such as bimolecular decays of peroxyl radical, due to lack of experimental studies that elucidate elementary steps. In addition, the current version of the pathway generator does not include the degradation of amide groups. As a result, this reaction was manually added into the generated pathway.

The reaction rate constants of the generated elementary reactions were primarily obtained by two methods: directly from literature and estimated by the GCM. The GCM can estimate hydroxyl radical reaction with an uncertainty within 0.5-2 times. The reaction rate constants that cannot be obtained by the above two methods were estimated based on similar reactions that have experimentally reported values. Table D.1 in

Appendix D contains the values of all reaction rate constants and how they were obtained or estimated.

The generated pathway was reduced by the DRG method with a criterion of 0.1%, which means the DRG method removed reactions that had rates smaller than 0.1% of overall consumption rate of reactant of interest. These removed reactions were majorly consisted of carbon radical H-atom abstraction reactions. The reduced mechanism was solved by the KMC solver with an initial population of 10^8. The detailed process about the way to select the appropriate criterion for the DRG method and initial population for the KMC solver can be found in authors' previous articles (Guo et al., 2014a; Guo et al., 2014b).

4.4.2 Predicted Reaction Pathways of PAM Degradation

4.4.2.1 Initial stage of the degradation of PAM

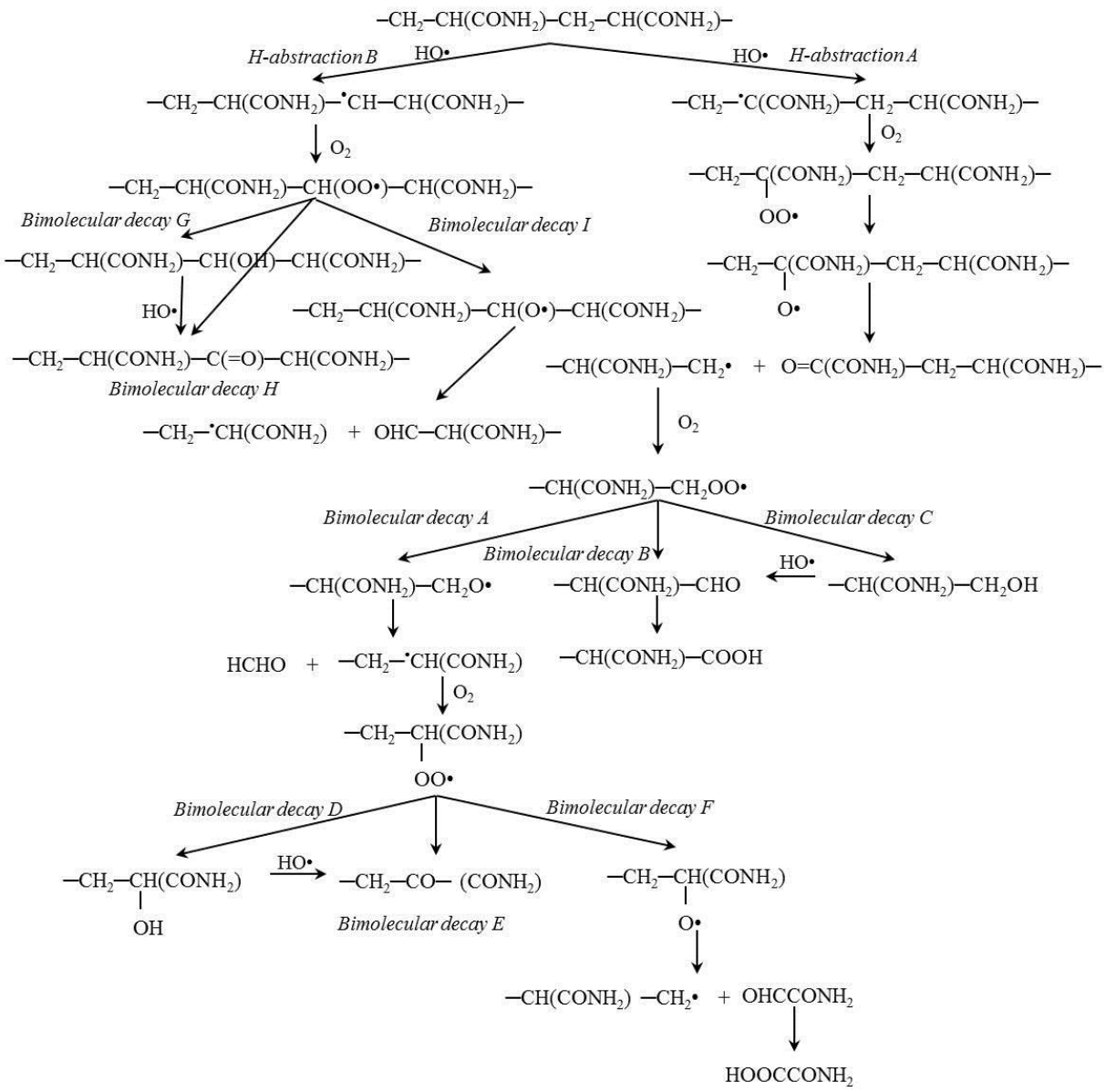

Figure 4.2. Generated degradation mechanism of PAM in the UV/TiO_2 process.

Figure 4.2 shows the generated degradation pathway of PAM in the UV/TiO_2 process. As the first step, the backbone of PAM molecule has two positions that can be attacked by hydroxyl radicals via H-atom abstraction reaction: the hydrogen atom attached to the α-carbon (i.e. H-abstraction A in Figure 4.2) and the hydrogen atom attached to the β-carbon (i.e. H-abstraction B in Figure 4.2). The ratio of the contributions of these two pathways is 1:3. These two pathways produce two different kinds of carbon-

centered radicals, which have radical sites located at α-carbon and β-carbon, respectively. In addition, the H-atom abstraction of hydrogen atom in the –CO-NH_2 group with hydroxyl radical is negligible as reported by Karpel Vel Leitner *et al.* (Karpel Vel Leitner et al., 2002).

4.4.2.2 Degradation of α-carbon centered radical

The α-carbon centered radical that is generated by the H-atom abstraction of PAM (i.e., H-abstraction A in Figure 4.2) produces oxyl radical, ─CH_2─C($CONH_2$)(O•)─CH_2─CH($CONH_2$)─, through the oxygen addition followed by the bimolecular decay. This oxyl radical goes the β-scission reaction and generates two sub-chains ended with O=C($CONH_2$)─ group and carbon-centered radical group, respectively (i.e., ─CH($CONH_2$)─CH_2• and O=C($CONH_2$)─CH_2─CH($CONH_2$)─ in Figure 4.2). On one side, O=C($CONH_2$)─CH_2─CH($CONH_2$)─ is attacked by hydroxyl radicals and is further degraded into LMWPs. On the other side, ─CH($CONH_2$)─CH_2• reaction rapidly with O_2 to form the end-peroxyl radical, ─CH($CONH_2$)─CH_2OO•.

The end-peroxyl radical, ─CH($CONH_2$)─CH_2OO•, is consumed through three bimolecular decay channels (i.e., bimolecular decay A, B, and C in Figure 4.2). First, ─CH($CONH_2$)─CH_2OO• goes through the Russell reaction (i.e., bimolecular decay C in Figure 4.2) (Russell, 1957) to produce end-hydroxyl group, which is further degraded to end-aldehyde group via the reaction with HO•. Second, ─CH($CONH_2$)─CH_2OO• also directly produces end-aldehyde group (i.e., bimolecular decay B in Figure 4.2), which is latterly hydrolyzed to end-carboxylic acid group. The end-carboxylic acid group undergoes randomly attack by HO• again, which finally leads to the formation of various

LMWPs. Third, ─CH($CONH_2$)─CH_2OO• produces end-oxyl radical, ─CH($CONH_2$)─CH_2O• (i.e., bimolecular decay A in Figure 4.2). The contributions of these three bimolecular decay channels are same.

The end-oxyl radical, ─CH($CONH_2$)─CH_2O•, decays through fast unimolecular fragmentation by C─O bond scission to form formaldehyde and end-carbon-centered radical, ─CH_2─•CH($CONH_2$), which is further degraded to end-peroxyl radical, ─CH_2─CH($CONH_2$)OO•. ─CH_2─CH($CONH_2$)OO• is consumed by three bimolecular decay channels (i.e., bimolecular decay D, E, and F in Figure 4.2) to produce end-hydroxyl group (─CH_2─CH($CONH_2$)(OH)), end-acyl group (─CH_2─CO─ ($CONH_2$)), and end-oxyl radical group (─CH_2─CH($CONH_2$)(O•)). On one side, ─CH_2─CH($CONH_2$)(OH) and ─CH_2─CO─ ($CONH_2$) are attacked by hydroxyl radicals and finally degraded to LMWPs. On the other side, ─CH_2─CH($CONH_2$)(O•) undergoes β-scission to generate $OHCCONH_2$ and ─CH($CONH_2$) ─CH_2•. The degradation pathway of ─CH($CONH_2$) ─CH_2• has been described above.

4.4.2.3 Degradation of β-carbon centered radical

The β-carbon centered radical, ─CH_2─CH($CONH_2$)─•CH─CH($CONH_2$)─, that is formed by H-atom abstraction of PAM (i.e., H-abstraction B in Figure 4.2) reacts with oxygen to produce peroxyl radical, ─CH_2─CH($CONH_2$)─CH(OO•)─CH($CONH_2$)─. This peroxyl radical undergoes three degradation channels, which forms three products: (1) inner-hydroxyl group, ─CH_2─CH($CONH_2$)─CH(OH)─CH($CONH_2$)─, (2) inner-ketone group, ─CH_2─CH($CONH_2$)─C(=O)─CH($CONH_2$)─, and (3) inner-oxyl radical,

─CH_2─CH($CONH_2$)─CH(O•)─CH($CONH_2$)─. The inner-hydroxyl group is further degraded to inner-ketone group, which is attacked by hydroxyl radicals again to finally form various LMWPs. The inner-oxyl radical undergoes β-scission to produce ─CH_2─•CH($CONH_2$) and OHC─CH($CONH_2$)─, whose degradation pathways have already been described above.

4.4.3 Simulation Results of PAM Degradation

Figure 4.3 compares the calculated profile of number averaged molecular weight (M_n) with experimental data reported by Vijayalakshmi *et al.* (Vijayalakshmi et al., 2005). The simulation results are in good agreement with the experimental data. From Figure 4.3, we can see that M_n decreases from 1.64 $\times 10^5$ g/mol to 5 $\times 10^4$ g/mol, which indicates the long chain PAM molecules are degraded into short chain oligomers during the UV/TiO_2 process.

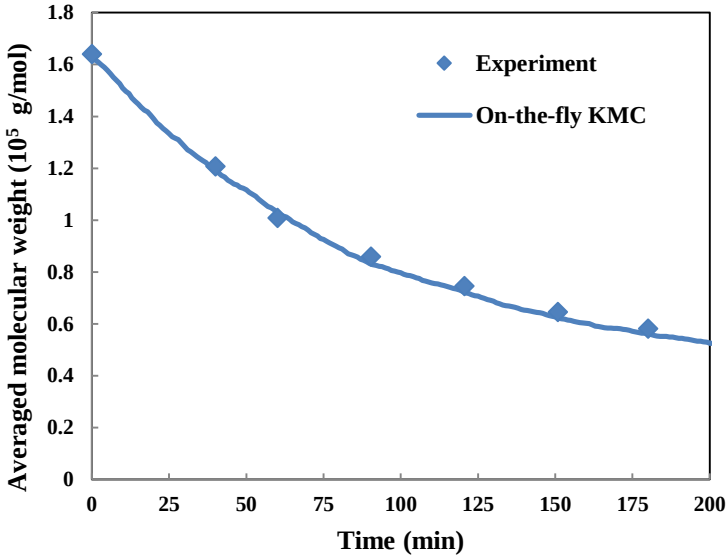

Figure 4.3. Comparison of profile of number averaged molecular weight between experimental data and calculated data for the degradation of PAM during UV/TiO_2 process.

To make a detailed look into the degradation process, we simulate the time evolvement of the molecular weight distribution (MWD) of the PAM degradation as shown in Figure 4.4. We can see that all polymers have the uniform and large molecular weight at the beginning (i.e., t = 0). As the degradation proceeds, the peak of the MWD shifts from large molecular weight to small molecular weight, which is consistent with the trend that is indicated by the M_n profile.

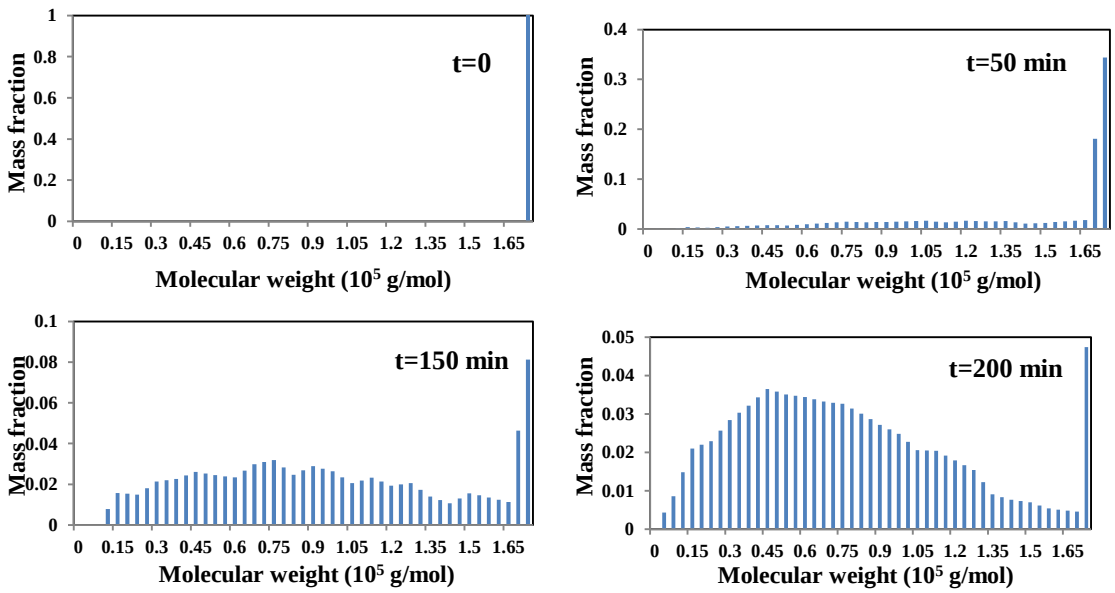

Figure 4.4. Calculated time evolution of molecular weight distribution for the degradation of PAM during the UV/TiO_2 process. Columns are the calculated mass tractions for polymers with various molecular weights.

Figure 4.5 shows the time evolvement of the number of generated reactions. At the initial stage (i.e., first 25 min), the number of reactions increases rapidly. Most of the reactions that is generated at this stage are H-atom abstraction reaction occurred on the backbone of PAM. At the second stage (i.e., 25 min to 100 min), the growth rate of the number of reactions slows down and the number of reactions finally converges to around 10^6. During this stage, the generated reactions are majorly consisted of oxygen addition

reaction, bimolecular decay reaction, β scission reaction and so forth. At the final stage (i.e., 100 min to 200 min), the number of reactions keep constant around 10^6, which indicates the degradation pathway is nearly completed.

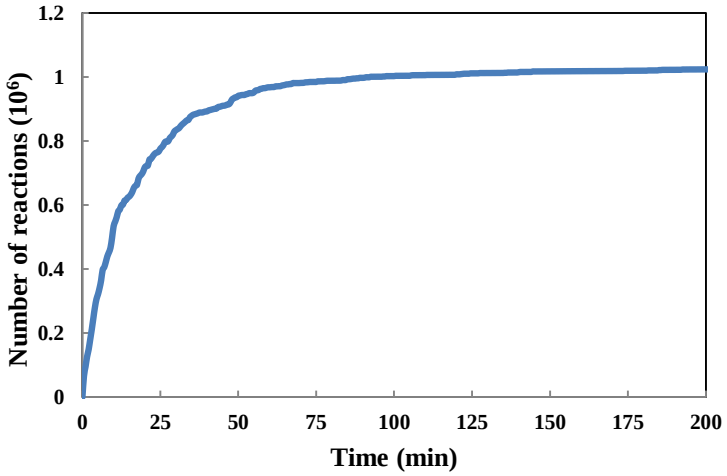

Figure 4.5. Time evolvement of the number of generated reactions for the degradation of PAM during the UV/TiO_2 process.

CHAPTER 5

FUTURE WORK

One potential error of the computer-based first-principles kinetic model may come from the uncertainty of the pathway generator. Although the current version of pathway generator can predict most of established elementary reactions occurring during AOPs, this pathway generator still cannot correctly predict some elementary reactions that are specific to certain compounds (e.g. reaction between hydrogen peroxide and pyruvic acid) or certain functional groups (e.g. S-, N-, or P-atom-containing groups). Furthermore, some elementary reactions should be further investigated (e.g. bimolecular decay of peroxyl radicals). More experimental and theoretical studies are needed to discover the elementary reaction mechanisms that have not been examined before and these are being investigated under ongoing work.

Another potential error of the computer-based first-principles kinetic model may come from the uncertainty of the reaction rate constant estimator. In this study, the reaction rate constant other than hydroxyl radical reaction are mostly estimated from similar reactions that have experimental values. This rough estimation might bring errors for the estimated reaction rate constants.

APPENDIX A

REACTIONS INCLUDED IN THE DEGRADATION MECHANISMS OF ACETONE AND TRICHLOROETHYLENE (TCE) IN UV/H_2O_2 PROCESS GENERATED BY THE COMPUTER-BASED KINETIC MODEL

Table A.1. Reactions included in the generated mechanism for the degradation of acetone in UV/H_2O_2 process with DRG criterion of 10^{-3}

	Reaction	Rate constant	References
1	$CH_3COCH_3 + \bullet OH \rightarrow \bullet CH_2COCH_3 + H_2O$	1.1×10^{8}	Buxton et al., 1988
2	$\bullet CH_2COCH_3 + O_2 \rightarrow \bullet OOCH_2COCH_3$	3×10^{9}	Zegota et al., 1986
3	$2\ \bullet OOCH_2COCH_3 \rightarrow 2\ \bullet OCH_2COCH_3 + O_2$	1×10^{8}	Schaefer et al., 2012
4	$2\ \bullet OOCH_2COCH_3 \rightarrow 2\ CH_3COCHO + H_2O_2$	2.13×10^{8}	Schaefer et al., 2012
5	$2\ \bullet OOCH_2COCH_3 \rightarrow CH_3COCHO + CH_3COCH_2OH + O_2$	4×10^{8}	Schaefer et al., 2012
6	$\bullet OCH_2COCH_3 \rightarrow \bullet CH(OH)COCH_3$	$1\times10^{6}\ s^{-1}$	Assumed based on Li et al., 2009
7	$\bullet OCH_2COCH_3 \rightarrow HCHO + \bullet COCH_3$	$1\times10^{6}\ s^{-1}$	Assumed based on Li et al., 2009
8	$CH_3COCHO + H_2O \xrightarrow{HO\bullet} CH_3COCOOH$	6.2×10^{8}	Schaefer et al., 2012
9	$CH_3COCH_2OH + \bullet OH \rightarrow \bullet CH_2COCH_2OH + H_2O$	5.43×10^{7}	GCM*
10	$CH_3COCH_2OH + \bullet OH \rightarrow CH_3COC^{\bullet}HOH + H_2O$	9.1×10^{7}	GCM*
11	$CH_3COC^{\bullet}HOH + O_2 \rightarrow \bullet OOCH(OH)COCH_3$	1×10^{9}	Neta et al., 1996
12	$HCOOH + \bullet OH \rightarrow CO_2^{-}\bullet + H^{+} + H_2O$	1.3×10^{8}	Buxton et al., 1988
13	$HCOO^{-} + \bullet OH \rightarrow CO_2^{-}\bullet + H_2O$	3.2×10^{9}	Buxton et al., 1988
14	$CO_2^{-}\bullet + O_2 \rightarrow O_2^{-}\bullet + CO_2$	2×10^{9}	Neta et al., 1990
15	$CO_2^{-}\bullet + H_2O_2 \rightarrow H_2O + CO_2 + \bullet OH$	6.3×10^{5}	Li et al., 2007
16	$HCHO + H_2O \xrightarrow{HO\bullet} HCOOH$	3.41×10^{8}	GCM*
17	$\bullet COCH_3 + O_2 \rightarrow \bullet OOCOCH_3$	1×10^{9}	Assumed based on Neta et al., 1996
18	$CH_3COCOOH + \bullet OH \rightarrow CH_3COC(O)O\bullet + H_2O$	7×10^{5}	GCM*
19	$CH_3COCOOH + \bullet OH \rightarrow \bullet CH_2COCOOH + H_2O$	5.43×10^{7}	GCM*
20	$CH_3COCOO^{-} + \bullet OH \rightarrow \bullet CH_2COCOO^{-} + H_2O$	5.43×10^{7}	GCM*
21	$\bullet CH_2COCH_2OH + O_2 \rightarrow \bullet OOCH_2COCH_2OH$	1×10^{9}	Assumed based on Neta et al., 1996

22	$\bullet OOCH(OH)COCH_3 \rightarrow CH_3COCHO + HO_2\bullet$	1×10^3 s^{-1}	Assumed based on Neta et al., 1990
23	$2\ \bullet OOCOCH_3 \rightarrow 2\ \bullet OCOCH_3 + O_2$	1×10^9	Assumed based on von Sonntag et al., 1991
24	$CH_3COC(O)O\bullet \rightarrow CO_2 + \bullet COCH_3$	1×10^6 s^{-1}	Assumed based on Li et al., 2009
25	$\bullet CH_2COCOOH + O_2 \rightarrow \bullet OOCH_2COCOOH$	1×10^9	Assumed based on Neta et al., 1996
26	$2\ \bullet OOCH_2COCH_2OH \rightarrow 2\ \bullet OCH_2COCH_2OH + O_2$	1×10^9	Assumed based on von Sonntag et al., 1991
27	$2\ \bullet OOCH_2COCH_2OH \rightarrow 2\ CH_2(OH)COCHO + H_2O_2$	1×10^9	Assumed based on von Sonntag et al., 1991
28	$2\ \bullet OOCH_2COCH_2OH \rightarrow CH_2(OH)COCHO + CH_2(OH)COCH_2OH + O_2$	1×10^9	Assumed based on von Sonntag et al., 1991
29	$2\ \bullet OOCH_2COCOOH \rightarrow 2\ \bullet OCH_2COCOOH + O_2$	1×10^9	Assumed based on von Sonntag et al., 1991
30	$2\ \bullet OOCH_2COCOOH \rightarrow 2\ OHCCOCOOH + H_2O_2$	1×10^9	Assumed based on von Sonntag et al., 1991
31	$2\ \bullet OOCH_2COCOOH \rightarrow OHCCOCOOH + HOCH_2COCOOH + O_2$	1×10^9	Assumed based on von Sonntag et al., 1991
32	$\bullet OCH_2COCH_2OH \rightarrow \bullet CH(OH)COCH_2OH$	1×10^6 s^{-1}	Assumed based on Li et al., 2009
33	$\bullet OCH_2COCH_2OH \rightarrow HCHO + \bullet COCH_2OH$	1×10^6 s^{-1}	Assumed based on Li et al., 2009
34	$CH_2(OH)COCHO + H_2O \xrightarrow{HO\bullet} CH_2(OH)COCOOH$	1.02×10^8	GCM*
35	$CH_2(OH)COCH_2OH + \bullet OH \rightarrow \bullet CH(OH)COCH_2OH + H_2O$	9.1×10^7	GCM*
36	$\bullet OCH_2COCOOH \rightarrow \bullet CH(OH)COCOOH$	1×10^6 s^{-1}	Assumed based on Li et al., 2009
37	$\bullet OCH_2COCOOH \rightarrow HCHO + \bullet COCOOH$	1×10^6 s^{-1}	Assumed based on Li et al., 2009
38	$OHCCOCOOH + H_2O \xrightarrow{HO\bullet} HOOCCOCOOH$	1.02×10^8	GCM*
39	$CH_2(OH)COCOOH + \bullet OH \rightarrow \bullet CH(OH)COCOOH + H_2O$	9.1×10^7	GCM*
40	$CH_2(OH)COCOOH + \bullet OH \rightarrow CH_2(OH)COC(O)O\bullet + H_2O$	7×10^5	GCM*
41	$\bullet CH(OH)COCH_2OH + O_2 \rightarrow \bullet OOCH(OH)COCH_2OH$	1×10^9	Assumed based on Neta et al., 1996
42	$\bullet COCH_2OH + O_2 \rightarrow \bullet OOCOCH_2OH$	1×10^9	Assumed based on Neta et al., 1996
43	$\bullet CH(OH)COCOOH + O_2 \rightarrow \bullet OOCH(OH)COCOOH$	1×10^9	Assumed based on Neta et al., 1996
44	$\bullet COCOOH + O_2 \rightarrow \bullet OOCOCOOH$	1×10^9	Assumed based on Neta et al., 1996
45	$\bullet OCH_2COOH \rightarrow \bullet CH_2(OH)COOH$	1×10^6	Assumed based on Li et al., 2009
46	$CH_2(OH)COC(O)O\bullet \rightarrow CO_2 + \bullet COCH_2(OH)$	1×10^6 s^{-1}	Assumed based on Li et al., 2009

47	$\bullet OOCH(OH)COCH_2OH \rightarrow OHCCOCH_2OH + HO_2\bullet$	1×10^3 s^{-1}	Assumed based on Li et al., 2009
48	$2\ \bullet OOCOCH_2OH \rightarrow 2\ \bullet OCOCH_2OH + O_2$	1×10^5	Assumed based on von Sonntag et al., 1991
49	$\bullet OOCH(OH)COCOOH \rightarrow OHCCOCOOH + HO_2\bullet$	1×10^3 s^{-1}	Assumed based on Li et al., 2009
50	$2\ \bullet OOCOCOOH \rightarrow 2\ \bullet OCOCOOH + O_2$	1×10^5	Assumed based on von Sonntag et al., 1991
51	$OHCCH_3 + H_2O \xrightarrow{HO\bullet} CH_3COOH$	7.45×10^8	*GCM
52	$\bullet OCOCH_2OH \rightarrow CO_2 + \bullet CH_2OH$	1×10^6 s^{-1}	Assumed based on Li et al., 2009
53	$\bullet OCOCOOH \rightarrow CO_2 + \bullet COOH$	1×10^6 s^{-1}	Assumed based on Li et al., 2009
54	$CH_3COOH + \bullet OH \rightarrow CH_3C(O)O\bullet + H_2O$	7×10^5	*GCM
55	$CH_3COOH + \bullet OH \rightarrow \bullet CH_2COOH + H_2O$	1.6×10^7	(6)
56	$CH_3COO^- + \bullet OH \rightarrow \bullet CH_2COO^- / \bullet CH_2COOH + H_2O$	8.5×10^7	(6)
57	$\bullet CH_2(OH) + O_2 \rightarrow \bullet OOCH_2(OH)$	1×10^9	Assumed based on Neta et al., 1996
58	$\bullet COOH + O_2 \rightarrow \bullet OOCOOH$	1×10^9	Assumed based on Neta et al., 1996
59	$\bullet CH_2COOH + O_2 \rightarrow \bullet OOCH_2COOH$	1×10^9	Assumed based on Neta et al., 1996
60	$\bullet OOCH_2(OH) \rightarrow HCHO + HO_2\bullet$	1×10^3 s^{-1}	Assumed based on Li et al., 2009
61	$\bullet OOCOOH \rightarrow CO_2 + HO_2\bullet$	1×10^1 s^{-1}	Assumed based on Neta et al., 1990
62	$2\ \bullet OOCH_2COOH \rightarrow 2\ \bullet OCH_2COOH + O_2$	1×10^9	Assumed based on von Sonntag et al., 1991
63	$2\ \bullet OOCH_2COOH \rightarrow 2\ OHCCOOH + H_2O_2$	1×10^9	Assumed based on von Sonntag et al., 1991
64	$2\ \bullet OOCH_2COOH \rightarrow OHCCOOH + CH_2(OH)COOH + O_2$	1×10^9	Assumed based on von Sonntag et al., 1991
65	$\bullet OCH_2COOH \rightarrow HCHO + \bullet COOH$	1×10^6 s^{-1}	Assumed based on Li et al., 2009
66	$HOOCCOOH + \bullet OH \rightarrow CO_2 + CO_2^-\bullet + H^+ + H_2O$	1.4×10^6	Buxton et al., 1988
67	$HOOCCOO^- + \bullet OH \rightarrow CO_2 + CO_2^-\bullet + H_2O$	4.7×10^7	Buxton et al., 1988
68	$H^+ + {}^-OOCCOO^- + \bullet OH \rightarrow CO_2 + CO_2^-\bullet + H_2O$	7.7×10^6	Buxton et al., 1988
69	$OHCCOOH + H_2O \xrightarrow{HO\bullet} HOOCCOOH$	2.86×10^7	*GCM
70	$CH_2(OH)COOH + \bullet OH \rightarrow \bullet CH(OH)COOH + H_2O$	5.4×10^8	*GCM
71	$CH_2(OH)COOH + \bullet OH \rightarrow CH_2(OH)C(O)O\bullet + H_2O$	7×10^5	*GCM
72	$CH_2(OH)COOH + \bullet OH \rightarrow \bullet OCH_2COOH + H_2O$	7×10^5	*GCM
73	$\bullet CH(OH)COOH + O_2 \rightarrow \bullet OOCH(OH)COOH$	1×10^9	Assumed based on Neta et al., 1996

74	$\bullet OOCH(OH)COOH \rightarrow OHCCOOH + HO_2\bullet$	1×10^3 s^{-1}	Assumed based on Neta et al., 1990
75	$CH_3COCOOH + H_2O_2 \rightarrow CH_3COOH + CO_2$	0.11	Stefan et al., 1999
76	$CH_3COCH_2OH + \bullet OH \rightarrow \bullet OCH_2COCH_3 + H_2O$	7×10^5	*GCM
77	$CH_2(OH)COCH_2OH + \bullet OH \rightarrow \bullet OCH_2COCH_2OH + H_2O$	7×10^5	*GCM
78	$CH_2(OH)COCOOH + \bullet OH \rightarrow \bullet OCH_2COCOOH + H_2O$	7×10^5	*GCM
79	$HOOCCOCOOH + \bullet OH \rightarrow \bullet OOCCOCOOH + H_2O$	7×10^5	*GCM
80	$\bullet OOCCOCOOH \rightarrow CO_2 + \bullet COCOOH$	1×10^6 s^{-1}	Assumed based on Li et al., 2009
81	$H_2O_2 + h\nu \rightarrow 2\ \bullet OH$	$\Phi_{H2O2} = 0.5$	Hunt et al., 1952
82	$H_2O_2 + HO\bullet \rightarrow H_2O + HO_2\bullet$	2.7×10^7	Buxton et al., 1988
83	$HO_2^- + HO\bullet \rightarrow OH^- + HO_2\bullet$	7.5×10^9	Buxton et al., 1988
84	$H_2O_2 + HO_2\bullet \rightarrow \bullet OH + H_2O + O_2$	3	Buxton et al., 1988
85	$H_2O_2 + O_2^-\bullet \rightarrow \bullet OH + OH^- + O_2$	0.13	Buxton et al., 1988
86	$\bullet OH + CO_3^{2-} \rightarrow CO_3^-\bullet + OH^-$	3.9×10^8	Buxton et al., 1988
87	$\bullet OH + HCO_3^- \rightarrow CO_3^-\bullet + H_2O$	8.5×10^6	Buxton et al., 1988
88	$H_2O_2 + CO_3^-\bullet \rightarrow HCO_3^- + HO_2\bullet$	4.3×10^5	Neta et al., 1988
89	$HO_2^- + CO_3^-\bullet \rightarrow CO_3^{2-} + HO_2\bullet$	3×10^7	Neta et al., 1988
90	$2\ HO\bullet \rightarrow H_2O_2$	5.5×10^9	Buxton et al., 1988
91	$HO\bullet + HO_2\bullet \rightarrow H_2O + O_2$	6.6×10^9	Elliott et al., 1992
92	$2\ HO_2\bullet \rightarrow H_2O_2 + O_2$	8.3×10^5	Bielski et al., 1985
93	$O_2^-\bullet + HO_2\bullet \rightarrow HO_2^- + O_2$	9.7×10^7	Bielski et al., 1985
94	$HO\bullet + O_2^-\bullet \rightarrow OH^- + O_2$	7×10^9	Elliott et al., 1992
95	$HO\bullet + CO_3^-\bullet \rightarrow$ unknown	3×10^9	Holeman et al., 1986
96	$O_2^-\bullet + CO_3^-\bullet \rightarrow CO_3^{2-} + O_2$	6×10^8	Eriksen et al., 1977
97	$H_2O_2 \Leftrightarrow H^+ + HO_2^-$	$pK_a = 11.6$	Perry et al., 1981
98	$HCOOH \Leftrightarrow H^+ + HCOO^-$	$pK_a = 3.75$	Lide et al., 2005
99	$CH_3COOH \Leftrightarrow H^+ + CH_3COO^-$	$pK_a = 4.75$	Lide et al., 2005
100	$HOOCCOOH \Leftrightarrow H^+ + HOOCCOO^-$	$pK_a = 1.25$	Lide et al., 2005
101	$HOOCCOO^- \Leftrightarrow H^+ + {}^-OOCCOO^-$	$pK_a = 3.81$	Lide et al., 2005
102	$H_2CO_3 \Leftrightarrow H^+ + HCO_3^-$	$pK_a = 6.3$	Lide et al., 2005
103	$HO_2\bullet \Leftrightarrow H^+ + O_2^-\bullet$	$pK_a = 4.8$	Bielski et al., 1985

*GCM: the reaction rate constant is predicted by the Group Contribution Method (GCM) developed by Minakata *et al* (Minakata et al., 2009).

Table A.2. Reactions included in the generated mechanism for the degradation of TCE in UV/H_2O_2 process with DRG criterion of 10^{-2}

	Reaction	Rate constant ($M^{-1}s^{-1}$)	References
1	$ClHC{=}CCl_2 + {}^{\bullet}OH \rightarrow ClCH(OH)\text{-}C^{\bullet}Cl_2$	2.4×10^{9}	Farhartaziz et al., 1977
2	$ClCH(OH)\text{-}C^{\bullet}Cl_2 \rightarrow OHC\text{-}C^{\bullet}Cl_2 + HCl$	5.1×10^{5} s^{-1}	Mertens et al., 1995
3	$OHC\text{-}C^{\bullet}Cl_2 + O_2 \rightarrow OHC\text{-}C(Cl_2)OO^{\bullet}$	3×10^{9}	von Sonntag et al., 1997
4	$2\ OHC\text{-}C(Cl_2)OO^{\bullet} \rightarrow 2\ OHC\text{-}C(Cl_2)O^{\bullet} + O_2$	4×10^{8}	von Sonntag et al., 1997
5	$OHC\text{-}C(Cl_2)O^{\bullet} \rightarrow OHC\text{-}C(O)Cl + Cl^{\bullet}$	1×10^{5} s^{-1}	von Sonntag et al., 1997
6	$COCl_2 + H_2O \rightarrow CO_2 + 2\ HCl$	8 s^{-1}	Li et al., 2007
7	$OHC\text{-}C(Cl_2)O^{\bullet} \rightarrow COCl_2 + {}^{\bullet}CHO$	1×10^{6} s^{-1}	Li et al., 2007
8	$OHCCOOH + H_2O_2 \rightarrow HCOOH + CO_2 + H_2O$	0.3	Leitzke et al., 2001
9	$HCOOH + {}^{\bullet}OH \rightarrow CO_2^{\bullet-} + H_2O + H^{+}$	1.3×10^{8}	Buxton et al., 1988
10	$HCOO^{-} + {}^{\bullet}OH \rightarrow CO_2^{\bullet-} + H_2O$	3.2×10^{9}	Buxton et al., 1988
11	$CO_2^{\bullet-} + O_2 \rightarrow CO_2 + O_2^{\bullet-}$	2×10^{9}	Neta et al., 1990
12	$CO_2^{\bullet-} + H_2O_2 \rightarrow CO_2 + OH^{-} + {}^{\bullet}OH$	6.3×10^{5}	Schwarz, 1992
13	$OHC\text{-}C(O)Cl + H_2O \rightarrow OHCCOOH + HCl$	0.005 s^{-1}	Li et al., 2007
14	$ClHC{=}CCl_2 + {}^{\bullet}Cl \rightarrow Cl_2CH\text{-}C^{\bullet}Cl_2$	1.9×10^{8}	Li et al., 2007
15	${}^{\bullet}CHO + H_2O + O_2 \rightarrow HCOOH + O_2^{-}\bullet + H^{+}$	1×10^{6} s^{-1}	Neta et al., 1996
16	$HOOCCOOH + {}^{\bullet}OH \rightarrow CO_2 + CO_2^{\bullet-} + H_2O + H^{+}$	1.4×10^{6}	Buxton et al., 1988
17	$HOOCCOO^{-} + {}^{\bullet}OH \rightarrow CO_2 + CO_2^{\bullet-} + H_2O$	4.7×10^{7}	Buxton et al., 1988
18	$H^{+} + OOCCOO^{-} + {}^{\bullet}OH \rightarrow CO_2 + CO_2^{\bullet-} + H_2O$	7.7×10^{6}	Buxton et al., 1988
19	$OHCCOOH + H_2O \xrightarrow{HO\bullet} HOOCCOOH$	2.86×10^{7}	*GCM
20	$Cl_2CH\text{-}C^{\bullet}Cl_2 + O_2 \rightarrow Cl_2CH\text{-}C(Cl_2)OO^{\bullet}$	1×10^{8}	Assumed based on Neta et al., 1996
22	$2\ Cl_2CH\text{-}C(Cl_2)OO^{\bullet} \rightarrow 2\ Cl_2CH\text{-}C(Cl_2)O^{\bullet} + O_2$	1×10^{9}	Assumed based on Von Sonntag et al., 1991
24	$Cl_2CHCOOH + {}^{\bullet}OH \rightarrow Cl_2C^{\bullet}COOH + H_2O$	2.75×10^{7}	Mao et al., 1991
25	$Cl_2CHCOO^{-} + {}^{\bullet}OH \rightarrow Cl_2C^{\bullet}COO^{-} + H_2O$	9.2×10^{7}	Maruthamuthu et al., 1995
26	$Cl_2CH\text{-}C(Cl_2)O^{\bullet} \rightarrow COCl_2 + {}^{\bullet}CHCl_2$	1×10^{6} s^{-1}	Li et al., 2007
27	$Cl_2CH\text{-}C(Cl_2)O^{\bullet} \rightarrow Cl_2CH\text{-}C(O)Cl + Cl^{\bullet}$	1×10^{5} s^{-1}	Li et al., 2007
28	$Cl_2C^{\bullet}COOH + O_2 \rightarrow {}^{\bullet}OOCCl_2\text{-}COOH$	1×10^{9}	Assumed based on Neta et al., 1996
29	$Cl_2CHC(O)O^{\bullet} \rightarrow CO_2 + {}^{\bullet}CHCl_2$	1×10^{6} s^{-1}	Assumed based on Li et al., 2009
30	${}^{\bullet}CHCl_2 + O_2 \rightarrow {}^{\bullet}OOCHCl_2$	1×10^{9}	Assumed based on Neta et al., 1996
31	$Cl_2CH\text{-}C(O)Cl + H_2O \rightarrow Cl_2CHCOOH + HCl$	0.005 s^{-1}	Li et al., 2007

32	$2\ ^{\bullet}OOCCl_2\text{-}COOH \rightarrow 2\ ^{\bullet}OCCl_2\text{-}COOH + O_2$	1×10^{9}	Assumed based on von Sonntag et al., 1991
33	$2\ ^{\bullet}OOCHCl_2 \rightarrow 2\ ^{\bullet}OCHCl_2 + O_2$	1×10^{9}	Assumed based on von Sonntag et al., 1991
34	$2\ ^{\bullet}OOCHCl_2 \rightarrow 2\ COCl_2 + H_2O_2$	1×10^{9}	Assumed based on von Sonntag et al., 1991
35	$2\ ^{\bullet}OOCHCl_2 \rightarrow COCl_2 + HOCHCl_2 + O_2$	1×10^{9}	Assumed based on von Sonntag et al., 1991
36	$^{\bullet}OCCl_2\text{-}COOH \rightarrow COCl_2 + {}^{\bullet}COOH$	$1\times10^{6}\ s^{-1}$	Assumed based on Li et al., 2009
37	$^{\bullet}OCCl_2\text{-}COOH \rightarrow OClC\text{-}COOH + Cl^{\bullet}$	$1\times10^{5}\ s^{-1}$	Assumed based on Li et al., 2009
38	$^{\bullet}OCHCl_2 \rightarrow HCOCl + Cl^{\bullet}$	$1\times10^{5}\ s^{-1}$	Assumed based on Li et al., 2009
39	$^{\bullet}OCHCl_2 \rightarrow {}^{\bullet}CCl_2(OH)$	$1\times10^{6}\ s^{-1}$	Assumed based on Li et al., 2009
40	$HCOCl \rightarrow HCl + CO$	$1\times10^{4}\ s^{-1}$	Li et al., 2009
41	$HOCHCl_2 \rightarrow HCOCl + HCl$	$5\times10^{5}\ s^{-1}$	Assumed based on Li et al., 2007
42	$^{\bullet}COOH + O_2 \rightarrow {}^{\bullet}OOCOOH$	1×10^{9}	Assumed based on Neta et al., 1996
43	$OClC\text{-}COOH + H_2O \rightarrow HOOCCOOH + HCl$	$0.005\ s^{-1}$	Li et al., 2007
44	$^{\bullet}CCl_2(OH) + O_2 \rightarrow {}^{\bullet}OOCCl_2(OH)$	1×10^{9}	Assumed based on Neta et al., 1996
45	$^{\bullet}OOCOOH \rightarrow CO_2 + HO_2^{\bullet}$	$1\times10^{6}\ s^{-1}$	Assumed based on Neta et al., 1990
46	$^{\bullet}OOCCl_2(OH) \rightarrow COCl_2 + HO_2^{\bullet}$	$1\times10^{6}\ s^{-1}$	Assumed based on Neta et al., 1990
47	$ClHC{=}CCl_2 + h\nu \rightarrow ClHC{=}C^{\bullet}Cl + Cl^{\bullet}$	$\Phi = 0.13$	Li et al., 2004
48	$ClHC{=}CCl_2 + H_2O + h\nu \rightarrow ClHC(OH)\text{-}CHCl_2$	$\Phi = 0.1$	Li et al., 2004
49	$ClHC{=}CCl_2 + h\nu \rightarrow ClC \equiv CCl + HCl$	$\Phi = 0.092$	Li et al., 2004
50	$ClHC{=}C^{\bullet}Cl + O_2 \rightarrow ClHC{=}C(Cl)OO^{\bullet}$	1×10^{9}	Assumed based on Neta et al., 1996
51	$2\ ClHC{=}C(Cl)OO^{\bullet} \rightarrow 2\ ClHC{=}C(Cl)O^{\bullet} + O_2$	1×10^{9}	Assumed based on von Sonntag et al., 1991
52	$ClHC{=}C(Cl)O^{\bullet} + H_2O \rightarrow ClCH_2COOH + Cl^{\bullet}$	$0.005\ s^{-1}$	Assumed based on Li et al., 2009
53	$ClCH_2COOH + {}^{\bullet}OH \rightarrow ClC^{\bullet}HCOOH + H_2O$	4.3×10^{7}	Farhartaziz et al., 1977
54	$ClCH_2COO^{-} + {}^{\bullet}OH \rightarrow ClC^{\bullet}HCOO^{-} + H_2O$	4×10^{8}	Maruthamuthu et al., 1995
55	$ClC^{\bullet}HCOOH + O_2 \rightarrow {}^{\bullet}OOCClH\text{-}COOH$	1×10^{9}	Assumed based on Neta et al., 1996
56	$2\ ^{\bullet}OOCClH\text{-}COOH \rightarrow 2\ ^{\bullet}OCClH\text{-}COOH + O_2$	1×10^{9}	Assumed based on von Sonntag et al., 1991
57	$2\ ^{\bullet}OOCClH\text{-}COOH \rightarrow 2\ OClC\text{-}COOH + H_2O_2$	1×10^{9}	Assumed based on von Sonntag et al., 1991

58	$2\ ^{\bullet}OOCClH\text{-}COOH \rightarrow OClC\text{-}COOH + ClHC(OH)\text{-}COOH + O_2$	1×10^{9}	Assumed based on von Sonntag et al., 1991
59	$^{\bullet}OCClH\text{-}COOH \rightarrow {}^{\bullet}CCl(OH)\text{-}COOH$	$1\times10^{6}\ s^{-1}$	Assumed based on Li et al., 2009
60	$^{\bullet}OCClH\text{-}COOH \rightarrow HCOCl + {}^{\bullet}COOH$	$1\times10^{6}\ s^{-1}$	Assumed based on Li et al., 2009
61	$^{\bullet}OCClH\text{-}COOH \rightarrow OHCCOOH + Cl^{\bullet}$	$1\times10^{5}\ s^{-1}$	Assumed based on Li et al., 2009
62	$ClHC(OH)\text{-}COOH \rightarrow OHCCOOH + HCl$	$5\times10^{5}\ s^{-1}$	Assumed based on Li et al., 2007
63	$^{\bullet}CCl(OH)\text{-}COOH + O_2 \rightarrow {}^{\bullet}OOCCl(OH)\text{-}COOH$	1×10^{5}	Assumed based on Neta et al., 1996
64	$^{\bullet}OOCCl(OH)\text{-}COOH \rightarrow OClCCOOH + HO_2^{\bullet}$	$1\times10^{3}\ s^{-1}$	Assumed based on Neta et al., 1990
65	$ClHC(OH)\text{-}CHCl_2 \rightarrow OHC\text{-}CHCl_2 + HCl$	$5\times10^{5}\ s^{-1}$	Assumed based on Li et al., 2007
66	$OHC\text{-}CHCl_2 + H_2O \xrightarrow{HO^{\bullet}} Cl_2CHCOOH$	7.81×10^{8}	*GCM
67	$ClC\equiv CCl + {}^{\bullet}OH \rightarrow Cl(OH)C{=}C^{\bullet}Cl$	3×10^{9}	Li et al., 2007
68	$Cl(OH)C{=}C^{\bullet}Cl \rightarrow O{=}C{=}C^{\bullet}Cl + HCl$	$1\times10^{6}\ s^{-1}$	Assumed based on Li et al., 2007
69	$O{=}C{=}C^{\bullet}Cl + H_2O \rightarrow HC^{\bullet}ClCOOH$	$0.005\ s^{-1}$	Assumed based on Li et al., 2009
70	$H_2O_2 + h\nu \rightarrow 2\ {}^{\bullet}OH$	$\Phi_{H2O2} = 0.5$	Hunt et al., 1952
71	$H_2O_2 + {}^{\bullet}OH \rightarrow H_2O + HO_2^{\bullet}$	2.7×10^{7}	Buxton et al., 1988
72	$HO_2^{-} + {}^{\bullet}OH \rightarrow OH^{-} + HO_2^{\bullet}$	7.5×10^{9}	Buxton et al., 1988
73	$H_2O_2 + HO_2^{\bullet} \rightarrow {}^{\bullet}OH + H_2O + O_2$	3	Buxton et al., 1988
74	$H_2O_2 + O_2^{\bullet-} \rightarrow {}^{\bullet}OH + OH^{-} + O_2$	0.13	Buxton et al., 1988
75	$2\ {}^{\bullet}OH \rightarrow H_2O_2$	5.5×10^{9}	Buxton et al., 1988
76	$^{\bullet}OH + HO_2^{\bullet} \rightarrow H_2O + O_2$	6.6×10^{9}	Elliott et al., 1992
77	$2\ HO_2^{\bullet} \rightarrow H_2O_2 + O_2$	8.3×10^{5}	Bielski et al., 1985
78	$O_2^{\bullet-} + HO_2^{\bullet} \rightarrow HO_2^{-} + O_2$	9.7×10^{7}	Bielski et al., 1985
79	$^{\bullet}OH + O_2^{\bullet-} \rightarrow OH^{-} + O_2$	7×10^{9}	Elliott et al., 1992
80	$Cl^{\bullet} + H_2O_2 \rightarrow HO_2^{\bullet} + Cl^{-}$	3×10^{9}	Li et al., 2007
81	$Cl^{\bullet} + Cl^{-} \rightarrow Cl_2^{\bullet-}$	8.6×10^{9}	Yu et al., 2004
82	$Cl_2^{\bullet-} + H_2O_2 \rightarrow HO_2^{\bullet} + 2\ Cl^{-} + H^{+}$	1.4×10^{5}	Neta et al., 1988
83	$H_2O_2 \Leftrightarrow H^{+} + HO_2^{-}$	$pK_a = 11.6$	Perry et al., 1981
84	$HCOOH \Leftrightarrow H^{+} + HCOO^{-}$	$pK_a = 3.75$	Lide et al., 2005
85	$CHCl_2COOH \Leftrightarrow H^{+} + CHCl_2COO^{-}$	$pK_a = 1.35$	Lide et al., 2005
86	$CH_2ClCOOH \Leftrightarrow H^{+} + CH_2ClCOO^{-}$	$pK_a = 2.87$	Lide et al., 2005
87	$HOOCCOOH \Leftrightarrow H^{+} + HOOCCOO^{-}$	$pK_a = 1.25$	Lide et al., 2005

88	$HOOCCOO^- \Leftrightarrow H^+ + {}^-OOCCOO^-$	$pK_a = 3.81$	Lide et al., 2005
89	$HO_2\bullet \Leftrightarrow H^+ + O_2^-\bullet$	$pK_a = 4.8$	Bielski et al., 1985

*GCM: the reaction rate constant is predicted by the Group Contribution Method (GCM) developed by Minakata *et al* (Minakata et al., 2009).

Table A.3. Top 40 most sensitive reactions for the generated degradation mechanism of acetone in UV/H_2O_2 process

Rank	Overall sensitivity coefficient	Reaction	Reaction type**
1	154.821	$H_2O_2 + HO\bullet \rightarrow H_2O + HO_2\bullet$	S
2	109.1304	$CH_3COCH_3 + \bullet OH \rightarrow \bullet CH_2COCH_3 + H_2O$	HA
3	30.8718	$HO\bullet + O_2^-\bullet \rightarrow OH^- + O_2$	S
4	25.61243	$CH_3COCHO + H_2O \xrightarrow{HO\bullet} CH_3COCOOH$	HA
5	22.95197	$CH_3COCOO^- + \bullet OH \rightarrow \bullet CH_2COCOO^- + H_2O$	HA
6	22.90226	$CH_3COCOOH + \bullet OH \rightarrow \bullet CH_2COCOOH + H_2O$	HA
7	22.8908	$CH_3COO^- + \bullet OH \rightarrow \bullet CH_2COO^- + H_2O$	HA
8	20.7645	$CH_3COOH + \bullet OH \rightarrow \bullet CH_2COOH + H_2O$	HA
9	17.09768	$O_2^-\bullet + HO_2\bullet \rightarrow HO_2^- + O_2$	S
10	16.55886	$CH_3COCOOH + H_2O_2 \rightarrow CH_3COOH + CO_2$	S
11	14.44321	$HCOO^- + \bullet OH \rightarrow CO_2^-\bullet + H_2O$	HA
12	7.701732	$HCOOH + \bullet OH \rightarrow CO_2^-\bullet + H^+ + H_2O$	HA
13	2.047578	$HOOCCOCOOH + \bullet OH \rightarrow \bullet OOCCOCOOH + H_2O$	HA
14	1.940754	$\bullet CH_2COCH_3 + O_2 \rightarrow \bullet OOCH_2COCH_3$	OA
15	1.836571	$HO\bullet + HO_2\bullet \rightarrow H_2O + O_2$	S
16	1.636074	$HOOCCOO^- + \bullet OH \rightarrow CO_2 + CO_2^-\bullet + H_2O$	HA
17	1.143512	$H^+ + {}^-OOCCOO^- + \bullet OH \rightarrow CO_2 + CO_2^-\bullet + H_2O$	HA
18	1.134597	$HOOCCOOH + \bullet OH \rightarrow CO_2 + CO_2^-\bullet + H^+ + H_2O$	HA
19	1.13327	$CH_3COCH_2OH + \bullet OH \rightarrow CH_3COC^{\bullet}HOH + H_2O$	HA
20	0.621593	$H_2O_2 + HO_2\bullet \rightarrow \bullet OH + H_2O + O_2$	S
21	0.426902	$H_2O_2 + O_2^-\bullet \rightarrow \bullet OH + OH^- + O_2$	S
22	0.297367	$CO_2^-\bullet + H_2O_2 \rightarrow H_2O + CO_2 + \bullet OH$	S
23	0.297366	$CO_2^-\bullet + O_2 \rightarrow O_2^-\bullet + CO_2$	S
24	0.200409	$CH_2(OH)COCOOH + \bullet OH \rightarrow \bullet CH(OH)COCOOH + H_2O$	HA

25	0.108026	$HO_2^- + HO\bullet \rightarrow OH^- + HO_2\bullet$	S
26	0.061838	$CH_2(OH)COOH + \bullet OH \rightarrow \bullet CH(OH)COOH + H_2O$	HA
27	0.051596	$OHCCOOH + H_2O \xrightarrow{HO\bullet} HOOCCOOH$	HA
28	0.012917	$2\ \bullet OOCH_2COCH_3 \rightarrow 2\ \bullet OCH_2COCH_3 + O_2$	PB
29	0.012917	$2\ \bullet OOCH_2COCH_3 \rightarrow 2\ CH_3COCHO + H_2O_2$	PB
30	0.012917	$2\ \bullet OOCH_2COCH_3 \rightarrow CH_3COCHO + CH_3COCH_2OH + O_2$	PB
31	0.009231	$2\ HO_2\bullet \rightarrow H_2O_2 + O_2$	S
32	0.004206	$2\ HO\bullet \rightarrow H_2O_2$	S
33	0.001983	$CH_3COCH_2OH + \bullet OH \rightarrow CH_3COC^\bullet HOH + H_2O$	HA
34	0.001542	$CH_2(OH)COCOOH + \bullet OH \rightarrow \bullet CH(OH)COCOOH + H_2O$	HA
35	0.000211	$2\ \bullet OOCH_2COOH \rightarrow 2\ OHCCOOH + H_2O_2$	PB
36	0.000211	$2\ \bullet OOCH_2COOH \rightarrow OHCCOOH + CH_2(OH)COOH + O_2$	PB
37	0.000211	$2\ \bullet OOCH_2COOH \rightarrow 2\ \bullet OCH_2COOH + O_2$	PB
38	0.000114	$2\ \bullet OOCOCOOH \rightarrow 2\ \bullet OCOCOOH + O_2$	PB
39	4.08E-05	$CH_3COC^\bullet HOH + O_2 \rightarrow \bullet OOCH(OH)COCH_3$	OA
40	3.03E-05	$2\ \bullet OOCH_2COCOOH \rightarrow 2\ \bullet OCH_2COCOOH + O_2$	PB

*GCM: the reaction rate constant is predicted by the Group Contribution Method (GCM) developed by Minakata *et. al* (Minakata et al., 2009).
**Reaction type:
S: special reaction;
HA: hydrogen abstraction reaction by hydroxyl radical;
PB: bimolecular decay of peroxy radical;
OA: oxygen addition;
BS: β scission;
OT: 1,2-H shift;
PH: $HO_2\bullet$ elimination;
R: reduced reaction by directed relation graph (DRG) method (Lu et al., 2005).

Table A.4. Top 50 most sensitive reactions for the generated degradation mechanism of TCE in UV/H_2O_2 process

Rank	Sensitivity coefficient	Reaction	Reaction type**
1	99.31116	$H_2O_2 + {}^\bullet OH \rightarrow H_2O + HO_2^\bullet$	S
2	45.55498	$HCOO^- + {}^\bullet OH \rightarrow CO_2^{\bullet -} + H_2O$	S
3	40.24085	$HCOOH + {}^\bullet OH \rightarrow CO_2^{\bullet -} + H_2O + H^+$	S

4	38.61828	$ClHC{=}CCl_2 + {}^{\bullet}OH \rightarrow ClCH(OH)\text{-}C^{\bullet}Cl_2$	DA
5	34.28115	${}^{\bullet}CHO + H_2O + O_2 \rightarrow HCOOH + O_2^{-\bullet} + H^+$	S
6	34.23631	$ClHC{=}C(Cl)O^{\bullet} + H_2O \rightarrow ClCH_2COOH + Cl^{\bullet}$	S
7	20.08585	$OHC\text{-}C(Cl_2)O^{\bullet} \rightarrow COCl_2 + {}^{\bullet}CHO$	BS
8	20.08556	$OHC\text{-}C(Cl_2)O^{\bullet} \rightarrow OHC\text{-}C(O)Cl + Cl^{\bullet}$	BS
9	19.01211	$ClCH_2COO^- + {}^{\bullet}OH \rightarrow ClC^{\bullet}HCOO^- + H_2O$	HA
10	16.40199	$ClCH_2COOH + {}^{\bullet}OH \rightarrow ClC^{\bullet}HCOOH + H_2O$	HA
11	16.22980	$Cl_2CHCOO^- + {}^{\bullet}OH \rightarrow Cl_2C^{\bullet}COO^- + H_2O$	HA
12	15.03048	$Cl_2CHCOOH + {}^{\bullet}OH \rightarrow Cl_2C^{\bullet}COOH + H_2O$	HA
13	14.98133	$HOOCCOO^- + {}^{\bullet}OH \rightarrow CO_2 + CO_2^{\bullet-} + H_2O$	HA
14	13.90682	$H^+ + OOCCOO^- + {}^{\bullet}OH \rightarrow CO_2 + CO_2^{\bullet-} + H_2O$	HA
15	12.05081	$HOOCCOOH + {}^{\bullet}OH \rightarrow CO_2 + CO_2^{\bullet-} + H_2O + H^+$	HA
16	7.66482	${}^{\bullet}OH + HO_2^{\bullet} \rightarrow H_2O + O_2$	S
17	7.584972	$OHC\text{-}CHCl_2 + H_2O \xrightarrow{HO^{\bullet}} Cl_2CHCOOH$	HA
18	6.968512	$Cl_2CH\text{-}C(Cl_2)O^{\bullet} \rightarrow COCl_2 + {}^{\bullet}CHCl_2$	BS
19	6.968116	$Cl_2CH\text{-}C(Cl_2)O^{\bullet} \rightarrow Cl_2CH\text{-}C(O)Cl + Cl^{\bullet}$	BS
20	6.918041	$OHC\text{-}C(O)Cl + H_2O \rightarrow OHCCOOH + HCl$	XE
21	3.515105	$OHCCOOH + H_2O \xrightarrow{HO^{\bullet}} HOOCCOOH$	HA
22	2.856532	$H_2O_2 + HO_2^{\bullet} \rightarrow {}^{\bullet}OH + H_2O + O_2$	S
23	2.767495	$2\ HO_2^{\bullet} \rightarrow H_2O_2 + O_2$	S
24	2.505145	$2\ {}^{\bullet}OH \rightarrow H_2O_2$	S
25	2.394647	$Cl_2CH\text{-}C(O)Cl + H_2O \rightarrow Cl_2CHCOOH + HCl$	XE
26	2.305301	$OHCCOOH + H_2O_2 \rightarrow HCOOH + CO_2 + H_2O$	S
27	1.530675	$OClC\text{-}COOH + H_2O \rightarrow HOOCCOOH + HCl$	XE
28	0.591761	${}^{\bullet}OCCl_2\text{-}COOH \rightarrow COCl_2 + {}^{\bullet}COOH$	BS
29	0.591254	${}^{\bullet}OCCl_2\text{-}COOH \rightarrow OClC\text{-}COOH + Cl^{\bullet}$	BS
30	0.333891	${}^{\bullet}OCClH\text{-}COOH \rightarrow HCOCl + {}^{\bullet}COOH$	BS
31	0.304	${}^{\bullet}OCClH\text{-}COOH \rightarrow {}^{\bullet}CCl(OH)\text{-}COOH$	BS
32	0.258906	$ClC{\equiv}CCl + {}^{\bullet}OH \rightarrow Cl(OH)C{=}C^{\bullet}Cl$	DA
33	0.130756	${}^{\bullet}OCClH\text{-}COOH \rightarrow OHCCOOH + Cl^{\bullet}$	BS
34	0.093377	$CO_2^{\bullet-} + O_2 \rightarrow CO_2 + O_2^{\bullet-}$	S
35	0.092586	$CO_2^{\bullet-} + H_2O_2 \rightarrow CO_2 + OH^- + {}^{\bullet}OH$	S

36	0.040931	$^{\bullet}OH + O_2^{\bullet-} \rightarrow OH^- + O_2$	S
37	0.016381	$O_2^{\bullet-} + HO_2^{\bullet} \rightarrow HO_2^- + O_2$	S
38	0.01403	$H_2O_2 + O_2^{\bullet-} \rightarrow {}^{\bullet}OH + OH^- + O_2$	S
39	0.002163	$2\ OHC\text{-}C(Cl_2)OO^{\bullet} \rightarrow 2\ OHC\text{-}C(Cl_2)O^{\bullet} + O_2$	PB
40	0.001935	$2\ ClHC{=}C(Cl)OO^{\bullet} \rightarrow 2\ ClHC{=}C(Cl)O^{\bullet} + O_2$	PB
41	0.000528	$ClHC{=}CCl_2 + {}^{\bullet}Cl \rightarrow Cl_2CH\text{-}C^{\bullet}Cl_2$	DA
42	0.00021	$HO_2^- + {}^{\bullet}OH \rightarrow OH^- + HO_2^{\bullet}$	S
43	0.000198	$2\ {}^{\bullet}OOCCl_2\text{-}COOH \rightarrow 2\ {}^{\bullet}OCCl_2\text{-}COOH + O_2$	PB
44	0.000161	$2\ Cl_2CH\text{-}C(Cl_2)OO^{\bullet} \rightarrow 2\ Cl_2CH\text{-}C(Cl_2)O^{\bullet} + O_2$	PB
45	0.000143	$^{\bullet}CCl(OH)\text{-}COOH + O_2 \rightarrow {}^{\bullet}OOCCl(OH)\text{-}COOH$	OA
46	0.000138	$2\ {}^{\bullet}OOCClH\text{-}COOH \rightarrow 2\ {}^{\bullet}OCClH\text{-}COOH + O_2$	PB
47	0.000138	$2\ {}^{\bullet}OOCClH\text{-}COOH \rightarrow 2\ OClC\text{-}COOH + H_2O_2$	PB
48	0.000138	$2\ {}^{\bullet}OOCClH\text{-}COOH \rightarrow OClC\text{-}COOH + ClHC(OH)\text{-}COOH + O_2$	PB
49	9.16E-05	$Cl(OH)C{=}C^{\bullet}Cl \rightarrow O{=}C{=}C^{\bullet}Cl + HCl$	S
50	9.11E-05	$OHC\text{-}C^{\bullet}Cl_2 + O_2 \rightarrow OHC\text{-}C(Cl_2)OO^{\bullet}$	OA

*GCM: the reaction rate constant is predicted by the Group Contribution Method (GCM) developed by Minakata *et. al* (Minakata et al., 2009).
**Reaction type:
S: special reaction;
HA: hydrogen abstraction reaction by hydroxyl radical;
PB: bimolecular decay of peroxy radical;
OA: oxygen addition;
BS: β scission;
OT: 1,2-H shift;
PH: HO_2• elimination;
XE: HCl elimination.

APPENDIX B

DIRECTED RELATION GRAPH CODES

```
/*----------------------------------------------------------------------
 * graph.h
 *
 *    This subroutine contains the generation and reduction of graph
 *
 * Author: Xin Guo
 * Date: 04/05/2012
 * ----------------------------------------------------------------------*/

#ifndef GRAPH_H
#define GRAPH_H

#include "species.h"
#include "reaction.h"
#include "global.h"
#include <vector>
#include <iostream>
using namespace::std;

class graph
{
public:
  graph(int k = 10, int t = 0);
  // Generate the graph from chemical mechanisms
  void create();
  // Reduce the generated graph, e is the criteria
  void reduction(double e = 0);
  // dfs is the depth first search
  void dfs();
  void dfs(int v, int label);
  void reaction();
  int begin(int v);
  int nextvert(int v);

private:
  //time is the tout to process the reduction
  int time;
  //a is the matrix to represent the graph
  double **a;
  //n is the number of species
  int n;
  int *reach;
  int *pos;
  //cr is the criteria for the reduction
  double cr;
};

inline graph::graph(int k, int t)
{
  n = k;
  time = t;
  a = new double *[n+1];
  reach = new int [n+1];
  pos = new int [n+1];
  for (int i=1; i <= n; ++i)
    pos[i]=0;
  for (int j=1; j <= n; ++j)
    a[j] = new double [n+1];
}

//calculate the interaction coefficient
inline void graph::create()
{
  //i is the parent species
  for (int i=0; i != n; ++i)
```

```
{
  //j is the child species
  for (int j=0; j != n; ++j)
  {
    a[i+1][j+1] = 0;
    double up = 0;
    double down = 0;

    // set the reaction p
    for (int p =0; p != rlist.size(); ++p)
    {
     // set the reactant m
     for (int m = 0; m != rlist[p]->reactant.size(); ++m)
     {
        //when we make sure species i exist in reaction p
       if (rlist[p]->reactant[m]->name == slist[i]->name)
       {
          //collect rate of reaction p to down
         down = down -(rlist[p]->trate[time])*(rlist[p]->sto_r[m]);

          //then at the condition that species i is the reactant of reaction p,
         //search the reactant list of reaction p again
         for (int w = 0; w != rlist[p]->reactant.size(); ++w)
         {
            //if we find species j is also in reactant list of reaction p
           if (rlist[p]->reactant[w]->name == slist[j]->name)
              //collect rate of reaction p to up
             up = up -(rlist[p]->trate[time])*(rlist[p]->sto_r[m]);
         }

          //then at the condition that species i is the reactant of reaction p,
          //search the product list of reaction p
         for (int e = 0; e != (*rlist[p]).product.size(); ++e)
         {
            //if we find species j is also in product list of reaction p
           if (rlist[p]->product[e]->name == slist[j]->name)
            //collect rate of reaction p to up
           up = up -(rlist[p]->trate[time])*(rlist[p]->sto_r[m]);
         }
       }
     }

     // set the product n
     for (int n = 0; n != rlist[p]->product.size(); ++n)
     {
       //when we make sure species i exist in reaction p
       if (rlist[p]->product[n]->name == slist[i]->name)
      {
         //collect rate of reaction p to down
        down = down + (rlist[p]->trate[time])*(rlist[p]->sto_p[n]);

         //then at the condition that species i is the product of reaction p,
          //search the reactant list of reaction p
         for (int w = 0; w != rlist[p]->reactant.size(); ++w)
        {
           //if we find species j is also in reactant list of reaction p
          if (rlist[p]->reactant[w]->name == slist[j]->name)
             //collect rate of reaction p to up
            up = up + (rlist[p]->trate[time])*(rlist[p]->sto_p[n]);
        }

         //then at the condition that species i is the product of reaction p,
          //search the product list of reaction p
        for (int e = 0; e != rlist[p]->product.size(); ++e)
        {
           //if we find species j is also in product list of reaction p
          if (rlist[p]->product[e]->name == slist[j]->name)
           //collect rate of reaction p to up
          up = up + (rlist[p]->trate[time])*(rlist[p]->sto_p[n]);
        }
      }
```

```
        }
      }
      a[i+1][j+1] = up/down;
    }
   }

 for (int z=1; z <= n; ++z)  reach[z]=0;
}

inline void graph::reduction(double e)
{
  cr = e;
  for (int i = 1; i <= n; ++i)
  {
    for (int j = 1; j <= n; ++j)
    {
      if (a[i][j] < cr)  a[i][j] = 0;
    }
  }
}

inline void graph::dfs()
{
  int label = 0;
  int i = 1;
  if(!reach[i])
  {
    label++;
    dfs(i, label);
  }

  //Generate the spicies list of removed species
  for (int m = 1; m <= n; ++m)
  {
    if (reach[m] == 0)
    {
      slistm[time].push_back(slist[m-1]);
    }
  }
}

inline void graph::dfs(int v, int label)
{
  slistr[time].push_back(slist[v-1]);
  reach[v] = label;
  int u = begin(v);
  while(u)
  {
    if(!reach[u])
    dfs(u, label);
    u = nextvert(v);
  }
}

inline int graph::begin(int v)
{
  if((v<1)||(v>n))
    cout<<"Bad input" <<endl;
  else {
    for(int i = 1; i <= n; ++i)
    {
      if(a[v][i] > 0)
      {
        pos[v] = i;
       return i;
      }
    }
  }
  return 0;
}
```

```
inline int graph::nextvert(int v)
{
  if ((v<1)&&(v>n))
  cout << "Bad input"<<endl;
  else {
    for(int i = pos[v]+1; i <= n; ++i)
    if(a[v][i] > 0)
    {
      pos[v]=i;
      return i;
    }
   }
   return 0;
}

inline void graph::reaction()
{
  for (int i = 0; i != slistm[time].size(); ++i)
  {
    for (int j = 0; j != rlist.size(); ++j)
    {
      for (int v = 0; v != rlist[j]->reactant.size(); ++v)
      {
       if (rlist[j]->reactant[v]->name == slistm[time][i]->name) rlist[j]->ex = false;
      }
      for (int w = 0; w != rlist[j]->product.size(); ++w)
      {
        if (rlist[j]->product[w]->name == slistm[time][i]->name)  rlist[j]->ex = false;
      }
    }
  }

  for (int i = 0; i != rlist.size(); ++i)
  {
    if (rlist[i]->ex == true)  rlistr[time].push_back(rlist[i]);
  }

  //reset the ex of each reaction in rlist to true for the next iteration
  for (int i = 0; i != rlist.size(); ++i)
  {
    rlist[i]->ex = true;
  }
}

#ENDIF
```

APPENDIX C

REACTIONS INCLUDED IN THE DEGRADATION MECHANISM OF POLYETHYLENE GLYCOL (PEG) IN UV/H_2O_2 PROCESS GENERATED BY THE COMPUTER-BASED KMC MODEL

Table C.1. Reactions included in the generated mechanism for the degradation of PEG in UV/H_2O_2 process

	Reaction	Rate constant ($M^{-1}s^{-1}$)	References
1	$H_2O_2 + h\nu \rightarrow 2\ \bullet OH$	Φ_{H2O2} =	Hunt et al., 1952
2	$H_2O_2 + HO\bullet \rightarrow H_2O + HO_2\bullet$	2.7×10^7	Buxton et al., 1988
3	$HO_2^- + HO\bullet \rightarrow OH^- + HO_2\bullet$	7.5×10^9	Buxton et al., 1988
4	$H_2O_2 + HO_2\bullet \rightarrow \bullet OH + H_2O + O_2$	3	Buxton et al., 1988
5	$H_2O_2 + O_2^-\bullet \rightarrow \bullet OH + OH^- + O_2$	0.13	Buxton et al., 1988
6	$2\ HO\bullet \rightarrow H_2O_2$	5.5×10^9	Buxton et al., 1988
7	$HO\bullet + HO_2\bullet \rightarrow H_2O + O_2$	6.6×10^9	Elliott et al., 1992
8	$2\ HO_2\bullet \rightarrow H_2O_2 + O_2$	8.3×10^5	Bielski et al., 1985
9	$O_2^-\bullet + HO_2\bullet \rightarrow HO_2^- + O_2$	9.7×10^7	Bielski et al., 1985
10	$HO\bullet + O_2^-\bullet \rightarrow OH^- + O_2$	7×10^9	Elliott et al., 1992
11	$-CH_2-CH_2-O-CH_2-CH_2-O- + HO\bullet \rightarrow$ $-CH_2-{}^{\bullet}CH-O-CH_2-CH_2-O- + H_2O$	6.61×10^8	GCM*
12	$-CH_2-{}^{\bullet}CH-O-CH_2-CH_2-O- + O_2 \rightarrow$ $-CH_2-CH(OO\bullet)-O-CH_2-CH_2-O-$	1×10^9	Estimated based on Neta et al., 1996
13	$2-CH_2-CH(OO\bullet)-O-CH_2-CH_2-O- \rightarrow$ $2-CH_2-CH(O\bullet)-O-CH_2-CH_2-O- + O_2$	2×10^9	Estimated based on von Sonntag et al., 1991
14	$2-CH_2-CH(OO\bullet)-O-CH_2-CH_2-O- \rightarrow$ $2-CH_2-C(=O)-O-CH_2-CH_2-O- + H_2O_2$	2×10^9	Estimated based on von Sonntag et al., 1991
15	$2-CH_2-CH(OO\bullet)-O-CH_2-CH_2-O- \rightarrow$ $-CH_2-C(=O)-O-CH_2-CH_2-O- +$ $-CH_2-CH(OH)-O-CH_2-CH_2-O- + O_2$	2×10^9	Estimated based on von Sonntag et al., 1991
16	$-CH_2-CH(OH)-O-CH_2-CH_2-O- + O_2 + HO\bullet \rightarrow \rightarrow$ $-CH_2-C(=O)-O-CH_2-CH_2-O- + HO_2\bullet + H_2O$	7.44×10^8	GCM*
17	$-CH_2-CH(O\bullet)-O-CH_2-CH_2-O- \rightarrow$ $-CH_2-CHO + \bullet O-CH_2-CH_2-O-$	1×10^5 s^{-1}	Estimated based on Li et al., 2009

18	$-CH_2-CHO+H_2O \xrightarrow{HO\bullet} -CH_2-COOH$	7.81×10^8	GCM*
19	$\bullet O-CH_2-CH_2-O- \rightarrow HCHO + \bullet CH_2-O-$	1×10^5 s^{-1}	Estimated based on Li et al., 2009
20	$\bullet O-CH_2-CH_2-O- + -CH_2-CH_2-O- \rightarrow$ $HO-CH_2-CH_2-O-+-CH_2-\bullet CH-O-$	1×10^5	Estimated based on Baignee et al., 1983
21	$\bullet CH_2-O-+ O_2 \rightarrow \bullet OOCH_2-O-$	1×10^9	Estimated based on Neta et al., 1996
22	$2\bullet OOCH_2-O- \rightarrow HOCH_2-O- + OHC-O-+ O_2$	2×10^9	Estimated based on von Sonntag et al., 1991
23	$2\bullet OOCH_2-O- \rightarrow 2OHC-O-+ H_2O_2$	2×10^9	Estimated based on von Sonntag et al., 1991
24	$2\bullet OOCH_2-O- \rightarrow 2\bullet OCH_2-O-+ O_2$	2×10^9	Estimated based on von Sonntag et al., 1991
25	$OHC-O-+H_2O \xrightarrow{HO\bullet} HOOC-O-$	3.66×10^8	GCM*
26	$HOCH_2CH_2OH + HO\bullet \rightarrow HO\bullet CHCH_2OH + H_2O$	6.93×10^8	GCM*
27	$HO\bullet CHCH_2OH + O_2 \rightarrow \bullet OOCH(OH)CH_2OH$	1×10^9	Estimated based on von Sonntag et al., 1991
28	$\bullet OOCH(OH)CH_2OH \rightarrow OHCCH_2OH + HO_2\bullet$	1×10^3 s^{-1}	Estimated based on Neta et al., 1990
29	$OHCCH_2OH + H_2O \xrightarrow{HO\bullet} HOOCCH_2OH$	7.81×10^8	GCM*
30	$HOOCCH_2OH + HO\bullet \rightarrow HOOC\bullet CHOH + H_2O$	6×10^8	Buxton et al., 1988
31	$^-OOCCH_2OH + HO\bullet \rightarrow {}^-OOC\bullet CHOH + H_2O$	8.6×10^8	Buxton et al., 1988
32	$HOOC\bullet CHOH + O_2 \rightarrow \bullet OOCH(OH)COOH$	1×10^9	Estimated based on von Sonntag et al., 1991
33	$\bullet OOCH(OH)COOH \rightarrow OHCCOOH + HO_2\bullet$	1×10^3 s^{-1}	Estimated based on Neta et al., 1990
34	$OHCCOOH + H_2O \xrightarrow{HO\bullet} HOOCCOOH$	2.86×10^7	GCM*
35	$OHCCOOH + H_2O_2 \rightarrow HCOOH + CO_2 + H_2O$	0.3	Leitzke et al., 2001
36	$HOOCCOOH + \bullet OH \rightarrow CO_2 + CO_2^{\bullet-} + H_2O + H^+$	1.4×10^6	Buxton et al., 1988
37	$HOOCCOO^- + \bullet OH \rightarrow CO_2 + CO_2^{\bullet-} + H_2O$	4.7×10^7	Buxton et al., 1988
38	$H^+ + OOCCOO^- + \bullet OH \rightarrow CO_2 + CO_2^{\bullet-} + H_2O$	7.7×10^6	Buxton et al., 1988
39	$HCHO + H_2O \xrightarrow{HO\bullet} HCOOH$	3.41×10^8	GCM*
40	$HCOOH + \bullet OH \rightarrow CO_2^{\bullet-} + H_2O + H^+$	1.3×10^8	Buxton et al., 1988
41	$HCOO^- + \bullet OH \rightarrow CO_2^{\bullet-} + H_2O$	3.2×10^9	Buxton et al., 1988
42	$CO_2^{\bullet-} + O_2 \rightarrow CO_2 + O_2^{\bullet-}$	2×10^9	Neta et al., 1990
43	$CO_2^{\bullet-} + H_2O_2 \rightarrow CO_2 + OH^- + \bullet OH$	6.3×10^5	Schwarz et al., 1992

44	$H_2O_2 \Leftrightarrow H^+ + HO_2^-$	pK_a =	Perry et al., 1981
45	$HO_2\bullet \Leftrightarrow H^+ + O_2^-\bullet$	pK_a = 4.8	Bielski et al., 1985
46	$HCOOH \Leftrightarrow H^+ + HCOO^-$	pK_a =	Perry et al., 1981
47	$HOOCCOOH \Leftrightarrow H^+ + HOOCCOO^-$	pK_a =	Perry et al., 1981
48	$HOOCCOO^- \Leftrightarrow H^+ + {}^-OOCCOO^-$	pK_a =	Perry et al., 1981
49	$HOCH_2COOH \Leftrightarrow H^+ + HOCH_2COO^-$	pK_a = 3.8	Perry et al., 1981

*GCM: the reaction rate constant is predicted by the Group Contribution Method (GCM) developed by Minakata *et al*. (Minakata et al., 2009)

Table C.2. Sensitivity analysis for the generated degradation mechanism of PEG in UV/H_2O_2 process

Rank	Reaction	Sensitivity coefficient	Reaction type**
1	$H_2O_2 + h\nu \rightarrow 2\ \bullet OH$	0.0745	S
2	$H_2O_2 + HO\bullet \rightarrow H_2O + HO_2\bullet$	0.0551	S
3	$-CH_2-CH_2-O-CH_2-CH_2-O- + HO\bullet \rightarrow$ $-CH_2-{}^\bullet CH-O-CH_2-CH_2-O- + H_2O$	0.0479	HA
4	$2\ HO_2\bullet \rightarrow H_2O_2 + O_2$	0.0476	S
5	$H_2O_2 + O_2^-\bullet \rightarrow \bullet OH + OH^- + O_2$	0.0430	S
6	$HOCH_2CH_2OH + HO\bullet \rightarrow HO^\bullet CHCH_2OH + H_2O$	0.0424	HA
7	$2\ HO\bullet \rightarrow H_2O_2$	0.0399	S
8	$HO\bullet + O_2^-\bullet \rightarrow OH^- + O_2$	0.0389	S
9	$-CH_2-CHO + H_2O \xrightarrow{HO\bullet} -CH_2-COOH$	0.0301	HA
10	$-CH_2-CH(OH)-O-CH_2-CH_2-O- + O_2 + HO\bullet \rightarrow \rightarrow$ $-CH_2-C(=O)-O-CH_2-CH_2-O- + HO_2\bullet + H_2O$	0.0290	HA
11	$OHCCH_2OH + H_2O \xrightarrow{HO\bullet} HOOCCH_2OH$	0.0283	HA
12	$H_2O_2 + HO_2\bullet \rightarrow \bullet OH + H_2O + O_2$	0.0276	S
13	$HO\bullet + HO_2\bullet \rightarrow H_2O + O_2$	0.0252	S
14	$OHCCOOH + H_2O \xrightarrow{HO\bullet} HOOCCOOH$	0.0178	HA
15	$OHCCOOH + H_2O_2 \rightarrow HCOOH + CO_2 + H_2O$	0.0175	S
16	$O_2^-\bullet + HO_2\bullet \rightarrow HO_2^- + O_2$	0.0165	S
17	$H^+ + OOCCOO^- + {}^\bullet OH \rightarrow CO_2 + CO_2^{\bullet -} + H_2O$	0.0098	HA
18	$HOOCCOO^- + {}^\bullet OH \rightarrow CO_2 + CO_2^{\bullet -} + H_2O$	0.0094	HA
19	$HOOCCOOH + {}^\bullet OH \rightarrow CO_2 + CO_2^{\bullet -} + H_2O + H^+$	0.0090	HA
20	$HCHO + H_2O \xrightarrow{HO\bullet} HCOOH$	0.0085	HA
21	$HCOO^- + {}^\bullet OH \rightarrow CO_2^{\bullet -} + H_2O$	0.0073	HA
22	$HCOOH + {}^\bullet OH \rightarrow CO_2^{\bullet -} + H_2O + H^+$	0.0071	HA

23	$HO_2^- + HO\bullet \rightarrow OH^- + HO_2\bullet$	0.0054	S
24	$OHC-O-+H_2O \xrightarrow{HO\bullet} HOOC-O-$	0.0043	HA
25	$^-OOCCH_2OH + HO\bullet \rightarrow {}^-OOC^{\bullet}CHOH + H_2O$	0.0023	HA
26	$HOOCCH_2OH + HO\bullet \rightarrow HOOC^{\bullet}CHOH + H_2O$	0.0021	HA
27	$2-CH_2-CH(OO\bullet)-O-CH_2-CH_2-O- \rightarrow$ $2-CH_2-CH(O\bullet)-O-CH_2-CH_2-O- + O_2$	0.0016	PB
28	$2-CH_2-CH(OO\bullet)-O-CH_2-CH_2-O- \rightarrow$ $2-CH_2-C(=O)-O-CH_2-CH_2-O- + H_2O_2$	0.0016	PB
29	$2-CH_2-CH(OO\bullet)-O-CH_2-CH_2-O- \rightarrow$ $-CH_2-C(=O)-O-CH_2-CH_2-O-+$ $-CH_2-CH(OH)-O-CH_2-CH_2-O-+O_2$	0.0016	PB
30	$2\bullet OOCH_2-O- \rightarrow 2\bullet OCH_2-O-+O_2$	0.0008	PB
31	$2\bullet OOCH_2-O- \rightarrow 2OHC-O-+H_2O_2$	0.0008	PB
32	$2\bullet OOCH_2-O- \rightarrow HOCH_2-O- + OHC-O-+O_2$	0.0008	PB
33	$CO_2^{\bullet-} + O_2 \rightarrow CO_2 + O_2^{\bullet-}$	0.0003	S
34	$CO_2^{\bullet-} + H_2O_2 \rightarrow CO_2 + OH^- + {}^{\bullet}OH$	0.0002	S
35	$-CH_2-{}^{\bullet}CH-O-CH_2-CH_2-O- + O_2 \rightarrow$ $-CH_2-CH(OO\bullet)-O-CH_2-CH_2-O-$	1.1E-04	OA
36	$HOOC^{\bullet}CHOH + O_2 \rightarrow \bullet OOCH(OH)COOH$	9.2E-05	OA
37	$-CH_2-CH(O\bullet)-O-CH_2-CH_2-O- \rightarrow$ $-CH_2-CHO + \bullet O-CH_2-CH_2-O-$	8.8E-05	BS
38	$HO^{\bullet}CHCH_2OH + O_2 \rightarrow \bullet OOCH(OH)CH_2OH$	8.5E-05	OA
39	$\bullet OOCH(OH)CH_2OH \rightarrow OHCCH_2OH + HO_2\bullet$	8.4E-05	PH
40	$\bullet OOCH(OH)COOH \rightarrow OHCCOOH + HO_2\bullet$	6.6E-05	PH
41	$\bullet O-CH_2-CH_2-O- +-CH_2-CH_2-O- \rightarrow$ $HO-CH_2-CH_2-O-+-CH_2-{}^{\bullet}CH-O-$	6.1E-05	HA
42	$\bullet O-CH_2-CH_2-O- \rightarrow HCHO + \bullet CH_2-O-$	4.3E-06	BS
43	$\bullet CH_2-O-+O_2 \rightarrow \bullet OOCH_2-O-$	3.9E-06	OA

*GCM: the reaction rate constant is predicted by the Group Contribution Method (GCM) developed by Minakata *et al*. (Minakata et al., 2009)
**Reaction type:
S: special reaction;
HA: hydrogen abstraction reaction by hydroxyl radical;
PB: bimolecular decay of peroxy radical;
OA: oxygen addition;
BS: β scission;
PH: HO_2• elimination;

APPENDIX D

ON-THE-FLY KINETIC MONTE CARLO SIMULATION OF POLYACRYLAMIDE DEGRADATION IN AQUEOUS PHASE UV/TIO_2 ADVANCED OXIDATION PROCESS

Table D.1. Reactions included in the generated mechanism for the degradation of PAM in UV/TiO_2 process

	Reaction	Rate constant ($M^{-1}s^{-1}$)	References
1	$H_2O_2 + h\nu \rightarrow 2\ \bullet OH$	Φ_{H2O2} =	Hunt et al., 1952
2	$H_2O_2 + HO\bullet \rightarrow H_2O + HO_2\bullet$	2.7×10^7	Buxton et al., 1988
3	$HO_2^- + HO\bullet \rightarrow OH^- + HO_2\bullet$	7.5×10^9	Buxton et al., 1988
4	$H_2O_2 + HO_2\bullet \rightarrow \bullet OH + H_2O + O_2$	3	Buxton et al., 1988
5	$H_2O_2 + O_2^-\bullet \rightarrow \bullet OH + OH^- + O_2$	0.13	Buxton et al., 1988
6	$2\ HO\bullet \rightarrow H_2O_2$	5.5×10^9	Buxton et al., 1988
7	$HO\bullet + HO_2\bullet \rightarrow H_2O + O_2$	6.6×10^9	Elliott et al., 1992
8	$2\ HO_2\bullet \rightarrow H_2O_2 + O_2$	8.3×10^5	Bielski et al., 1985
9	$O_2^-\bullet + HO_2\bullet \rightarrow HO_2^- + O_2$	9.7×10^7	Bielski et al., 1985
10	$HO\bullet + O_2^-\bullet \rightarrow OH^- + O_2$	7×10^9	Elliott et al., 1992
11	$-CH_2-CH(CONH_2)-CH_2-CH(CONH_2)- + HO\bullet \rightarrow$ $-CH_2-CH(CONH_2)-{}^{\bullet}CH-CH(CONH_2)- + H_2O$	1.41×10^9	GCM*
12	$-CH_2-CH(CONH_2)-{}^{\bullet}CH-CH(CONH_2)- + O_2 \rightarrow$ $-CH_2-CH(CONH_2)-CH(OO\bullet)-CH(CONH_2)-$	1×10^9	Estimated based on Neta et al., 1996
13	$2-CH_2-CH(CONH_2)-CH(OO\bullet)-CH(CONH_2)- \rightarrow$ $2-CH_2-CH(CONH_2)-CH(O\bullet)-CH(CONH_2)- + O_2$	2×10^9	Estimated based on von Sonntag et al., 1991
14	$2-CH_2-CH(CONH_2)-CH(OO\bullet)-CH(CONH_2)- \rightarrow$ $2-CH_2-CH(CONH_2)-C(=O)-CH(CONH_2)- + H_2O_2$	2×10^9	Estimated based on von Sonntag et al., 1991
15	$2-CH_2-CH(CONH_2)-CH(OO\bullet)-CH(CONH_2)- \rightarrow$ $-CH_2-CH(CONH_2)-C(=O)-CH(CONH_2)- +$ $-CH_2-CH(CONH_2)-CH(OH)-CH(CONH_2)- + O_2$	2×10^9	Estimated based on von Sonntag et al., 1991
16	$-CH_2-CH(CONH_2)-CH(OH)-CH(CONH_2)-$ $+ O_2 + HO\bullet \rightarrow \rightarrow$ $-CH_2-CH(CONH_2)-C(=O)-CH(CONH_2)-$ $+ HO_2\bullet + H_2O$	1.59×10^9	GCM*

17	$-CH_2-CH(CONH_2)-CH(O\bullet)-CH(CONH_2)- \rightarrow$ $-CH_2-{}^{\bullet}CH(CONH_2) + OHC-CH(CONH_2)-$	1×10^5 s^{-1}	Estimated based on Li et al., 2009
18	$OHC-CH(CONH_2)- + H_2O \xrightarrow{HO\bullet}$ $HOOC-CH(CONH_2)-$	7.81×10^8	GCM*
19	$-CH_2-CH(CONH_2)-CH_2-CH(CONH_2)- + HO\bullet \rightarrow$ $-CH_2-{}^{\bullet}C(CONH_2)-CH_2-CH(CONH_2)- + H_2O$	4.22×10^8	GCM*
20	$-CH_2-{}^{\bullet}C(CONH_2)-CH_2-CH(CONH_2)- + O_2 \rightarrow$ $-CH_2-C(CONH_2)(OO\bullet)-CH_2-CH(CONH_2)-$	1×10^9	Estimated based on Neta et al., 1996
21	$2-CH_2-C(CONH_2)(OO\bullet)-CH_2-CH(CONH_2)- \rightarrow$ $2-CH_2-C(CONH_2)(O\bullet)-CH_2-CH(CONH_2)- + O_2$	2×10^9	Estimated based on von Sonntag et al., 1991
22	$-CH_2-C(CONH_2)(O\bullet)-CH_2-CH(CONH_2)- \rightarrow$ $-CH(CONH_2)-CH_2\bullet +$ $O=C(CONH_2)-CH_2-CH(CONH_2)-$	1×10^5 s^{-1}	Estimated based on Li et al., 2009
23	$-CH(CONH_2)-CH_2\bullet + O_2 \rightarrow$ $-CH(CONH_2)-CH_2OO\bullet$	1×10^9	Estimated based on Neta et al., 1996
24	$2-CH(CONH_2)-CH_2OO\bullet \rightarrow$ $2-CH(CONH_2)-CH_2O\bullet + O_2$	2×10^9	Estimated based on von Sonntag et al., 1991
25	$2-CH(CONH_2)-CH_2OO\bullet \rightarrow$ $2-CH(CONH_2)-CH_2OH + H_2O_2$	2×10^9	Estimated based on von Sonntag et al., 1991
26	$2-CH(CONH_2)-CH_2OO\bullet \rightarrow$ $-CH(CONH_2)-CH_2OH + -CH(CONH_2)-CHO + O_2$	2×10^9	Estimated based on von Sonntag et al., 1991
27	$-CH(CONH_2)-CHO + O_2 + HO\bullet \rightarrow\rightarrow$ $-CH(CONH_2)-COOH + HO_2\bullet + H_2O$	1.59×10^9	GCM*
28	$-CH(CONH_2)-CH_2O\bullet \rightarrow$ $-CH_2-{}^{\bullet}CH(CONH_2) + HCHO$	1×10^5 s^{-1}	Estimated based on Li et al., 2009
29	$-CH_2-{}^{\bullet}CH(CONH_2) + O_2 \rightarrow$ $-CH_2-CH(CONH_2)OO\bullet$	1×10^9	Estimated based on Neta et al., 1996
30	$2-CH_2-CH(CONH_2)OO\bullet \rightarrow$ $2-CH_2-CH(CONH_2)O\bullet + O_2$	2×10^9	Estimated based on von Sonntag et al., 1991
31	$2-CH_2-CH(CONH_2)OO\bullet \rightarrow$ $2-CH_2-CH(CONH_2)OH + H_2O_2$	2×10^9	Estimated based on von Sonntag et al., 1991
32	$2-CH_2-CH(CONH_2)OO\bullet \rightarrow$ $-CH_2-CH(CONH_2)OH + -CH_2-CO-(CONH_2) + O_2$	2×10^9	Estimated based on von Sonntag et al., 1991
33	$-CH_2-CH(CONH_2)OH + O_2 + HO\bullet \rightarrow\rightarrow$ $-CH_2-CO-(CONH_2) + HO_2\bullet + H_2O$	1.59×10^9	GCM*

34	$-CH_2-CH(CONH_2)O\bullet \rightarrow$ $-CH(CONH_2)-CH_2\bullet + OHCCONH_2$	1×10^5 s^{-1}	Estimated based on Li et al., 2009
35	$OHC\,CONH_2 + H_2O \xrightarrow{HO\bullet} HOOC\,CONH_2$	7.81×10^8	GCM*
36	$HOOC\,CONH_2 + HO\bullet \rightarrow\rightarrow CO_2 + H_2O + NO_3^- + H^+$	10^5	Karpel et al., 2002
37	$HCHO + H_2O \xrightarrow{HO\bullet} HCOOH$	3.41×10^8	GCM*
38	$HCOOH + {}^\bullet OH \rightarrow CO_2^{\bullet-} + H_2O + H^+$	1.3×10^8	Buxton et al., 1988
39	$HCOO^- + {}^\bullet OH \rightarrow CO_2^{\bullet-} + H_2O$	3.2×10^9	Buxton et al., 1988
40	$CO_2^{\bullet-} + O_2 \rightarrow CO_2 + O_2^{\bullet-}$	2×10^9	Neta et al., 1990
41	$CO_2^{\bullet-} + H_2O_2 \rightarrow CO_2 + OH^- + {}^\bullet OH$	6.3×10^5	Schwarz et al., 1992
42	$H_2O_2 \Leftrightarrow H^+ + HO_2^-$	pK_a =	Perry et al., 1981
43	$HO_2\bullet \Leftrightarrow H^+ + O_2^-\bullet$	pK_a =	Bielski et al., 1985
44	$HCOOH \Leftrightarrow H^+ + HCOO^-$	pK_a =	Perry et al., 1981

*GCM: the reaction rate constant is predicted by the Group Contribution Method (GCM) developed by Minakata *et al*. (Minakata et al., 2009)

APPENDIX E

DEVELOPMENT OF SIMPLIFIED MODELS FOR ADVANCED OXIDATION PROCESSES

E.1 Introduction

Advanced oxidation processes (AOPs) that produce highly reactive hydroxyl radicals at ambient temperature and atmospheric pressure are attractive and promising water and wastewater treatment technologies. In sustainable development of water and wastewater treatment technologies, AOPs can play significant roles. For example, AOPs can potentially mineralize toxic organic compounds via radical involved chain reactions and do not leave any hazardous wastes if adequate design is applied. In water reuse and water reclamation areas, it is a common practice to employ a combination of ultraviolet with hydrogen peroxide (UV/H_2O_2) AOP for the removal of specific organic contaminants (e.g., 1,4-dioxane, NDMA) after the RO process. The energy consumption of UV/H_2O_2 contributes approximately 7% of overall energy usages in the water reclamation process, and therefore, AOP is a competitive technology with other water treatment technologies (e.g., RO, MF, and UF). Although in design of AOPs we maximize removal efficacy of organic compounds and minimize energy usage in AOPs per removal of order of the target compound, there is a trade-off between these parameters. For example, in UV/H_2O_2, increasing the dosage of hydrogen peroxide increases the removal efficacy of target compound by absorbing more fraction of UV light to produce hydroxyl radicals, while an excess dosage of hydrogen peroxide might decrease the removal efficacy and energy efficiency by increasing the scavenging of

hydroxyl radical by hydrogen peroxide. Accordingly, there is a need to develop a tool to evaluate these treatment design parameters at first place.

Simplified pseudo-steady state model and pseudo-steady state model are useful tools to optimize these design and operational parameters in AOPs. Although there are some limitations that result from the steady-state assumptions, they are precise enough to examine the feasibility of the AOPs. In the simplified pseudo-steady analysis, steady-state concentrations of radicals do not change with time and are equal to the initial steady-state concentrations. The steady-state hydroxyl radical concentration can be solved analytically. The pseudo-steady state model assumes net zero of the rate of radical species that are involved in AOPs but radical concentrations change with time. Accordingly, an ordinary differential equation (ODE) should be solved numerically to obtain time-dependent concentration profile of hydroxyl radical. Although several models for AOPs have already been developed in peer-reviewed research articles (Glaze *et al*., 1995; Lay, 1989; and Stefan *et al*., 1996), none of them developed a learning module or actual tools for users to calculate and optimize their AOP design.

In this module, we develop tools that are easy to use for the purpose of designing AOPs. In these tools, we include two AOPs simulation models: 1) simplified pseudo-steady state model and 2) pseudo-steady state model for ozone with hydrogen peroxide and ultraviolet photolysis with hydrogen peroxide AOPs, respectively. We consider flow conditions in various reactors that include completely mixed batch reactor (CMBR), completely mixed flow reactor (CMFR), plug flow reactor (PFR), tanks-in-series (TIS) reactors, and dispersed flow reactor (DFR). Users can estimate and optimize their design of AOPs with respect to removal efficacy and energy efficiency by calculating the

effluent concentration of a target compound of interest and the energy efficiency per removal order (EE/O) values (Bolton and Cater, 1994). In addition, users can also learn how to develop AOPs models from this module by reading this module, where background knowledge and development processes for various AOPs models in various reactors are presented. A Microsoft Excel spread sheet associated with simplified pseudo-steady state models and MathCAD files associated with pseudo-steady state models are available free of charge via the Internet at http://www.csengin.org/csengine/. In the sample problem section, examples about how AOPs can be designed from the sustainable water and wastewater treatment point of view by removing target contaminants and minimizing overall energy usage are given.

Because this module requires readers to have some background knowledge of advanced oxidation processes with process principles and reaction kinetics, readers are referred to read the book *Water Treatment Principles and Design* (3rd edition), written by Crittenden *et al.* (2012).

E.2 Simplified Pseudo-Steady State Models

In this module, the simplified pseudo-steady state models include: 1) H_2O_2/O_3 model; 2) H_2O_2 added after O_3 addition model; 3) UV/H_2O_2 model; and 4) O_3 - R_c model. The reactor types include: 1) tanks-in-series (TIS) reactor; 2) completely mixed batch reactor (CMBR); 3) completely mixed flow reactor (CMFR); 4) plug flow reactor (PFR); and 5) dispersed flow reactor (DFR) in closed systems. Table E1 lists important elementary reactions that are involved in these models. It is noted that we excluded reactions that occur less likely than above reactions (e.g., $HO\cdot + HO\cdot$). In the following

part, the development processes of all these four simplified pseudo-steady state models are described separately.

Table E.1. Important elementary reactions that are involved in the AOPs

No.	Reactions	Rate constants, $M^{-1}s^{-1}$	Source
	Reactions specifically for H_2O_2/O_3 process		
1	$HO_2^- + O_3 \rightarrow O_3^-\bullet + HO_2\bullet$	$k_1 = 2.8\times10^6$	a
2	$OH^- + O_3 \rightarrow HO_2^- + O_2$	$k_2 = 70$	a
3	$O_2^-\bullet + O_3 \rightarrow O_3^-\bullet + O_2$	$k_3 = 1.6\times10^9$	b
4	$O_3^-\bullet + H^+ \rightarrow HO_3\bullet$	$k_4 = 5.2\times10^{10}$	b
5	$HO_3\bullet \rightarrow HO\bullet + O_2$	$k_5 = 1.1\times10^5\ s^{-1}$	b
6	$O_3 + R \rightarrow$ Products	k_6=?	
7	$O_3 + HO\bullet \xrightarrow{k_7} HO_2\bullet + O_2$	$k_7 = 2.6\times10^8$	a
	Reactions specifically for H_2O_2/UV process		
8	$H_2O_2 + hv \rightarrow 2HO\bullet$	$r_{UV,H_2O_2} = -r_{HO\bullet}/2 = -\Phi_{H_2O_2} P_{U\text{-}V} f_{H_2O_2} \left(1-e^{-A}\right)$ $A = 2.303b\left(\varepsilon_{H_2O_2} C_{H_2O_2} + \varepsilon_{HO_2^-} C_{HO_2^-} + \varepsilon_R C_R + \varepsilon_{NOM} C_{NOM}\right)$ $f_{H_2O_2} = 2.303b\left(\varepsilon_{H_2O_2} C_{H_2O_2} + \varepsilon_{HO_2^-} C_{HO_2^-}\right)/A$ $\varepsilon_{H_2O_2,254nm} = 17.9\sim19.6\ M^{-1}cm^{-1}$ $\Phi_{H_2O_2} = \Phi_{HO_2^-} = 0.5$	
9	$R + hv \rightarrow$ Products	$r_{UV,R} = -\Phi_R P_{U\text{-}V} f_R \left(1-e^{-A}\right)$ $f_R = 2.303b\,\varepsilon_R C_R / A$	
	Reactions common for both H_2O_2/O_3 and H_2O_2/UV processes		
10	$HO\bullet + HO_2^- \rightarrow OH^- + HO_2\bullet$	$k_{10} = 7.5\times10^9$	c
11	$HO\bullet + H_2O_2 \rightarrow H_2O + HO_2\bullet$	$k_{11} = 2.7\times10^7$	d
12	$HO\bullet + HCO_3^- \rightarrow CO_3^-\bullet + H_2O$	$k_{12} = 8.5\times10^6$	d
13	$HO\bullet + R \rightarrow$ Products	k_{13} (See *GCM)	
14	$HO\bullet + NOM \rightarrow$ Products	$k_{14} = 1.39\times10^8$ to 4.53×10^8 (average = 2.23×10^8)	e
15	$HO\bullet + Cl^- \rightarrow$ Products	$k_{15} = 4.3\times10^9$	d
16	$HO\bullet + CO_3^{2-} \rightarrow CO_3^-\bullet + OH^-$	$k_{16} = 3.9\times10^8$	d

17	$HO\bullet + Fe^{2+} \rightarrow$ Products	$k_{17} = 2.3\times10^{8}$	d
18	$HO\bullet + Mn^{2+} \rightarrow$ Products	$k_{18} = 1.4\times10^{8}$	d
	Acid dissociation constants		
19	$H_2CO_3^* \rightleftarrows H^+ + HCO_3^-$	$pK_{a1} = 6.3$	f
20	$HCO_3^- \rightleftarrows H^+ + CO_3^{2-}$	$pK_{a2} = 10.3$	f
21	$H_2O \rightleftarrows H^+ + OH^-$	$pK_{a3} = 14$	f
22	$H_2O_2 \rightleftarrows H^+ + HO_2^-$	$pK_{a5} = 11.75$	g
23	$HO_2\bullet \rightleftarrows H^+ + O_2^-\bullet$	$pK_{a6} = 4.8$	a

References: (a) Staehelin and Hoigne, 1982; (b) Buhler *et al*., 1984; (c) Christensen *et al*., 1982; (d) Buxton and Greenstock, 1988; (e) Westerhoff *et al*., 2007; (f) Stumm and Morgan, 1981; (g) Behar *et al*., 1970.

E.2.1 Ozone with Hydrogen Peroxide Model

The H_2O_2/O_3 model is a process in which gaseous ozone is injected in water and hydrogen peroxide is added simultaneously. The gaseous ozone is transferred into water via mass transfer process. Accordingly, initial chemical reactions take place in the presence of hydrogen peroxide.

E.2.1.1 Elementary Reactions

The elementary reactions of H_2O_2/O_3 process involved in this model are reactions 1-7 and 10-18 in Table E1. The overall reaction for the H_2O_2/O_3 process is:

$$H_2O_2 + 2O_3 \rightarrow 2HO\bullet + 3O_2 \qquad \text{(E-1)}$$

From the reaction above, we can see that 0.5 mole of H_2O_2 is required for each mole of O_3 in order to produce a mole of HO ; or a mass ratio of 0.354 kg of H_2O_2 is needed per kilogram of O_3.

From all of the elementary reactions involved in this model as listed in Table E1, net formation rates of various radicals can be obtained as below:

$$r_{HO\bullet} = k_5[HO_3\bullet] - k_{10}[HO\bullet][HO_2^-] - k_{11}[HO\bullet][H_2O_2] - k_{12}[HO\bullet][HCO_3^-] - k_{13}[HO\bullet][R]$$
$$- k_{14}[HO\bullet][NOM] - k_{15}[HO\bullet][Cl^-] - k_{16}[HO\bullet][CO_3^{2-}] - k_{17}[HO\bullet][Fe^{2+}] - k_{18}[HO\bullet][Mn^{2+}] \quad \text{(E-2)}$$

$$r_{HO_3\bullet} = k_4[O_3^-\bullet][H^+] - k_5[HO_3\bullet] \quad \text{(E-3)}$$

$$r_{O_3^-?} = k_1[O_3][HO_2^-] + k_3[O_2^-\bullet][O_3] - k_4[O_3^-\bullet][H^+] \quad \text{(E-4)}$$

$$r_{HO_2\bullet/O_2\bullet} = k_1[HO_2^-][O_3] + k_{10}[HO\bullet][HO_2^-] + k_{11}[HO\bullet][H_2O_2] - k_3[O_3][O_2^-\bullet] \quad \text{(E-5)}$$

where r_{HO} = net formation rate of hydroxyl radical formation, mole/L•s

$r_{HO3\bullet}$ = net formation rate of ozonide radical formation, mole/L•s

$r_{O3\text{-}\bullet}$ = net formation rate of ozonide ion radical formation, mole/L•s

$r_{HO2\bullet/O2\bullet}$ = total formation rate of superoxide radical formation, mole/L•s

k_{12} = second order rate constant between hydroxyl radical and bicarbonate, L/mole•s

k_{13} = second order rate constant between hydroxyl radical and target organic compound R, L/mole•s

k_{14} = second order rate constant between hydroxyl radical and NOM, L/mole•s

k_{15} = second order rate constant between hydroxyl radical and Cl^-, L/mole•s

k_{16} = second order rate constant between hydroxyl radical and carbonate, L/mole•s

k_{17} = second order rate constant between hydroxyl radical and Fe(II), L/mole•s

k_{18} = second order rate constant between hydroxyl radical and Mn(II), L/mole•s

$[HO_3\bullet]$ = concentration of ozonide radical, mole/L

$[HO\bullet]$ = concentration of hydroxyl radical, mole/L

$[HO_2^-]$ = concentration of conjugate base or anion of hydrogen peroxide, mole/L

$[H_2O_2]$ = concentration of hydrogen peroxide, mole/L

$[HCO_3^-]$ = concentration of bicarbonate, mole/L

[R] = concentration of target organic compound, mole/L

[NOM] = concentration of NOM, mole/L

$[Cl^-]$ = concentration of chloride ion, mole/L

$[CO_3^{2-}]$ = concentration of carbonate, mole/L

$[Fe^{2+}]$ = concentration of two value iron ion, mole/L

$[Mn^{2+}]$ = concentration of two value manganese ion, mole/L

$[O_3^-\bullet]$ = concentration of ozonide ion radical, mole/L

$[H^+]$ = concentration of hydrogen ion, mole/L

$[O_2^-\bullet]$ = concentration of superoxide anion radical, mole/L

$[O_3]$ = concentration of ozone, mole/L

At pseudo–steady state approximation (i.e., all of the net formation rates of radicals (Eq. E-2 to Eq. E-5) are set to be zero), the following expression of the concentration of the hydroxyl radical (Eq. E-6) can be obtained.

$$[HO\bullet]_{ss} = \frac{2k_1[HO_2^-][O_3]}{k_{12}[HCO_3^-]+k_{13}[R]+k_{14}[NOM]+k_{15}[Cl^-]+k_{16}[CO_3^{2-}]+k_{17}[Fe^{2+}]+k_{18}[Mn^{2+}]} \quad \text{(E-6)}$$

where $[HO\bullet]_{ss}$ = pseudo-steady-state concentration of hydroxyl radical, mole/L.

The pseudo–steady state assumption is also invoked for the formation rate of ozone in the liquid phase and the reaction rate of ozone can be written as below:

$$r_{O_3} = k_L a\left(\frac{P_{O_3}}{H_{O_3}} - [O_3]\right) - k_1[HO_2^-][O_3] - k_3[O_2^-\bullet][O_3] = 0 \quad \text{(E-7)}$$

where k_{La} = overall mass transfer coefficient for ozone, s^{-1}

P_{O3} = partial pressure of ozone in inlet gas, atm

H_{O3} = Henry's law constant for ozone, atm·L/mole

Substituting equation E-5 and E-7 into equation E-6, the following expression is obtained:

$$[HO\bullet]_{ss} = \frac{k_L a\left(\frac{P_{O_3}}{H_{O_3}}\right)}{k_{10}[HO_2^-]+k_{11}[H_2O_2]+k_{12}[HCO_3^-]+k_{13}[R]+k_{14}[NOM]+k_{15}[Cl^-]+k_{16}[CO_3^{2-}]+k_{17}[Fe^{2+}]+k_{18}[Mn^{2+}]} \quad \text{(E-8)}$$

The model can be further simplified with the assumption that the concentration of the hydroxyl radical does not change with time and is equal to the initial value expressed as below:

$$[HO\bullet]_{ss,0} = \frac{k_L a\left(\frac{P_{O_3}}{H_{O_3}}\right)}{k_{10}[HO_2^-]_0+k_{11}[H_2O_2]_0+k_{12}[HCO_3^-]_0+k_{13}[R]_0+k_{14}[NOM]_0+k_{15}[Cl^-]_0+k_{16}[CO_3^{2-}]_0+k_{17}[Fe^{2+}]_0+k_{18}[Mn^{2+}]_0} \quad \text{(E-9)}$$

where $[HO\bullet]_{ss,0}$ = initial steady-state concentration of HO•, mole/L

$[HO_2^-]_0$ = initial concentration of conjugate base or anion of hydrogen peroxide, mole/L

$[H_2O_2]_0$ = initial concentration of hydrogen peroxide, mole/L

$[HCO_3^-]_0$ = initial concentration of bicarbonate, mole/L

$[R]_0$ = initial concentration of target organic compound, mole/L

$[NOM]_0$ = initial concentration of NOM, mole/L

$[Cl^-]_0$ = initial concentration of chloride ion, mole/L

$[CO_3^{2-}]_0$ = initial concentration of carbonate, mole/L

$[Fe^{2+}]_0$ = initial concentration of two value iron ion, mole/L

$[Mn^{2+}]_0$ = initial concentration of two value manganese ion, mole/L

Thus, a pseudo–first-order consumption rate law of the target compound can be obtained:

$$r_R = -k_R[R] \quad \text{(E-10)}$$

$$k_R = k_{13}[HO\bullet]_{ss,0} \quad \text{(E-11)}$$

where k_R is the pseudo–first-order reaction rate constant of target compound R, s^{-1}, and k_{13} is the second order rate constant between target compound R and the hydroxyl radical, L/mole•s. This model, termed the simplified pseudo–steady state (Sim-PSS) model, may overestimate the consumption rate of the target compound, because it assumes that the hydroxyl radical concentration is constant and equal to the initial value. For a more comprehensive model of the AOP that does not assume pseudo–steady state or a constant pH, users can refer to the AdOx™ (version 1.0), developed by Crittenden *et al.*(1999).

There is a tool available to calculate the aqueous phase hydroxyl radical reaction rate constant, which is k_{13} in Table E1. Users can refer to the Group Contribution Method developed by Minakata *et al.* (2009). This method can predict a large variety of aqueous phase hydroxyl radical reaction rate constants. A Microsoft Excel spread sheet and a compiled FORTRAN program are given for this purpose. This material is available free of charge via the Internet at http://pubs.acs.org/doi/suppl/10.1021/es900956c.

E.2.1.2 Reactors

Effluent concentration of the target compound can be written from mass balances for the target compound in tanks-in-series (TIS) reactor, completely mixed batch reactor (CMBR), completely mixed flow reactor (CMFR), plug flow reactor (PFR), and dispersed flow reactor (DFR) in a closed system.

$$[R] = \frac{[R]_0}{(1+k_R\frac{\tau}{n})^n} \quad \text{(TIS)} \quad \text{(E-12)}$$

$$[R]=[R]_0 e^{-k_R t} \qquad \text{(CMBR)} \qquad \text{(E-13)}$$

$$[R]=\frac{[R]_0}{(1+k_R\tau)} \qquad \text{(CMFR)} \qquad \text{(E-14)}$$

$$[R]=[R]_0 e^{-k_R \tau} \qquad \text{(PFR)} \qquad \text{(E-15)}$$

$$[R]=\frac{[R]_0 4a\exp(Pe/2)}{(1+a)^2\exp(aPe/2)-(1-a)^2\exp(-aPe/2)} \qquad \text{(DFR)} \qquad \text{(E-16)}$$

$$(a=\sqrt{1+4k_R\tau/\mathrm{Pe}})$$

where $[R]_0$ is the influent concentration of the target compound, [R] is the effluent concentration of the target compound, τ is the hydraulic retention time of the reactor, k_R is the pseudo–first-order reaction rate constant of the target compound, n is the number of tanks for TIS, and Pe is the Peclet number for DFR.

E.2.1.3 Energy Efficiency per Removal of Order

The energy efficiency per removal of order (EE/O) values of the batch system (i.e., CMBR) and the flow system (i.e., TIS, CMFR, PFR, DFR) can be calculated from the equations below, respectively.

For batch system

$$EE/O = \frac{\frac{k_L a \frac{P_{O_3}}{H_{O_3}}}{\eta} V \times \frac{10^3 \text{ liter}}{\text{meter}^3} \times \frac{0.0022 \text{ lb}}{\text{gram}} \times E_{O3} \times \frac{60 \text{ seconds}}{\text{minutes}} + C_{H2O2} \times \frac{0.0022 \text{ lb}}{\text{gram}}}{V \log\left(\frac{C_i}{C_f}\right)} \qquad \text{(E-17)}$$

where k_{La} = overall mass transfer coefficient for ozone, s^{-1}

P_{O3} = partial pressure of ozone in inlet gas, atm

H_{O3} = Henry's law constant for ozone, atm·L/mole

V = reactor volume, m^3

M_{O3} = molecular weight of ozone, g/mole

E_{O3} = energy use to produce O_3, kWh/lb

t = reaction time for batch reactor, minute

η = transfer efficiency of ozone contactor , dimensionless

C_{H2O2} = total concentration of H_2O_2 added into the reactor, mg/L

E_{H2O2} = energy use to produce H_2O_2, kWh/lb;

C_i = influent concentration of the target compound, mg/L

C_f = effluent concentration of the target compound, mg/L

For flow system

$$EE/O = \frac{\dfrac{k_L a \left(\dfrac{P_{O_3}}{H_{O_3}}\right) V \times \dfrac{10^3 \text{ liter}}{\text{meter}} \times M_{O_3} \times \dfrac{0.0022 \text{ lb}}{\text{gram}}}{\eta} + C_{H2O2} \times \dfrac{0.0022 \text{ lb}}{\text{gram}}}{Q \log\left(\dfrac{C_i}{C_f}\right)} \qquad \text{(E-18)}$$

where Q = flow rate of the reactor, m^3/s

E.2.2 H_2O_2 Added after O_3 Addition Model

There is occasion where gaseous ozone is injected at first place and solely ozonation takes place for obtaining Ct disinfection credits and then hydrogen peroxide is added for the destruction of target organic compound. The waste water will continuously flow through an ozone contactor for disinfection and a H_2O_2/O_3 reactor for the degradation of target compound. In this model, we only simulate the H_2O_2/O_3 reactor,

where hydrogen peroxide is added to water that has a certain concentration of ozone (i.e., $[O_3]_{res}$).

E.2.2.1 Elementary Reactions

The elementary reactions involved, the formation rates of radicals and the calculation process of the concentration of the hydroxyl radical are the same with the simplified pseudo-steady state H_2O_2/O_3 model. The steady state hydroxyl radical concentration is given by the following equation using $[O_3]_{res}$:

$$[HO\bullet]_{ss} = \frac{2k_1[HO_2^-][O_3]_{res}}{k_{12}[HCO_3^-]+k_{13}[R]+k_{14}[NOM]+k_{15}[Cl^-]+k_{16}[CO_3^{2-}]+k_{17}[Fe^{2+}]+k_{18}[Mn^{2+}]} \quad \text{(E-19)}$$

The model can be further simplified with the assumption that the concentration of the hydroxyl radical does not change with time and is equal to the initial value, expressed as below:

$$[HO\bullet]_{ss,0} = \frac{2k_1[HO_2^-]_0[O_3]_{res}}{k_{12}[HCO_3^-]_0+k_{13}[R]_0+k_{14}[NOM]_0+k_{15}[Cl^-]_0+k_{16}[CO_3^{2-}]_0+k_{17}[Fe^{2+}]_0+k_{18}[Mn^{2+}]_0} \quad \text{(E-20)}$$

Thus a pseudo–first-order reaction rate of the target compound can be same as in equations (E-10) and (E-11), respectively.

E.2.2.2 Reactors

The mass balance equations for the target compound in various types of reactors are the same with the simplified pseudo-steady state H_2O_2/O_3 model. The process where hydrogen peroxide is added in the presence of dissolved ozone is for particularly flow reactors, and therefore, we only consider flow system (i.e., CMFR, TIS, PFR, and DIS) for this process.

E.2.2.3 Energy Efficiency per Removal of Order

As mentioned above, we only consider flow system for the EE/O calculations. The EE/O value for the flow system can be calculated by

$$EE/O = \frac{\dfrac{Q_{O3} \times \dfrac{0.0022\ lb}{gram} \times E_{O3}}{\eta} + Q_{H2O2} \times \dfrac{0.0022\ lb}{gram} \times E_{H2O2}}{Q \log\left(\dfrac{C_i}{C_f}\right)} \quad \text{(E-21)}$$

where Q = flow rate of the reactor, m^3/s

C_{O3} = concentration of ozone in liquid phase, mg/L

E_{O3} = energy use to produce O_3, kWh/lb

η = transfer efficiency of the ozone contactor, dimensionless

C_{H2O2} = total concentration of H_2O_2 added into the reactor, mg/L

E_{H2O2} = energy use to produce H_2O_2, kWh/lb

C_i = influent concentration of the target compound, mg/L

C_f = effluent concentration of the target compound, mg/L

E.2.3 Ultraviolet with Hydrogen Peroxide Model

The H_2O_2/UV is a process in which hydrogen peroxide is injected into a reactor equipped with UV light. The photolysis of hydrogen peroxide will produce hydroxyl radical that can degrade target compounds.

E.2.3.1 Elementary Reactions

The elementary reactions of the H_2O_2/UV process involved in this model are reactions 8-18 in Table E1. From the elementary reactions involved in this model, the net formation rate of the hydroxyl radical can be obtained as below:

$$r_{HO\bullet} = 2\Phi_{H_2O_2} P_{U\text{-}V} f_{H_2O_2} - k_{10}[HO\bullet][HO_2^-] - k_{11}[HO\bullet][H_2O_2] - k_{12}[HO\bullet][HCO_3^-] - k_{13}[HO\bullet][R] - k_{14}[HO\bullet][NOM] - k_{15}[HO\bullet][Cl^-] - k_{16}[HO\bullet][CO_3^{2-}] - k_{17}[HO\bullet][Fe^{2+}] - k_{18}[HO\bullet][Mn^{2+}] \quad \text{(E-22)}$$

where $r_{HO\bullet}$ = net formation rate of hydroxyl radical, mole/L•s

Φ_{H2O2} = quantum yield of hydrogen peroxide, mole/einstein

$P_{U\text{-}V}$= UV light intensity at wavelength λ, einstein/(L•s)

f_{H2O2} = fraction of light absorbed by hydrogen peroxide, dimensionless

A = absorbance, dimensionless

k_{10} = second order rate constant between hydroxyl radical and anion of hydrogen peroxide, L/mole•s

k_{11} = second order rate constant between hydroxyl radical and hydrogen peroxide, L/mole•s

k_{12} = second order rate constant between hydroxyl radical and bicarbonate, L/mole•s

k_{13} = second order rate constant between hydroxyl radical and target organic compound R, L/mole•s

k_{14} = second order rate constant between hydroxyl radical and NOM, L/mole•s

k_{15} = second order rate constant between hydroxyl radical and chloride ion, L/mole•s

k_{16} = second order rate constant between hydroxyl radical and carbonate, L/mole•s

k_{17} = second order rate constant between hydroxyl radical and Fe(II), L/mole•s

k_{18} = second order rate constant between hydroxyl radical and Mn(II), L/mole•s

[HO•] = concentration of hydroxyl radical, mole/L

$[HO_2^-]$ = concentration of anion of hydrogen peroxide, mole/L

$[H_2O_2]$ = concentration of hydrogen peroxide, mole/L

$[HCO_3^-]$ = concentration of bicarbonate, mole/L

[R] = concentration of target compound R, mole/L

[NOM] = concentration of NOM, mole carbon/L

$[Cl^-]$ = concentration of chloride ion, mole/L

$[CO_3^{2-}]$ = concentration of carbonate, mole/L

$[Fe^{2+}]$ = concentration of Fe^{2+}, mole/L

$[Mn^{2+}]$ = concentration of Mn^{2+}, mole/L

After invoking the pseudo–steady state approximation, steady-state hydroxyl radical concentration is:

$$[HO\bullet]_{ss} = \frac{2\Phi_{H_2O_2} P_{U\text{-}V} f_{H_2O_2}}{k_{10}[HO_2^-] + k_{11}[H_2O_2] + k_{12}[HCO_3^-] + k_{13}[R] + k_{14}[NOM] + k_{15}[Cl^-] + k_{16}[CO_3^{2-}] + k_{17}[Fe^{2+}] + k_{18}[Mn^{2+}]} \quad \text{(E-23)}$$

This model can be further simplified with the assumption that the concentration of the hydroxyl radical does not change with time and is equal to the initial value expressed as below:

$$[HO\bullet]_{ss,0} = \frac{2\Phi_{H_2O_2} P_{U\text{-}V} f_{H_2O_2}}{k_{10}[HO_2^-]_0 + k_{11}[H_2O_2]_0 + k_{12}[HCO_3^-]_0 + k_{13}[R]_0 + k_{14}[NOM]_0 + k_{15}[Cl^-]_0 + k_{16}[CO_3^{2-}]_0 + k_{17}[Fe^{2+}]_0 + k_{18}[Mn^{2+}]_0} \quad \text{(E-24)}$$

where $[HO\bullet]_{ss,0}$ = initial pseudo–steady state concentration of hydroxyl radical, mole/L

$[H_2O_2]_0$ = initial concentration of hydrogen peroxide, mole/L

$[HCO_3^-]_0$ = initial concentration of bicarbonate, mole/L

$[R]_0$ = initial concentration of target compound R, mole/L

$[NOM]_0$ = initial concentration of NOM, mole/L

$[Cl^-]_0$ = initial concentration of chloride ion, mole/L

$[CO_3^{2-}]_0$ = initial concentration of carbonate, mole/L

$[Fe^{2+}]_0$ = initial concentration of Fe^{2+}, mole/L

$[Mn^{2+}]_0$ = initial concentration of Mn^{2+}, mole/L

The photolysis of the target compound can be neglected because of the low reaction rate. Thus a pseudo–first-order reaction rate of the target compound can be same as in equations (E-10) and (E-11), respectively.

E.2.3.2 Reactors

The mass balance equations for the target compound in various reactors are the same with the simplified pseudo-steady state H_2O_2/O_3 model. The effluent concentrations of target compound can be estimated using equations from (E-12) to (E-16) for reactor types of TIS, CMBR, CMFR, PFR, and DFR, respectively.

E.2.3.3 Energy Efficiency per Removal of Order

The EE/O values of the flow system and the batch system can be calculated by

$$EE/O = \frac{P + Q \times \frac{3600\ \text{seconds}}{\text{hours}} \times [H_2O_2] \times \frac{0.0022\ \text{lb}}{\text{gram}} \times E_{H_2O_2}}{Q \times \frac{3600\ \text{seconds}}{\text{hours}} \times \log\left(\frac{C_i}{C_f}\right)} \quad \text{(For flow system)} \quad \text{(E-25)}$$

$$EE/O = \frac{P \times \frac{1\ \text{hour}}{60\ \text{minutes}} + V \times [H_2O_2] \times \frac{0.0022\ \text{lb}}{\text{gram}} \times E_{H_2O_2}}{V \times \log\left(\frac{C_i}{C_f}\right)} \quad \text{(For batch system)} \quad \text{(E-26)}$$

where P = total lamp power, kW

Q = flow rate of the reactor, m^3/s

C_{H2O2} = total concentration of H_2O_2 added into the reactor, mg/L

E_{H2O2} = energy use to produce H_2O_2, kWh/lb

V = reactor volume, m^3

t = reaction time for the batch system, min

C_i = influent concentration of the target compound, mg/L

C_f = effluent concentration of the target compound, mg/L

E.2.4 Ozone Rc Model

During ozonation, hydroxyl radical will be produced when aqueous phase ozone reacts with NOM. Since hydroxyl radical is a highly reactive oxidant for degradation of target compound, the target compound will be degraded by two ways: direct reacting with ozone and reacting with hydroxyl radical produced by ozone and NOM. It is important to simulate both degradation pathways for the purpose of adequate prediction of degradation and optimization of the process.

E.2.4.1 Elementary Reactions

The destruction rate of the target compound can be expressed as below:

$$r_R = -k_{O3}[R][O_3] - k_{HO\bullet}[HO\bullet][R] \qquad \text{(E-27)}$$

where r_R = rate of disappearance of the target compound R, mole/L ·s

$[O_3]$ = concentration of ozone in aqueous phase, mole/L

[R] = concentration of target compound R, mole/L

[HO ·] = concentration of hydroxyl radical, mole/L

$k_{HO\cdot}$ = second order rate constants between hydroxyl radical and target compound, L/mole ·s

k_{O3}= second order rate constants between ozone and target compound, L/ mole ·s

It is reported that the ratio of the concentration of the hydroxyl radical to the concentration of ozone in aqueous phase, termed as R_c (=[HO•]/[O_3]), is relatively constant (10^{-7}-10^{-9}) during the decomposition process in the presence of NOM (Elovitz and von Gunten, 1999).

The loss of ozone and the decomposition of the target compound can be described by pseudo–first-order reaction and second order reaction, respectively:

$$r_{O_3} = -k[O_3] \tag{E-28}$$

$$r_R = -(k_{O_3} + k_{HO\bullet} R_c)[O_3][R] \tag{E-29}$$

where r_{O3} = rate of loss of ozone in aqueous phase, mole/L·s

k = pseudo-first-order rate constant for ozone, s^{-1}

r_R = rate of disappearance of target compound R, mole/L·s

R_c = ratio of hydroxyl radical concentration to aqueous phase ozone concentration, dimensionless

$k_{HO\cdot}$ = second order rate constants between hydroxyl radical and target compound, L/mole·s

k_{O3} = second order rate constants between ozone and target compound, L/mole·s

E.2.4.2 Reactors

The mass balance equations for ozone and target compound in various reactors are the same with the simplified pseudo-steady state H_2O_2/O_3 model. The effluent concentrations of target compound can be estimated using equations from (E-12) to (E-16) for reactor types of TIS, CMBR, CMFR, PFR, and DFR, respectively.

E.2.4.3 Energy Efficiency per Removal of Order

The EE/O values of the batch system and the flow system can be calculated by

$$EE/O = \frac{Q_{O3} \times \frac{0.0022\ lb}{gram} E_{O3}}{\eta \times Q \log\left(\frac{C_i}{C_f}\right)} \quad \text{(For flow system)} \quad \text{(E-30)}$$

$$EE/O = \frac{V_{O3} \times \frac{0.0022\ lb}{gram} E_{O3}}{\eta \times V \log\left(\frac{C_i}{C_f}\right)} \quad \text{(For batch system)} \quad \text{(E-31)}$$

where Q = flow rate of the liquid stream of the reactor for flow system, m^3/s

V = volume of the reactor, m^3

C_{O3} = ozone concentration in the liquid phase, mg/L

E_{O3} = energy use to produce O_3, kWh/lb

η = transfer efficiency of the ozone contactor, dimensionless

C_i = influent concentration of the target compound, mg/L

C_f = effluent concentration of the target compound, mg/L

E.3 Pseudo-Steady State Model

In this module, the pseudo-steady state models include: 1) H_2O_2/O_3 model; 2) H_2O_2 added after O_3 addition model; 3) UV/H_2O_2 model; and 4) O_3 - R_c model. The reactor types include: 1) completely mixed batch reactor (CMBR); 2) completely mixed flow reactor (CMFR); and 3) plug flow reactor (PFR). The elementary reactions involved in the pseudo-steady state models are the same with the simplified pseudo-steady state models as listed in Table E1.

E.3.1 Ozone with Hydrogen Peroxide Model

E.3.1.1 Elementary Reactions

The elemental reactions of H_2O_2/O_3 process involved in this model are the same with the simplified pseudo-steady state H_2O_2/O_3 model. From all of the elementary reactions involved, net formation rates of main species, including H_2O_2/HO_2^-, R, NOM, Fe^{2+}, Mn^{2+}, Cl^-, HCO_3^-/CO_3^{2-}, O_3, can be obtained as below:

$$\frac{d[H_2O_2/HO_2^-]}{dt} = -k_1[HO_2^-][O_3]-k_{10}[HO\bullet][HO_2^-]- k_{11}[HO\bullet][H_2O_2] \quad \text{(E-32)}$$

$$\frac{d[R]}{dt} = - k_9[HO\bullet][R] \quad \text{(E-33)}$$

$$\frac{d[NOM]}{dt} = - k_{14}[HO\bullet][NOM] \quad \text{(E-34)}$$

$$\frac{d[Fe^{2+}]}{dt} = - k_{17}[HO\bullet][Fe^{2+}] \quad \text{(E-35)}$$

$$\frac{d[Mn^{2+}]}{dt} = - k_{18}[HO\bullet][Mn^{2+}] \quad \text{(E-36)}$$

$$\frac{d[Cl^-]}{dt} = - k_{15}[HO\bullet][Cl^-] \quad \text{(E-37)}$$

$$\frac{d[HCO_3^-/CO_3^{2-}]}{dt} = -k_{12}[HO\bullet][HCO_3^-]-k_{16}[HO\bullet][CO_3^{2-}] \quad \text{(E-38)}$$

$$\frac{d[O_3]}{dt} = k_L a\left(\frac{P_{O_3}}{H}-[O_3]\right)-k_1[HO_2^-][O_3]-k_3[O_2^-\bullet][O_3] \quad \text{(E-39)}$$

The net formation rates of radicals, including HO•, HO_3•, O_3^-•, and O_2^-•, are the same with simplified pseudo-steady state H_2O_2/O_3 model and can be calculated with the equations from (E-2) to (E-5), respectively.

The following equilibrium relationships are considered:

$$[HCO_3^-] = \frac{K_{a1}[H_2CO_3^*]}{[H^+]} \quad \text{(E-40)}$$

$$[CO_3^{2-}] = \frac{K_{a2}[HCO_3^-]}{[H^+]} \quad \text{(E-41)}$$

$$[HO_2^-] = \frac{K_{a3}[H_2O_2]}{[H^+]} \quad \text{(E-42)}$$

The following expressions of radical concentrations are obtained once the pseudo–steady state approximation is applied to all radical intermediates, which means all of the net formation rates of radicals are set to be zero.

$$[HO\bullet]_{ss} = \frac{k_5[HO_3\bullet]}{k_{10}[HO_2^-]+k_{11}[H_2O_2]+k_{12}[HCO_3^-]+k_{13}[R]+k_{14}[NOM]+k_{15}[Cl^-]+k_{16}[CO_3^{2-}]+k_{17}[Fe^{2+}]+k_{18}[Mn^{2+}]} \quad \text{(E-43)}$$

$$[HO_3\bullet]_{ss} = \frac{k_4[O_3^-\bullet][H^+]}{k_5} \quad \text{(E-44)}$$

$$[O_3^-\bullet]_{ss} = \frac{k_1[HO_2^-][O_3]+k_3[O_2^-\bullet][O_3]}{k_4[H^+]} \quad \text{(E-45)}$$

$$[O_2^-\bullet]_{ss} = \frac{k_1[HO_2^-][O_3]+k_{10}[HO\bullet][HO_2^-]+k_{11}[HO\bullet][H_2O_2]}{k_3[O_3]} \quad \text{(E-46)}$$

E.3.1.2 Reactors

Pseudo-steady state H_2O_2/O_3 model considers following reactors: 1) completely mixed batch reactor (CMBR), 2) completely mixed flow reactor (CMFR), and 3) plug flow reactor (PFR). The mass balance equations for all of these reactors are listed as below:

$$\frac{dC_a}{dt} = r_a \qquad \text{(CMBR)} \qquad \text{(E-47)}$$

$$\frac{dC_a}{dt} = \frac{1}{\tau}(C_{ao}\text{-}C_a)+r_a \qquad \text{(CMFR)} \qquad \text{(E-48)}$$

$$\frac{dC_a}{d\tau} = r_a \qquad \text{(PFR)} \qquad \text{(E-49)}$$

where C_{ao} is the influent concentration of species A; C_a is the concentration of A at time t; t is the reaction time; τ is the hydraulic retention time; and r_a is the net formation rate of the species A. The ordinary differential equations (ODEs) resulting from the substitution of net formation rates of main species and concentrations of radicals into the mass balances equations are solved by 4th-order Runge-Kutta method.

E.3.1.3 Energy Efficiency per Removal of Order

The calculation of the EE/O values for both flow systems and batch systems are the same with the simplified pseudo-steady state H_2O_2/O_3 model.

E.3.2 H_2O_2 Added after O_3 Addition Model

E.3.2.1 Elementary Reactions

The elementary reactions and development processes of pseudo-steady state H_2O_2 added after O_3 addition model are the same with pseudo-steady state H_2O_2/O_3 model except that the net formation rate of aqueous phase O_3 doesn't include mass transfer process of O_3 from gas phase to aqueous phase, which is expressed as below:

$$\frac{d[O_3]}{dt} = -k_1[HO_2^-][O_3]-k_3[O_2^-\bullet][O_3] \qquad \text{(E-50)}$$

E.3.2.2 Reactors

The process where hydrogen peroxide is added in the presence of dissolved ozone is for particularly flow reactors, and therefore, we only consider CMFR and PFR for this process. The mass balance equations for main species in various reactors are the same with the pseudo-steady state H_2O_2/O_3 model. The ordinary differential equations (ODEs) resulting from the substitution of formation rates of main species and concentrations of radicals into the mass balances equations are solved by 4th-oder Runge-Kutta method.

E.3.2.3 Energy Efficiency per Removal of Order

The calculations of the EE/O values for flow system are the same with the simplified pseudo-steady state H_2O_2 added after O_3 addition model.

E.3.3 Ultraviolet with Hydrogen Peroxide Model

E.3.3.1 Elementary Reactions

The elementary reactions of H_2O_2/UV process involved in this model are the same with the simplified pseudo-steady state H_2O_2/UV model. From all of the elementary reactions involved, the net formation rates of main species, including H_2O_2/HO_2^-, R, NOM, Fe^{2+}, Mn^{2+}, Cl^-, HCO_3^-/CO_3^{2-} , can be obtained as below:

$$\frac{d[H_2O_2/HO_2^-]}{dt} = -\Phi P_{U\text{-}V} f(1-e^{-A}) - k_{10}[HO\bullet][HO_2^-] - k_{11}[HO\bullet][H_2O_2] \quad \text{(E-51)}$$

$$\frac{d[R]}{dt} = -k_{13}[HO\bullet][R] \quad \text{(E-52)}$$

$$\frac{d[NOM]}{dt} = -k_{14}[HO\bullet][NOM] \quad \text{(E-53)}$$

$$\frac{d[Fe^{2+}]}{dt} = -k_{17}[HO\bullet][Fe^{2+}] \quad \text{(E-54)}$$

$$\frac{d[Mn^{2+}]}{dt} = - k_{18}[HO\bullet][Mn^{2+}] \quad \text{(E-55)}$$

$$\frac{d[Cl^-]}{dt} = - k_{15}[HO\bullet][Cl^-] \quad \text{(E-56)}$$

$$\frac{d[HCO_3^-/CO_3^{2-}]}{dt} = -k_{12}[HO\bullet][HCO_3^-] - k_{16}[HO\bullet][CO_3^{2-}] \quad \text{(E-57)}$$

The net formation rate of HO• is the same with simplified pseudo-steady state H_2O_2/UV model, which can be found in (E-24). The following equilibrium relationships are considered:

$$[HCO_3^-] = \frac{K_{a1}[H_2CO_3^*]}{[H^+]} \quad \text{(E-58)}$$

$$[CO_3^{2-}] = \frac{K_{a2}[HCO_3^-]}{[H^+]} \quad \text{(E-59)}$$

$$[HO_2^-] = \frac{K_{a3}[H_2O_2]}{[H^+]} \quad \text{(E-60)}$$

The following expressions of steady state HO• concentrations is obtained once the pseudo–steady state approximation is applied, which means the net formation rate of HO• is set to be zero.

$$[HO\bullet]_{ss} = \frac{2\Phi P_{U\text{-}V} f(1-e^{-A})}{k_{10}[HO_2^-]+k_{11}[H_2O_2]+k_{12}[HCO_3^-]+k_{13}[R]+k_{14}[NOM]+k_{15}[Cl^-]+k_{16}[CO_3^{2-}]+k_{17}[Fe^{2+}]+k_{18}[Mn^{2+}]} \quad \text{(E-61)}$$

E.3.3.2 Reactors

The mass balance equations for main species in various reactors are the same with the pseudo-steady state H_2O_2/O_3 model. The ordinary differential equations (ODEs)

resulting from the substitution of formation rates of main species and concentrations of radicals into the mass balances equations are solved by 4th-oder Runge-Kutta method.

E.3.3.3 Energy Efficiency per Removal of Order

The calculation of EE/O value for both flow systems and batch systems are the same with the simplified pseudo-steady state H_2O_2/UV model.

E.3.4 Ozone R_c model

E.3.4.1 Elementary Reactions

The elementary reactions in this model are the same with the simplified pseudo-steady state O_3 R_c model. The net formation rates of main species, including O_3, R, NOM, Fe^{2+}, Mn^{2+}, Cl^-, HCO_3^-/CO_3^{2-}, can be obtained:

$$\frac{d[O_3]}{dt} = -k[O_3] \quad \text{(E-62)}$$

$$\frac{d[R]}{dt} = -(k_{O_3} + k_{13}R_c)[O_3][R] \quad \text{(E-63)}$$

$$\frac{d[NOM]}{dt} = -k_{14}R_c[O_3][NOM] \quad \text{(E-64)}$$

$$\frac{d[Fe^{2+}]}{dt} = -k_{17}R_c[O_3][Fe^{2+}] \quad \text{(E-65)}$$

$$\frac{d[Mn^{2+}]}{dt} = -k_{18}R_c[O_3][Mn^{2+}] \quad \text{(E-66)}$$

$$\frac{d[Cl^-]}{dt} = -k_{15}R_c[O_3][Cl^-] \quad \text{(E-67)}$$

$$\frac{d[HCO_3^-/CO_3^{2-}]}{dt} = -k_{12}R_c[O_3][HCO_3^-] - k_{16}R_c[O_3][CO_3^{2-}] \quad \text{(E-68)}$$

E.3.4.2 Reactors

The mass balance equations for ozone and main species in various reactors are the same with the pseudo-steady state H_2O_2/O_3 model. The ordinary differential equations (ODEs) resulting from the substitution of formation rates of main species into the mass balances equations are solved by 4^{th}-order Runge-Kutta method.

E.3.4.3 Energy Efficiency per Removal of Order

The calculation of EE/O value for both flow systems and batch systems are the same with the simplified pseudo-steady state O_3 R_c model.

E.4 Instruction for Microsoft Excel Spread Sheet

This part gives an instruction of the supplemental Microsoft Excel spread sheet associated with the simplified pseudo-steady state models.

E.4.1 Input Data

To run a simulation, some properties or operational parameters should be directly entered into the appropriate places. The following discussion will elaborate on how to enter the parameters and the information necessary for a model simulation run.

There are three steps for entering inputs: (1) entering general inputs in general input column on the "Input Page", (2) choosing one kind of model and entering relative parameters for a specific model type in corresponding column on the "Input Page", (3) choosing one type of reactor and entering relative parameters for a specific reactor type in corresponding page following the "Input Page".

E.4.1.1 Inputs for All Types of Reactors

This part has five columns divided by general inputs and inputs for different kinds of models applied.

(1) General inputs for four models

This column contains background parameters and properties which can be used by all of the four models. The general inputs include alkalinity, DOC, the reaction rate constant of DOC with the hydroxyl radical, the concentration of chloride ion, the concentration of Fe(II), the concentration of Mn(II), pH, the concentration of the target compound, the molecular weight of the target compound, the HO · reaction rate constant with the target compound, the total reactor volume, and the flow rate of the reactor (this input can be neglected when users use completely mixed batch reactor(CMBR)).

General Inputs For Four Models	
pH	7.5
Concentration of target compound, mg/L	0.1
Molecular weight of target compound, g/mole	131
$k_{HO\cdot}$ with target compound, $M^{-1}s^{-1}$ *(See *GCM)*	4.20E+09
Concentration of chloride ion, mg/L	2.00
Concentration of iron ion (II), mg/L	0.05
Concentration of manganese ion (II), mg/L	0.10
Alkalinity, mg/L as $CaCO_3$	400
DOC, mg/L	0.7
$k_{HO\cdot}$ with DOC, $M^{-1}s^{-1}$	3.90E+08
Total reactor volume, m^3	10
Flow rate, m^3/s (Can be neglected when using CMBR)	0.025

Figure E.1. General inputs of simplified pseudo-steady state models.

(2) Inputs for H_2O_2/O_3 model

When using the H_2O_2/O_3 model, you should enter the total H_2O_2 dosage, the overall mass transfer coefficient for O_3, the partial pressure of ozone, the energy use for O_3 production, the energy use for H_2O_2 production, and the transfer efficiency of ozone contactor, apart from entering the general inputs.

Inputs For H_2O_2/O_3 Model	
Total H_2O_2 dosage, mg/L	1
Overall mass transfer coefficient for O_3, s^{-1}	0.00060
Partial pressure of ozone, atm	0.07
Energy use for O_3 production, kWh/lb	5
Transfer efficiency of ozone contactor	0.8
Energy use for H_2O_2 production, kWh/lb	4.9

Figure E.2. Inputs for H_2O_2/O_3 model.

(3) Inputs for H_2O_2 added after O_3 addition model

For this model, you should specify the total H_2O_2 dosage, the initial ozone concentration at the point of H_2O_2 addition, the transfer efficiency of ozone contactor, the energy use for O_3 production, and the energy use for H_2O_2 production.

Inputs For H_2O_2 Added After O_3 Addition Model	
Total H2O2 dosage, mg/L	1.4
Initial ozone concentration at the point of H_2O_2 addition, mg/L	5.5
Transfer efficiency of ozone contactor	0.8
Energy use for O_3 production, kWh/lb	5
Energy use for H_2O_2 production, kWh/lb	4.9

Figure E.3. Inputs for H_2O_2 added after O_3 addition model.

(4) Inputs for H_2O_2/UV model

For this kind of model, you should specify the total H_2O_2 dosage, the wavelength of light used in this model, the number of lamps, the lamp power, the lamp efficiency, the

energy use for H_2O_2 production and the absorbance of NOM at 254 nm for a cell path length of 1 cm.

Inputs For H_2O_2/UV Model	
Total H_2O_2 dosage, mg/L	85
Wavelength of light, nm	254
Number of lamps	12
Lamp power, kW	15
Electronical efficiency	0.2
Energy use for H_2O_2 production, kWh/lb	4.9
Absorbance of NOM at 254 nm for a cell path length of 1 cm	0.300

Figure E.4. Inputs for H_2O_2/UV model.

(5) Inputs for O_3 R_c model

For this kind of model, you should specify the initial ozone concentration, the second order reaction rate constant between ozone and the target compound (which can be ignored for the most part because the direct oxidation of ozone is usually negligible as compared to hydroxyl radical), the R_c value, the ozone pseudo–first-order reaction rate constant, the transfer efficiency of ozone contactor, the energy use for ozone production.

Inputs For O_3 R_c Model	
Initial ozone concentration, mg/L	1.3
k_{O3} with target compound, $M^{-1}s^{-1}$	17
R_c(=[HO•]/[O_3])	1.00E-07
Ozone pseudo-first-order reactioin rate constant, min^{-1}	0.1
Transfer efficiency of ozone contactor	0.8
Energy use for O_3 production, kWh/lb	5

Figure E.5. Inputs for O_3 R_c model.

E.4.1.2 Inputs for Specific Reactors

This spread sheet contains five kinds of reactors: completely mixed batch reactor (CMBR), plug flow reactor (PFR), completely mixed flow reactor (CMFR) as ideal

reactors and tanks in series (TIS) reactor, dispersed flow reactor (DFR) in closed systems as non-ideal reactors. You should enter reactor parameters in the corresponding pages following the "Input Page."

For the CMBR, you should specify the reaction time for CMBR on the "CMBR Page".

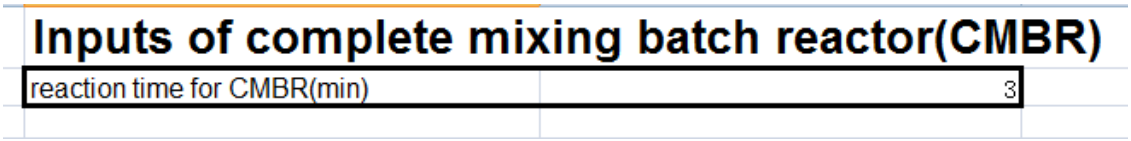

Figure E.6. Input for CMBR.

For the TIS reactor, you should specify the number of completely mixed flow reactors on the "TIS Page".

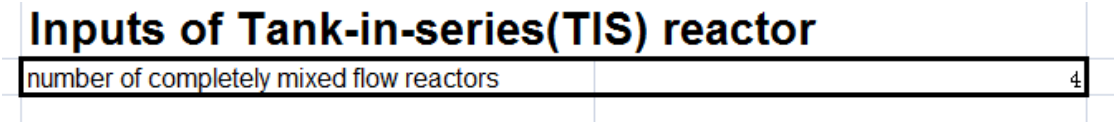

Figure E.7. Input for TIS.

For the DFR reactor, you should specify the Peclet number on the "DFR Page".

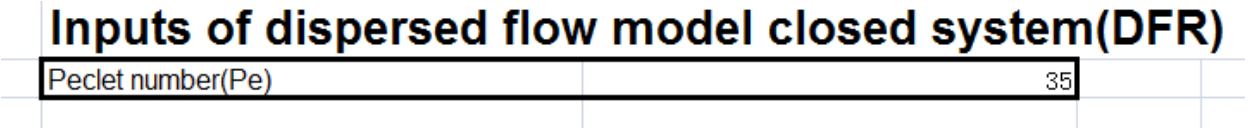

Figure E.8. Input for DFR.

E.4.2 Output Data

The output data of each kind of reactor can be found on the corresponding page, which contains the effluent concentrations of the target compound and EE/O values for all four models.

Outputs of Tanks-in-series (TIS) Reactor

Types of models	Effluent concentration of target compound, mg/L	EE/O, kWh/m^3 . order of removal	EE/O, kWh/kgal . order of removal
H_2O_2/O_3 model	0.057	0.165	0.624
H_2O_2 added after O_3 addition model	0.091	0.263	0.997
H_2O_2/UV model	0.010	0.601	2.275
O_3 R_c model	0.041	0.026	0.098

Figure E.9. Outputs for TIS.

E.5 Instruction for MathCAD Files

This part gives an instruction of the supplemental MathCAD files associated with the pseudo-steady state models.

E.5.1 Input Data

To run a simulation, some properties or operational parameters should be directly entered in the appropriate places. The following discussion will elaborate on how to enter the parameters and information necessary for a model simulation run.

There are four steps for entering inputs: (1) choosing one kind of model and opening relative MathCAD file, (2) entering general inputs in the general inputs column, (3) entering inputs specific to the chosen model in the corresponding model column, (4) choosing one type of reactor and entering relative parameters in the corresponding reactor column.

E.5.1.1 General Inputs for Four Models

This column contains background parameters and properties which can be used by all of the four models. The general inputs include alkalinity, DOC, reaction rate constant of DOC with hydroxyl radical, concentration of chloride ion, concentration of Fe(II), concentration of Mn(II), pH, concentration of target compound, molecular weight

of target compound, HO · reaction rate constant with target compound, and total reactor volume.

General Inputs:

pH	pH := 7.5
Concentration of target compound, mg/L	ρ := 0.2
Molecular weight of target compound, g/mole	M := 131.389
$k_{HO\cdot}$ with target compound, $M^{-1}S^{-1}$	k9 := 4.2 · 10^{9}
*(see *GCM)*	
Concentration of chloride ion, mg/L	Clm := 35.5 · 10^{-3}
Concentration of Fe(II), mg/L	Fem := 56 · 10^{-3}
Concentration of Mn(II), mg/L	Mnm := 55 · 10^{-3}
Alkalinity, mg/L as $CaCO_3$	Alk := 400
DOC, mg/L	DOC := 0.7
$k_{HO\cdot}$ with DOC, $M^{-1}s^{-1}$	k10 := 3.9 · 10^{8}
Total reactor volume, m^3	v := 5.5

Figure E.10. General Inputs of pseudo-steady state models.

E.5.1.2 Inputs for H_2O_2/O_3 Model

When using the H_2O_2/O_3 model, you should enter the total H_2O_2 dosage, overall mass transfer coefficient for O_3, partial pressure of ozone, energy use for O_3 production, energy use for H_2O_2 production, and transfer efficiency of ozone contactor, apart from entering the general inputs.

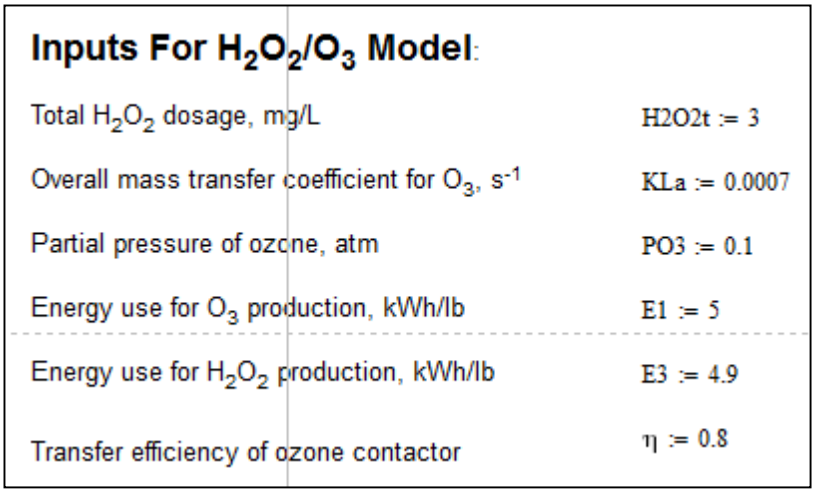

Figure E.11. Inputs for H_2O_2/O_3 model.

E.5.1.3 Inputs for H_2O_2 Added after O_3 Addition Model

When using the H_2O_2 added after O_3 addition model, you should specify the total H_2O_2 dosage, the initial ozone concentration at the point of H_2O_2 addition, the transfer efficiency of ozone contactor, the energy use for O_3 production, and the energy use for H_2O_2 production.

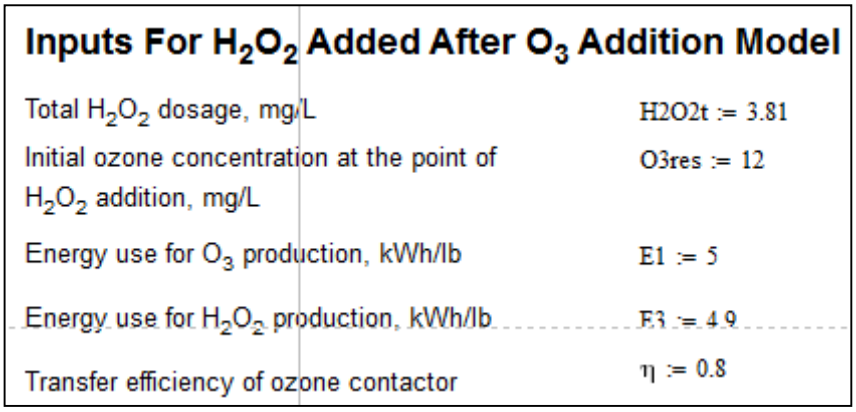

Figure E.12. Inputs for H_2O_2 added after O_3 addition model.

E.5.1.4 Inputs for H_2O_2/UV Model

When using the H_2O_2/UV model, you should specify the wavelength of light used in this model, the number of lamps, the lamp power, the lamp efficiency, the absorbance of NOM at 254 nm for a cell path length of 1cm, and the energy use for H_2O_2 production.

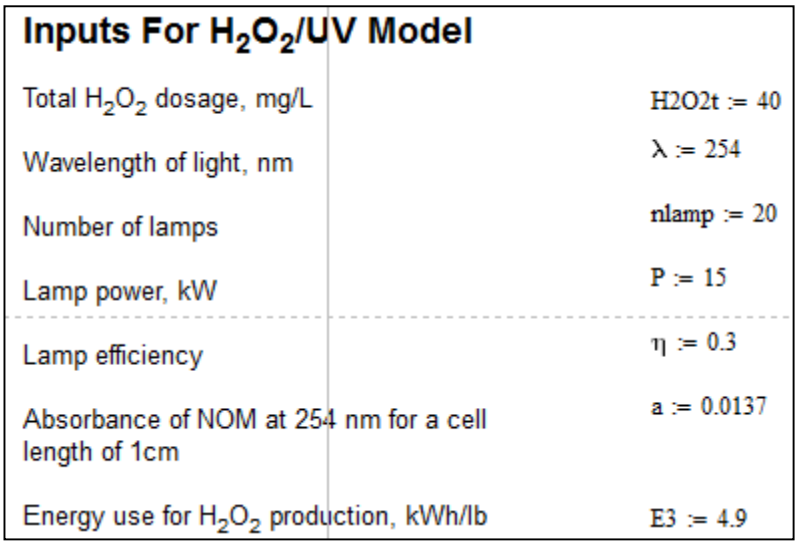

Figure E.13. Inputs for H_2O_2/UV model.

E.5.1.5 Inputs for O_3 R_c Model

When using O_3 R_c model, you should specify the initial ozone concentration, the reaction rate constant between ozone and target compound (which can be ignored for the most part because the direct oxidation of ozone is usually negligible as compared to hydroxyl radical), the R_c value, the ozone pseudo-first-order reaction rate constant, the transfer efficiency of ozone contactor, and the energy use for O_3 production.

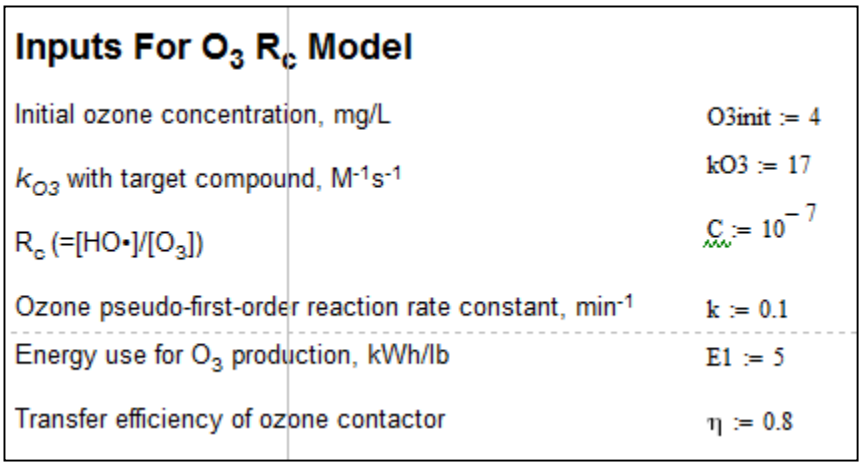

Figure E.14. Inputs for O_3 R_c model.

E.5.1.6 Inputs for Specific Reactors

These MathCAD files contain three kinds of reactors: CMBR, PFR and CMFR. You should enter reactor parameters in the corresponding columns. For CMBR, you should specify the reaction time for CMBR on "CMBR" column.

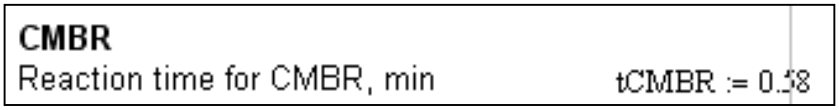

Figure E.15. Inputs for CMBR.

For CMFR or PFR, you should specify the flow rate of the reactor on "CMFR or PFR" column.

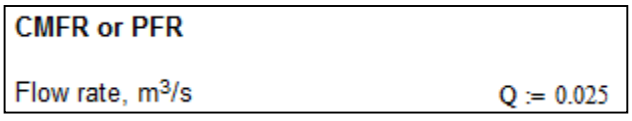

Figure E.16. Inputs for CMFR or PFR.

E.5.2 Calculation

The calculation part lists detailed calculation process.

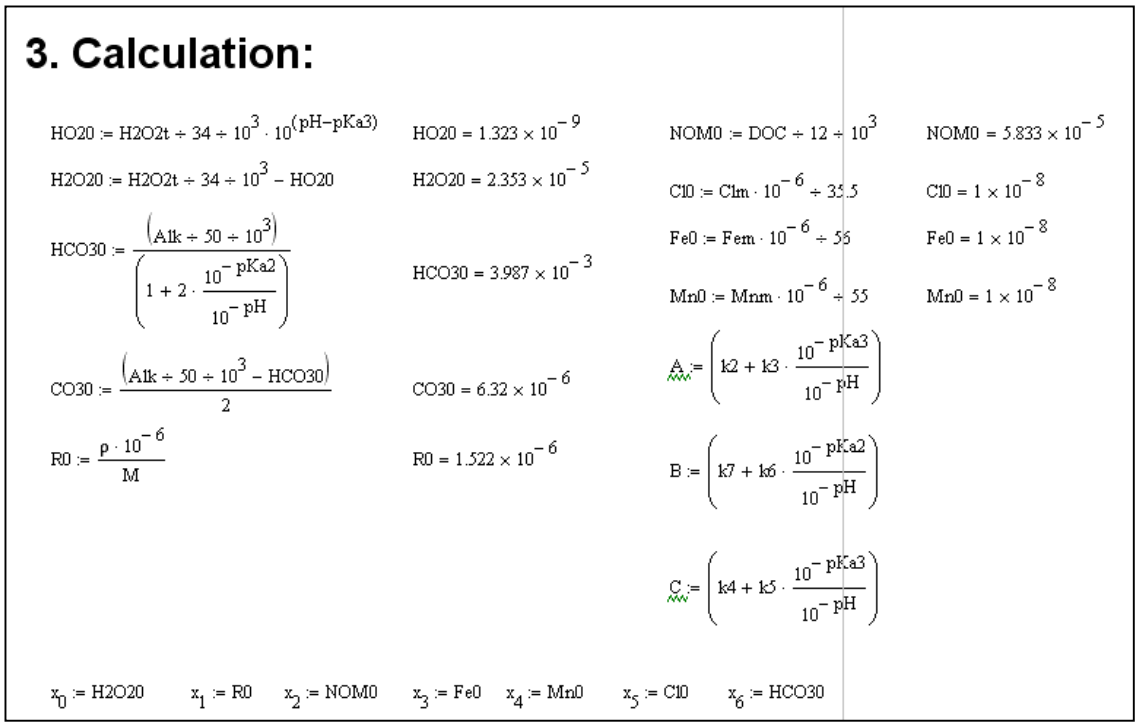

Figure E.17. Calculation part.

E.5.3 Output Data

The output data of each kind of reactor can be found on corresponding part, which contains the effluent concentration profiles of main species and the EE/O value profiles for the chosen process.

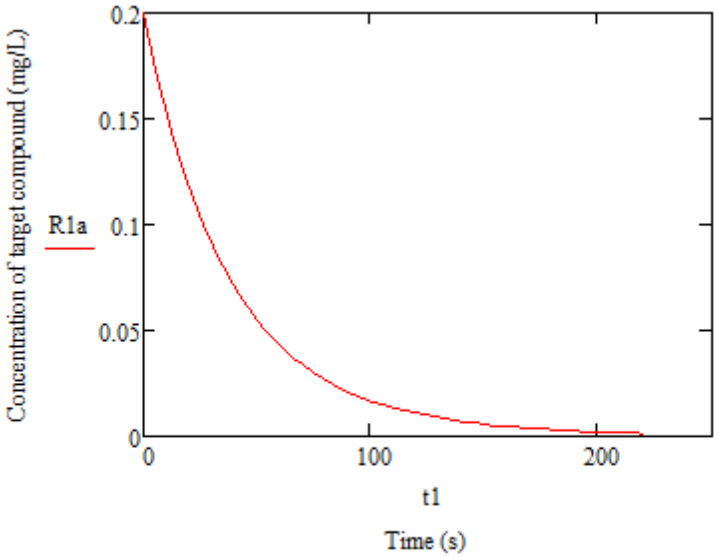

$RCMBR := R1a_{50}$ $RCMBR = 1.412 \times 10^{-3}$ mg/L

(a)

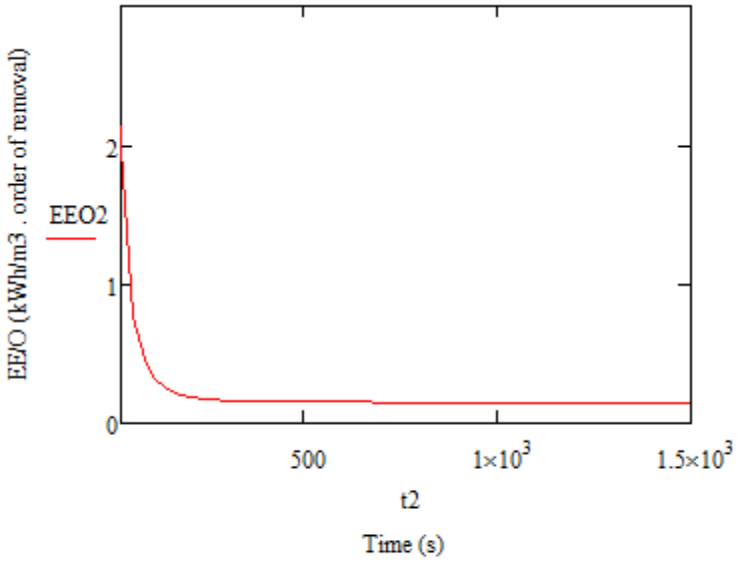

$EEOCMFR := EEO2_{50} = 0.151$ kWh/m^3 . order of removal

$EEOCMFR1 := EEOCMFR \div 264.2 \cdot 10^3 = 0.571$ $kWh/10^3$ gal . order of removal

(b)

Figure E.18. Outputs part. (a) Effluent concentration profile of target compound. (b) EE/O value profile.

E.6 Sample Problems

In this section, we will give several sample problems to aid users to understand how to use our models to optimize the designs of AOPs. The optimization processes of using simplified pseudo-steady state models and pseudo-steady state models are similar. For simplicity, in this part we only give three samples for the pseudo-steady state models, which include H_2O_2/O_3 model, H_2O_2 added after O_3 addition model, and UV/H_2O_2 model.

E.6.1 Sample Problem for Pseudo-Steady State H_2O_2/O_3 Model

E.6.1.1 Problem Statement

A small city discovered that one of its well was contaminated with 200 μg/L TCE. In order to use the well as drinking water source, the TCE needs to be reduced below its maximum contaminant level (MCL), which is 5 μg/L. During normal pumping operations, the well produces about 0.025 m^3/s water. The pH, alkalinity and DOC concentration are 7.5, 400 mg/L as $CaCO_3$, and 0.7 mg/L, respectively.

Compound	Influent concentration		HO• Rate Constant, $k_{HO\bullet}$, L/mole•s
	(μg/L)	(μmol/L)	
TCE	200	1.52	4.20×10^9
DOC	700		3.90×10^8

In this case, we will design a H_2O_2/O_3 process that can remove the target compound below its MCL and determine the optimum operational parameters including H_2O_2 dosage and overall mass transfer coefficient for O_3. A plug flow reactor (PFR) will be designed, considering the follow information: (1) the partial pressure of ozone is 0.1 atm, (2) the Henry's law constant for O_3 at 23℃ is 83.9 atm-L/mole, (3) the influent

concentration of chloride ion is 2 mg/L, (4) the influent concentration of iron ion(II) is 0.05 mg/L, (5) the influent concentration of manganese ion(II) is 0.1 mg/L, (6) the energy use for O_3 production is 5 kWh/lb, (7) the energy use for H_2O_2 production is 4.9 kWh/lb, and (8) the transfer efficiency of the ozone contactor is 80%.

E.6.1.2 Solution

Before we optimize our design of the H_2O_2/O_3 process, we should determine our treatment objective of the target pollutant, TCE. According to the MCL of TCE, which is 5 μg/L, we will set the treatment objective to be 3 μg/L, which is below the MCL. A plug flow reactor (PFR) will be designed in this example. For simplicity, we will use a fixed hydraulic retention time of 4 min. However, in practice, users can use different hydraulic retention times and determine the optimum value by comparing the EE/O for each retention time.

To determine the optimum operational parameters, we will find different pairs of H_2O_2 dosages and overall mass transfer coefficient for O_3 that can achieve the desired removal of TCE. By comparing the calculated EE/O values for all pairs, we will get the optimum H_2O_2 dosages and overall mass transfer coefficient for O_3. The detailed way of determining the operational parameters is shown as below.

(1) Determine the reactor volume

With a hydraulic retention time of 4 min, the volume of the reactor can be calculated by $V = Q \times \tau = 0.025 \times 4 \times 60 = 6\ m^3$, where Q is the flow rate and τ is the hydraulic retention time.

(2) Determine the overall mass transfer coefficient for O_3

To evaluate the impact of ozone mass transfer on the performance of H_2O_2/O_3 process, we will model overall mass transfer coefficients for O_3 (k_La) ranging from 5.6×10^{-4} s^{-1} to 10^{-3} s^{-1} as listed in Table E2.

(3) Determine the H_2O_2 dosage for each overall mass transfer coefficient for O_3

For each k_La value, the proper H_2O_2 dosage to achieve the treatment objective is determined and the corresponding EE/O value is calculated, which are listed in Table E2. We should notice that the proper H_2O_2 dosage mentioned above might not be easily found. Users can first try a relatively large range of H_2O_2 dosage and then gradually narrow the searching range of H_2O_2 dosage until users find the proper H_2O_2 dosage with a satisfied accuracy. At the same time, with an ozone partial pressure of 0.1 atm, the molar ratio of H_2O_2 dosage to the ozone dosage that transfers from the gas phase to the liquid phase can also be calculated by

$$r_{[H_2O_2]/[O_3]} = \frac{C_{H_2O_2} \times \frac{1\ \text{gram}}{10^3\ \text{milligram}}}{M_{H2O2} \times k_L a \times \frac{P}{H} \times \tau \times \frac{60\ \text{seconds}}{\text{minutes}}}$$

where $r_{[H2O2]/[O3]}$ is the molar ratio of H_2O_2 dosage to the ozone dosage transferred to liquid phase, mM/mM; C_{H2O2} is the concentration of H_2O_2 in the liquid phase, mg/L; k_La is the overall mass transfer coefficient for O_3, s^{-1}, P is the partial pressure of ozone in the gas phase, atm; H is the Henry's law constant for O_3, atmL/mol; and τ is the hydraulic retention time for PFR, min. From Table C.2, we can see that the $r_{[H2O2]/[O3]}$ are modeled ranging from 0.39 to 1.08.

Table E.2. Simulation results of various operational conditions for H_2O_2/O_3 process that

achieves the treatment objective

Run NO.	k_La ($10^{-4}s^{-1}$)	H_2O_2 dosage (mM)	$R_{[H2O2]/[O3]}$ (mM/mM)	EE/O (kWh/m^3. order of removal)
1	5.6	0.17	1.08	0.092
2	5.7	0.15	0.94	0.089
3	6.0	0.13	0.76	0.088
4	6.5	0.12	0.64	0.090
5	7.0	0.11	0.57	0.096
6	7.5	0.11	0.53	0.101
7	8.0	0.11	0.49	0.105
8	9.0	0.11	0.44	0.117
9	10.0	0.11	0.39	0.127

To give users a detailed instruction about how to use our supplied MathCAD file for H_2O_2/O_3 process to get the effluent concentration of target compound and EE/O values for a single run, we will run NO.3 in Table 6.1 as an example in the following part.

Get start

Open the MathCAD file for H_2O_2/O_3 process and the main window will appear.

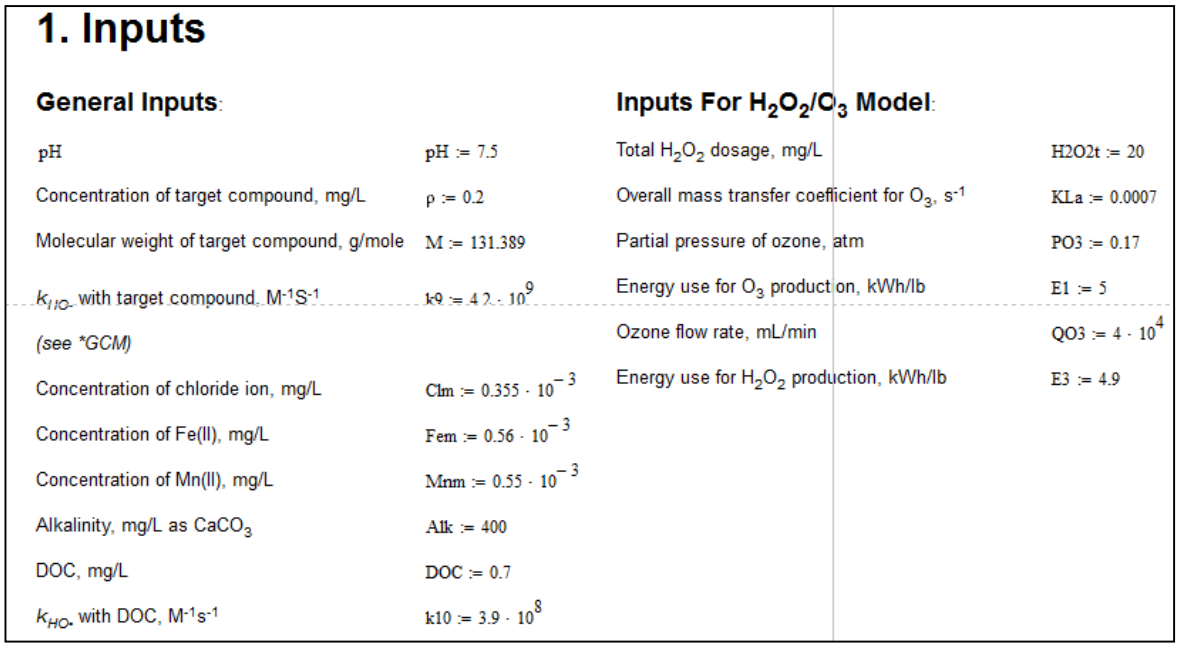

Figure E.19. Main window of H_2O_2/O_3 model.

General input

The general inputs are specified in the left corner of the input part shown in Figure E19. The pH is 7.5; the concentration of target compound (TCE) is 200 μg/L; the molecular weight of target compound (TCE) is 131.389 g/mole; $k_{HO\bullet}$ with target compound is 4.20×10^{9} $M^{-1}s^{-1}$; concentrations of chloride ion, iron ion(II), and manganese ion(II) is 2 mg/L, 0.05 mg/L, and 0.1 mg/L, respectively; alkalinity is 400 mg/L as $CaCO_3$; DOC concentration is 0.7 mg/L; $k_{HO\bullet}$ with DOC is 3.9×10^{8} $M^{-1}s^{-1}$; and the total reactor volume is 6 m^3.

General Inputs:

pH	pH := 7.5
Concentration of target compound, mg/L	ρ := 0.2
Molecular weight of target compound, g/mole	M := 131.389
$k_{HO\bullet}$ with target compound, $M^{-1}S^{-1}$	$k9 := 4.2 \cdot 10^{9}$
*(see *GCM)*	
Concentration of chloride ion, mg/L	Clm := 2
Concentration of Fe(II), mg/L	Fem := 0.05
Concentration of Mn(II), mg/L	Mnm := 0.1
Alkalinity, mg/L as $CaCO_3$	Alk := 400
DOC, mg/L	DOC := 0.7
$k_{HO\bullet}$ with DOC, $M^{-1}s^{-1}$	$k10 := 3.9 \cdot 10^{8}$
Total reactor volume, m^3	v := 6

Figure E.20. General input portion.

Inputs for H_2O_2/O_3 model

The inputs for H_2O_2/O_3 model are specified in the middle part of the main window shown in Figure E19. The total H_2O_2 dosage is 0.13 mM (4.4 mg/L); the overall mass transfer coefficient for O_3 is $6\times10^{-4}s^{-1}$; the partial pressure of ozone is 0.1 atm; the energy use for O_3 production is 5 kWh/lb O_3; the transfer efficiency of ozone contactor is 0.8; and the energy use for H_2O_2 production is 4.9 kWh/lb.

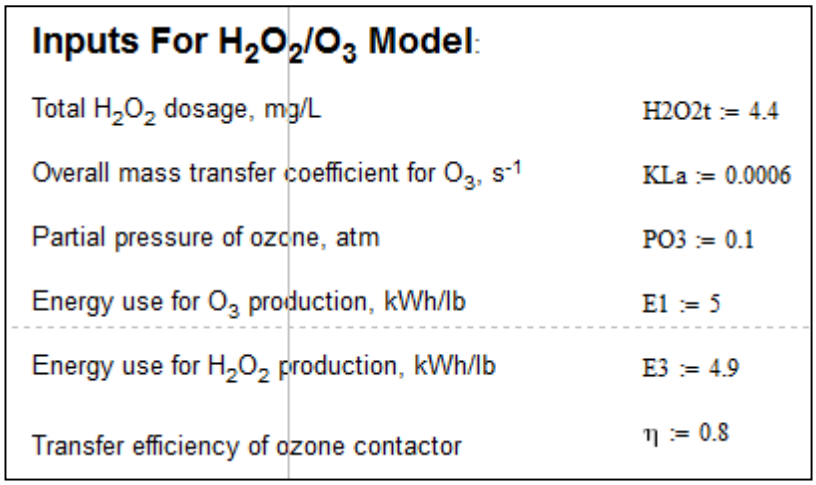

Figure E.21. H_2O_2/O_3 model input portion.

Inputs for reactor properties

In this solution, a PFR system will be designed. The inputs for PFR are specified in CMFR or PFR column of inputs portion. The flow rate is 0.025 m^3/s.

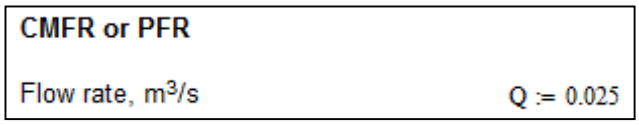

Figure E.22. PFR input portion.

Viewing results

We can obtain the effluent concentration profile of target compound and EE/O value of the process from the "output of PFR" part. In this solution, the effluent concentration of TCE is 3 μg/L and the EE/O for H_2O_2/O_3 model is 0.088 kWh/m^3 or

0.334 kWh/kgal.

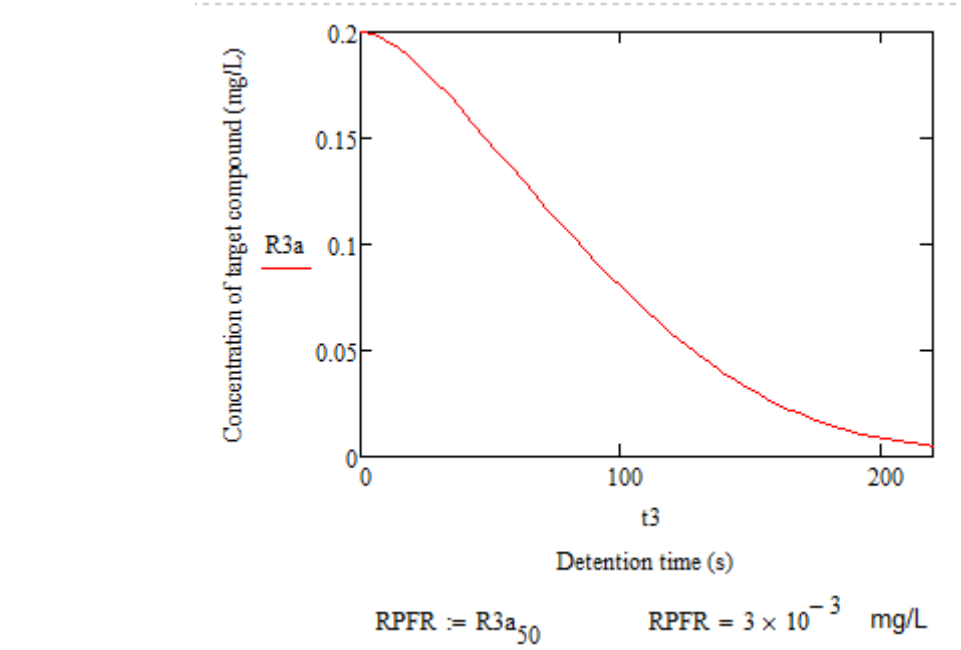

(a)

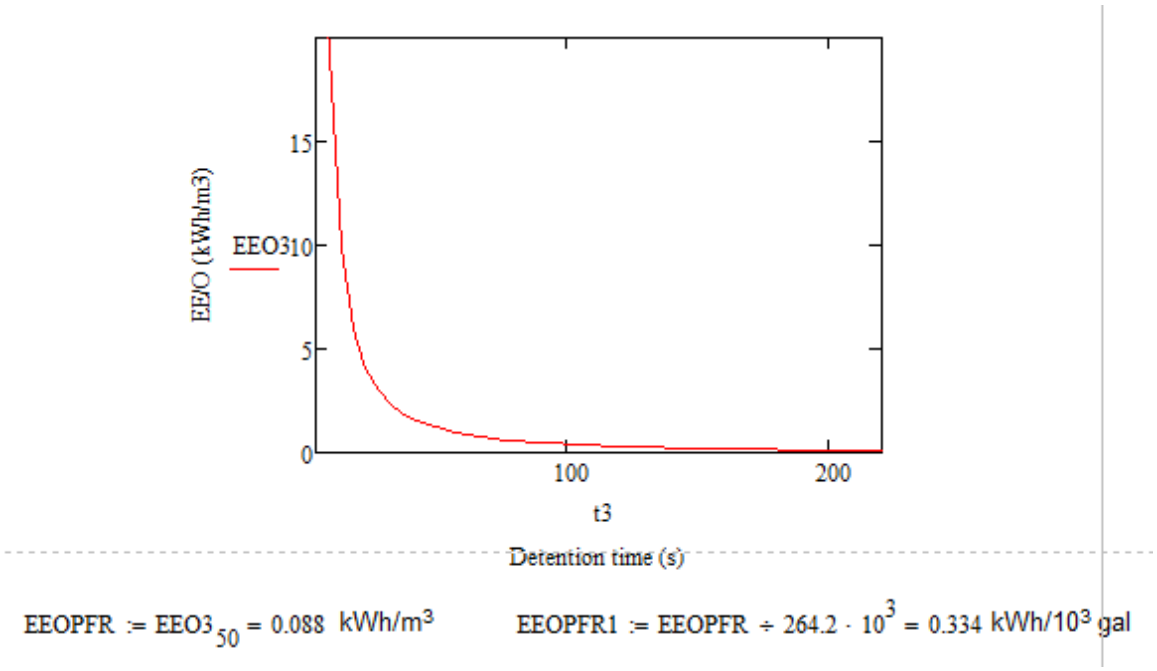

(b)

Figure E.23. H_2O_2/O_3 model output portion of PFR. (a) Effluent concentration profile of target compound. (b) EE/O value profile.

(4) Determine the optimum overall mass transfer coefficient of O_3 and H_2O_2 dosage

We can compare the EE/O to get the optimum H_2O_2 dosages and overall mass transfer coefficients for O_3. The EE/O values of all cases in Table E2 are plotted in Figure E24. We can see that increasing the $r_{[H2O2]/[O3]}$ value will decrease the EE/O value at low $r_{[H2O2]/[O3]}$ levels and increase the EE/O values at high $r_{[H2O2]/[O3]}$ levels. The lowest EE/O value is achieved in run NO.3, when $r_{[H2O2]/[O3]}$ is 0.76, H_2O_2 dosage is 0.13 mM (4.4 mg/L), and k_La is 0.0006 s^{-1}.

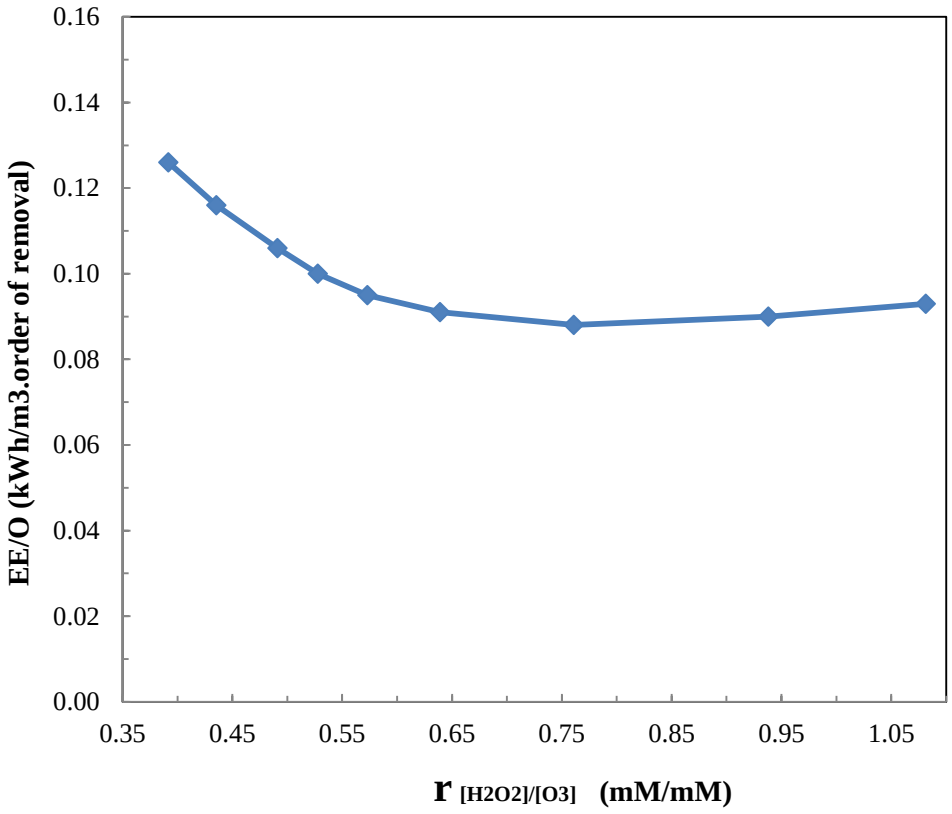

Figure E.24. The impact of $r_{[H2O2]/[O3]}$ on the EE/O values of H_2O_2/O_3 process.

(5) Conclusion

In this example, a PFR will be designed.

The optimized design parameters are as below:

Volume of reactor: 6 m^3

Overall mass transfer coefficients for O_3: 0.0006 s^{-1}

H_2O_2 dosage: 4.4 mg/L

E.6.2 Sample Problem for Pseudo-Steady State H_2O_2 Added after O_3 Addition Model

E.6.2.1 Problem Statement

A small city discovered that one of its well was contaminated by some chemical pollutants. Ozone was first added to the water to disinfect it, and when certain Ct disinfection credit was obtained, it is useful to estimate the potential of adding H_2O_2 to remove target pollutant, TCE. The concentration of TCE is 50 μg/L. In order to use the water as drinking water, the TCE needs to be reduced below its maximum contaminant level (MCL), which is 5 μg/L. During normal pumping operations, the well produces about 0.025 m^3/s water. The pH, alkalinity and DOC concentration are 7.5, 400 mg/L as $CaCO_3$, and 0.7 mg/L, respectively.

Compound	Influent concentration		HO• Rate Constant, $k_{HO\bullet}$, L/mole•s
	(μg/L)	(μmol/L)	
TCE	50	0.38	4.20×10^9
DOC	700		3.90×10^8

In this example, we will design a H_2O_2 added after O_3 addition system that can remove the target compound below its MCL and determine the optimum operational parameters including initial dissolved O_3 concentration at the point of H_2O_2 addition and the H_2O_2 dosage. A plug flow reactor (PFR) will be designed, considering the follow information:

(1) the influent concentration of chloride ion is 0.5 mg/L, (2) the influent concentration of iron ion(II) is 0.05 mg/L, (3) the influent concentration of manganese ion(II) is 0.1 mg/L, (4) the energy use for O_3 production is 5 kWh/lb, (5) the energy use for H_2O_2 production is 4.9 kWh/lb, and (6) the transfer efficiency of ozone contactor is 80%.

E.6.2.2 Solution

Before we optimize our design of the H_2O_2 added after O_3 addition process, we should determine our treatment objective of the target pollutant, TCE. According to the MCL of TCE, which is 5 μg/L, we will set the treatment objective to be 3 μg/L, which is below the MCL. A plug flow reactor (PFR) will be designed in this example. For simplicity, we will use a fixed hydraulic retention time of 4 min. However, in practice, users can use different hydraulic retention times and determine the optimum value by comparing the EE/O for each retention time.

To determine the optimum operational parameters, we will find different pairs of H_2O_2 dosages and initial dissolved O_3 concentration that can achieve the desired removal of TCE. By comparing the calculated EE/O values for all pairs, we will get the optimum H_2O_2 dosages and initial dissolved O_3 concentration. The detailed way of determining the operational parameters is shown as below.

(1) Determine the reactor volume

With a hydraulic retention time of 4 min, the volume of the reactor can be calculated by $V = Q \times \tau = 0.025 \times 4 \times 60 = 6\ m^3$, where Q is the flow rate and τ is the hydraulic retention time.

(2) Determine initial dissolved O_3 concentration

We will model the initial dissolved O_3 concentration at the point of H_2O_2 addition ($[O_3]_{diss}$) ranging from 1.5 mg/L (0.03 mM) to 5.0 mg/L (0.10 mM) as listed in Table E3.

(3) Determine the H_2O_2 dosage for each initial dissolved O_3 concentration

For each $[O_3]_{diss}$, the proper H_2O_2 dosage to achieve the treatment objective is determined and the corresponding EE/O value is calculated, which are listed in Table E3. We should notice that the proper H_2O_2 dosage mentioned above might not be easily found. Users can first try a relatively large range of H_2O_2 dosage and then gradually narrow the searching range of H_2O_2 dosage until users find the proper H_2O_2 dosage with a satisfied accuracy. At the same time, we can calculate the molar ratio of H_2O_2 dosage to $[O_3]_{diss}$ ($[H_2O_2]/[O_3]_{diss}$). From Table C.3, we can see that we simulate the $[H_2O_2]/[O_3]_{diss}$ value ranging from 0.14 to 1.32.

Table E.3. Simulation results of various operational conditions for H_2O_2 added after O_3 addition process that achieves the treatment objective

Run NO.	$[O_3]_{diss}$ (mg/L)	H_2O_2 dosage (mg/L)	$[H_2O_2]/[O_3]_{diss}$ (mM/mM)	EE/O (kWh/m^3.order of removal)
1	1.5	1.4	1.32	0.0284
2	1.6	1.2	1.06	0.0272
3	1.7	1.1	0.91	0.0265
4	1.8	1.0	0.78	0.0264
5	1.9	0.9	0.67	0.0274
6	2.0	0.8	0.56	0.0294
7	2.5	0.6	0.34	0.0338
8	3.0	0.6	0.28	0.0369
9	3.5	0.5	0.20	0.0427
10	4.0	0.5	0.18	0.0487
11	4.5	0.5	0.16	0.0549
12	5.0	0.5	0.14	0.0604

To give users a detailed instruction about how to use our supplied MathCAD file for H_2O_2 added after O_3 addition process to get the effluent concentration of target compound and EE/O values for a single run, we will run the NO.6 in Table C.3 as an

example in the following part.

Get start

Open the MathCAD file for H_2O_2 added after O_3 addition process and the main window will appear.

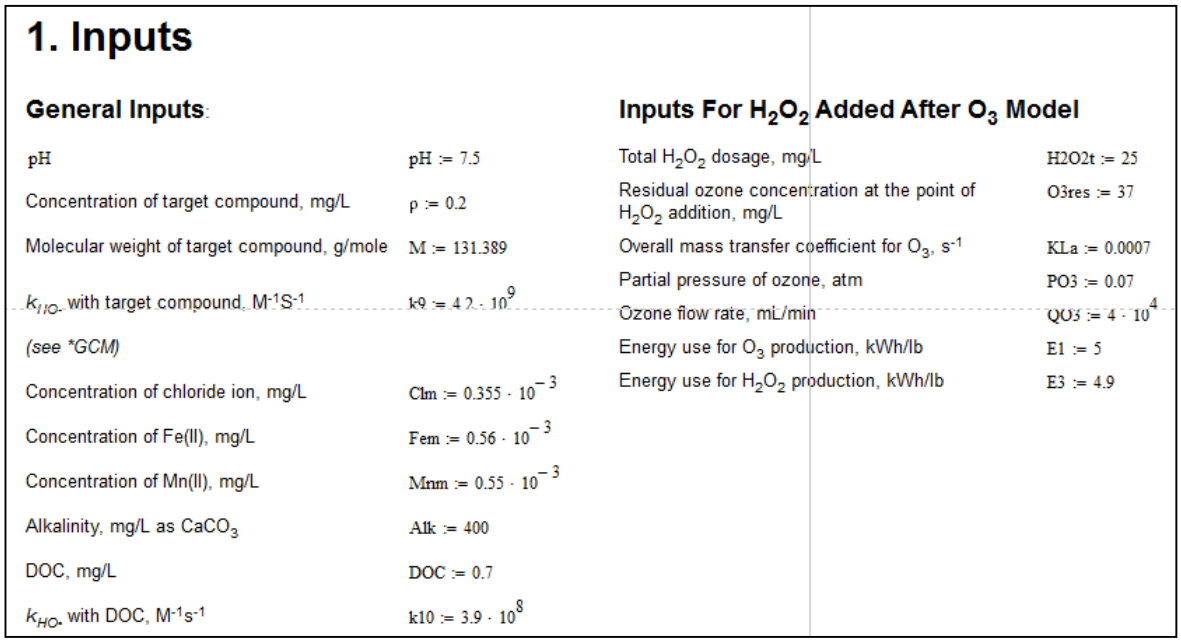

Figure E.25. Main input window of H_2O_2 added after O_3 addition model.

General input

The general inputs are specified in the left corner of the main window shown in Figure E25. The pH is 7.5; the concentration of target compound (TCE) is 50 μg/L; the molecular weight of target compound is 131.389 g/mole; $k_{HO\bullet}$ with target compound is 4.20×10^9 $M^{-1}s^{-1}$; concentrations of chloride ion, iron ion(II), and manganese ion(II) are 0.5 mg/L, 0.05 mg/L, and 0.1 mg/L, respectively; alkalinity is 400 mg/L as $CaCO_3$; DOC concentration is 0.7 mg/L; $k_{HO\bullet}$ with DOC is 3.90×10^8 $M^{-1}s^{-1}$; and the total reactor volume is 6 m^3.

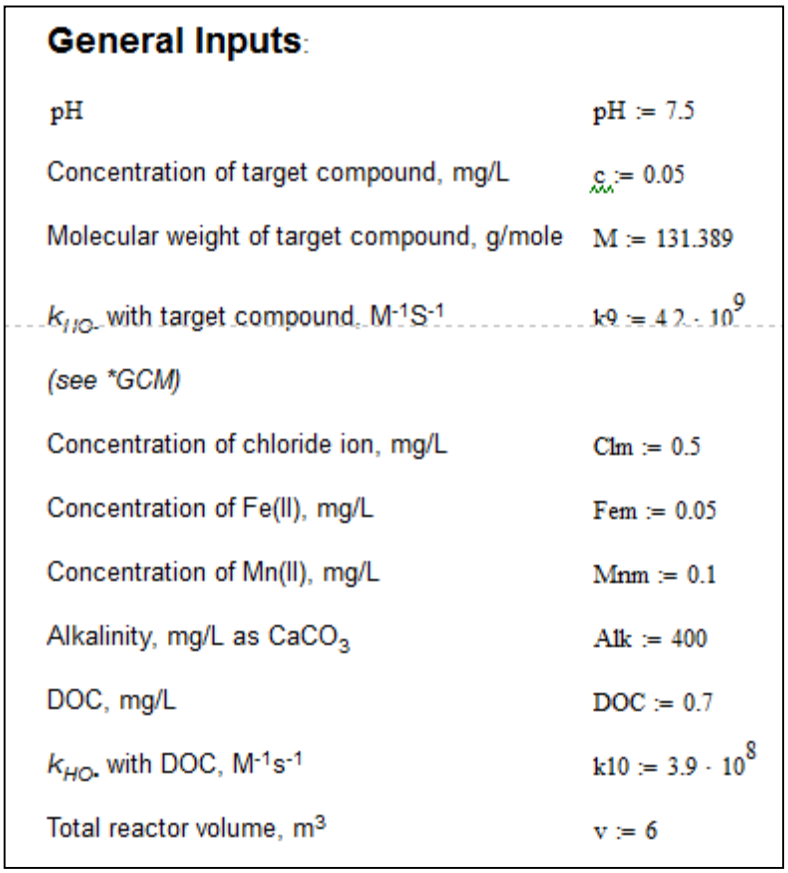

Figure E.26. General input portion.

Inputs for H_2O_2 added after O_3 addition model

The inputs for H_2O_2 added after O_3 addition model are specified in the middle part of the main window shown in Figure E25. The H_2O_2 dosage is 0.8 mg/L; the initial ozone concentration at the point of H_2O_2 addition is 2 mg/L; the transfer efficiency of ozone contactor is 0.8; the energy use for O_3 production is 5 kWh/lb; and the energy use for H_2O_2 production is 4.9 kWh/lb.

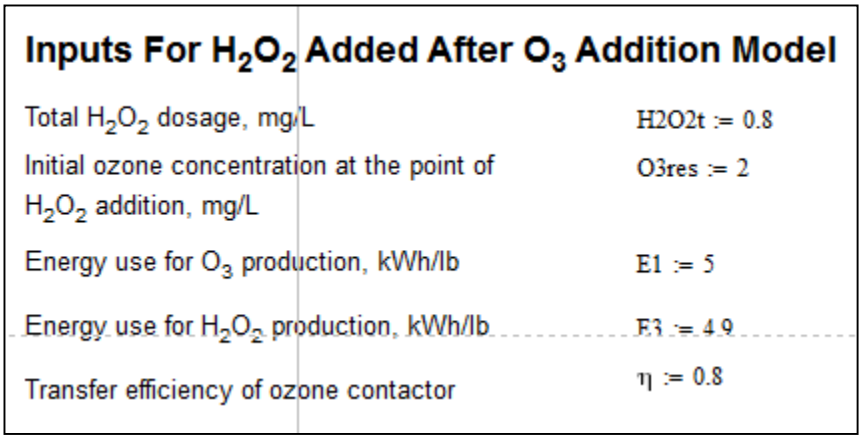

Figure E.27. H_2O_2 added after O_3 addition model input portion.

Inputs for reactor properties

In this solution, a PFR system will be designed. The inputs for PFR are specified in CMFR or PFR column of inputs portion. The flow rate is 0.025 m^3/s.

Figure E.28. PFR input portion.

Viewing results

We can obtain the effluent concentration profile of target compound and EE/O value of the process from the "output of PFR" part. In this solution, the effluent concentration of TCE is 3 μg/L. The EE/O for H_2O_2 added after O_3 addition model is 0.0294 kWh/m^3.order of removal or 0.1114 kWh/kgal.order of removal.

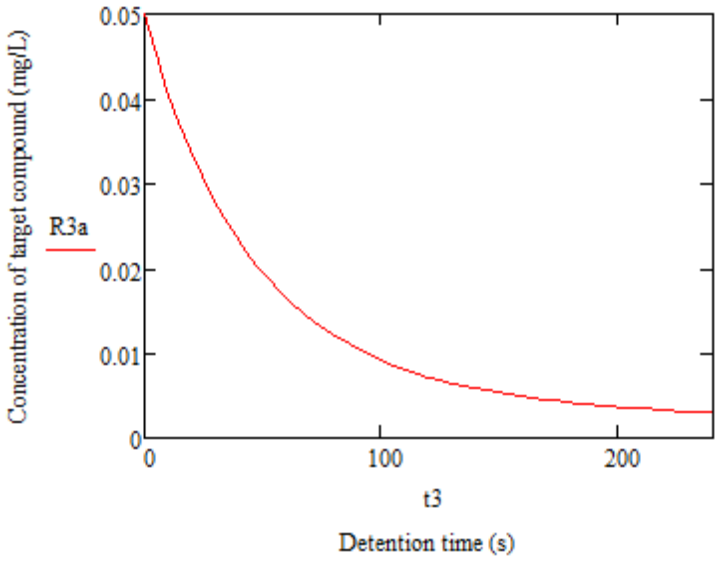

$RPFR := R3a_{50}$ $RPFR = 3 \times 10^{-3}$ mg/L

(a)

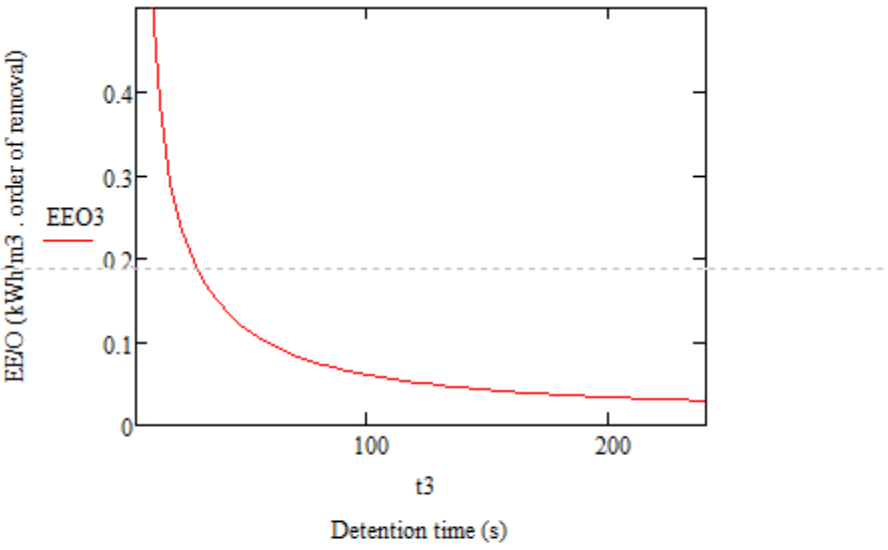

$EEOPFR := EEO3_{50} = 0.0294$ kWh/m^3 . order of removal

$EEOPFR1 := EEOPFR \div 264.2 \cdot 10^3 = 0.1114$ kWh/10^3 gal . order of removal

(b)

Figure E.29. H_2O_2 added after O_3 addition model output portion of PFR. (a) Effluent concentration profile of target compound. (b) EE/O value profile.

(4) Determine the optimum initial dissolved O_3 concentration and H_2O_2 dosage

We can then compare the EE/O to get the optimum H_2O_2 dosages and initial dissolved O_3 concentration at the point of H_2O_2 addition. The EE/O values of all cases in Table E3 are plotted in Figure E30. We can see that increasing the $[H_2O_2]/[O_3]_{diss}$ value will decrease the EE/O value at low $[H_2O_2]/[O_3]_{diss}$ levels and increase the EE/O values at high $[H_2O_2]/[O_3]_{diss}$ levels. The lowest EE/O value is achieved in run NO.4, when $[H_2O_2]/[O_3]_{diss}$ is 0.78, H_2O_2 dosage is 1.0 mg/L, and initial dissolved O_3 concentration is 1.8 mg/L.

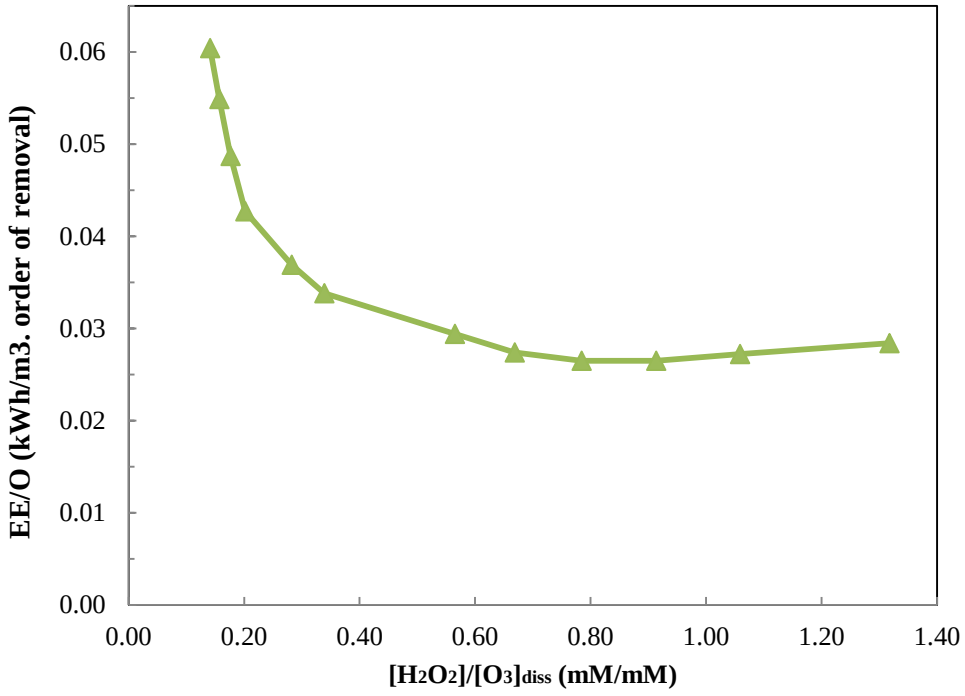

Figure E.30. The impact of molar ratio of H_2O_2 dosage to initial dissolved ozone concentration on the EE/O values of H_2O_2 added after O_3 addition process.

(5) Conclusion

In this example, a PFR will be designed.

The design parameters are as below:

Volume of reactor: 6 m^3

Initial dissolved O_3 concentration at the point of H_2O_2 addition: 1.8 mg/L

H_2O_2 dosage: 1.0 mg/L

E.6.3 Sample Problem for Pseudo-Steady-State H_2O_2/UV Model

E.6.3.1 Problem Statement

A small city discovered that one of its well was contaminated with 200 μg/L TCE. In order to use the well as drinking water source, the TCE needs to be reduced below its maximum contaminant level (MCL), which is 5 μg/L. The pH, alkalinity, and DOC concentration are 6.8, 400 mg/L as $CaCO_3$, and 0.7 mg/L, respectively. The following table shows some important physicochemical properties of H_2O_2, TCE and NOM.

Compound	MW, g/mole	OH Radical rate constant, k_{OH}, L/mole•s	Extinction coefficient, ε, L/mole•cm	Quantum yield, ϕ
TCE	131.389	4.20×10^9	Ignored	0
NOM	NA	3.90×10^8	0.0196	0
H_2O_2	34.015	-	19.6	0.5

In this example, we will design a UV/H_2O_2 system that can remove the target compound below its MCL and determine the optimum operational parameters including H_2O_2 dosage, and total lamp power. A plug flow reactor (PFR) will be designed, considering the follow information: (1) for simplicity, the UV-light intensity is monochromatic at 254 nm and that the lamps are 20% efficient, (2) the influent concentration of chloride ion is 2 mg/L, (3) the influent concentration of iron ion(II) is 0.05 mg/L, (4) the influent

concentration of manganese ion(II) is 0.1 mg/L, (5) the absorbance of NOM at 254 nm for a cell path length of 1cm is 0.014, and (6) the energy use for H_2O_2 production is 4.9 kWh/lb.

E.6.3.2 Solution

Before we optimize our design of the UV/H_2O_2 process, we should determine our treatment objective of the target pollutant, TCE. According to the MCL of TCE, which is 5 μg/L, we will set the treatment objective to be 3 μg/L, which is below the MCL. A plug flow reactor (PFR) will be designed in this example. For simplicity, we will use a fixed hydraulic retention time of 4 min. However, in practice, users can use different hydraulic retention times and determine the optimum value by comparing the EE/O for each retention time.

To determine the optimum operational parameters, we will find different pairs of H_2O_2 dosages and total lamp power that can achieve the desired removal of TCE. By comparing the calculated EE/O values for all pairs, we will get the optimum H_2O_2 dosages and total lamp power. Because the residual H_2O_2 for the UV/H_2O_2 process might be detrimental to the environment if they are directly discharged into the public water system, we should also consider the residual H_2O_2 concentration for all simulation when we optimize our operational parameters. The detailed way of determining the operational parameters is shown as below.

(1) Determine the reactor volume

With a hydraulic retention time of 4 min, the volume of the reactor can be calculated by $V = Q \times \tau = 0.025 \times 4 \times 60 = 6\ m^3$, where Q is the flow rate and τ is the hydraulic retention time.

(2) Determine the total lamp power

We will model the total lamp power ranging from 20 kW to 45 kW as listed in Table E4. With a reactor volume of 6 m^3, the total lamp power is related to the UV intensity by the equation below

,

where $P_{U\text{-}V}$ is the UV intensity, einsteins/L·s; P is the total lamp power, kW; η is the lamp efficiency, dimensionless; N_{av} is the Avogadro's number, $mole^{-1}$; V is the reactor volume, m^3; h is the Planck's constant, J/Hz; and ν is the light frequency, Hz. We should notice that in practice, the lamp efficiency may vary for different options of UV lamp. However, in this sample problem, we assume the lamp efficiency is 20% for simplicity. We can calculate the UV intensity corresponding to each total lamp power as shown in Table E4.

Table E.4. The UV intensity corresponding to various total lamp power

Run NO.	Total lamp power (kW)	UV intensity (10^{-6} eins./L•s)
1	20	0.39
2	21	0.41
3	22	0.43
4	24	0.47
5	30	0.59
6	40	0.79
7	45	0.89

(3) Determine the H_2O_2 dosage for each total lamp power

For each total lamp power, the proper H_2O_2 dosage to achieve the treatment objective is determined, and the corresponding residual H_2O_2 concentration and EE/O value are recorded in Table E5. We should notice that the proper H_2O_2 dosage mentioned

above might not be easily found. Users can first try a relatively large range of H_2O_2 dosage and then gradually narrow the searching range of H_2O_2 dosage until users find the proper H_2O_2 dosage with a satisfied accuracy.

Table E.5. Simulation results of various operational conditions for UV/H_2O_2 process that achieves the treatment objective

Run NO.	Total lamp power (kW)	UV intensity (10^{-6} eins./L•s)	H_2O_2 dosage (mg/L)	Residual H_2O_2 concentration (mg/L)	EE/O (kWh/m^3.order of removal)
1	20	0.39	26.9	21.2	0.281
2	21	0.41	24.2	18.6	0.271
3	22	0.43	22.1	16.5	0.265
4	24	0.47	19.0	13.5	0.258
5	30	0.59	13.8	8.5	0.264
6	40	0.79	10.0	4.9	0.303
7	45	0.89	8.8	3.9	0.327

To give users a detailed instruction about how to use our supplied MathCAD file for UV/H_2O_2 process to get the effluent concentration of target compound and EE/O values for a single run, we will run the NO.5 in Table 6.4 as an example in the following part.

Get start

Open the MathCAD file for UV/H_2O_2 process and the main window will appear.

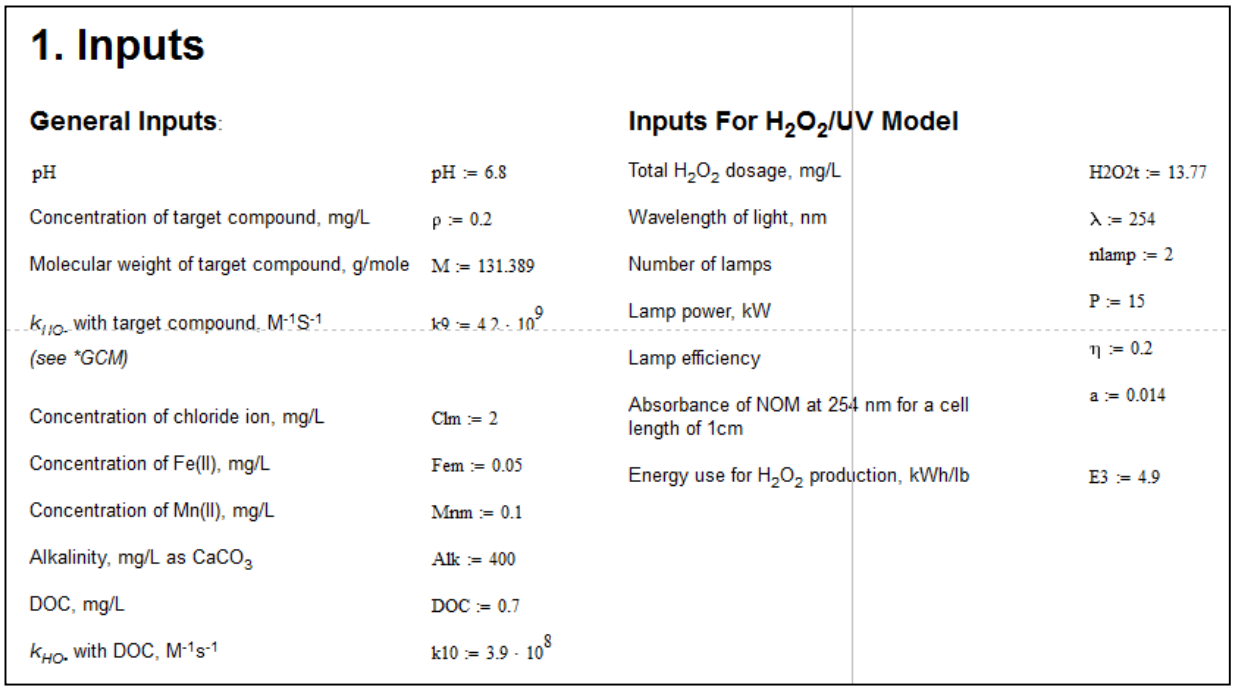

Figure E.31. Main input window.

General input

The general inputs are specified in the upper left corner of the main input window, as shown in Figure E31. The pH is 6.8; the concentration of the target compound (TCE) is 200 μg/L; the molecular weight of the target compound is 131 g/mole; the $k_{HO\bullet}$ with target compound is 4.20×10^{9} $M^{-1}s^{-1}$; the concentrations of chloride ion, iron ion(II), and manganese ion(II) are 2 mg/L, 0.05 mg/L, and 0.1 mg/L, respectively; the alkalinity is 400 mg/L as $CaCO_3$; the DOC concentration is 0.7 mg/L; the $k_{HO\bullet}$ with DOC is 3.90×10^{8} $M^{-1}s^{-1}$; the total reactor volume is 6 m^3.

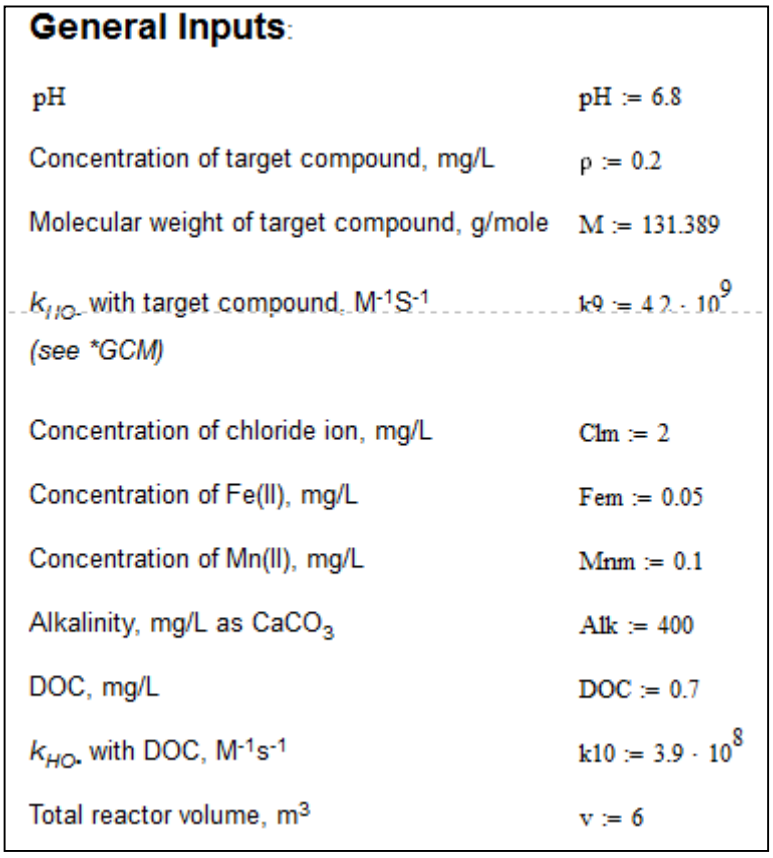

Figure E.32. General input portion of the main input window.

Inputs for H_2O_2/UV model

The inputs for the H_2O_2/UV model are specified in the middle of the main input window, as shown in Figure E31. The H_2O_2 dosage is 13.8 mg/L; the wavelength of light is 254 nm; the number of lamps is 2; the lamp power is 15 kW; the lamp efficiency is 0.2; the energy use for H_2O_2 production is 4.9 kWh/lb; and the absorbance of NOM at 254 nm for a cell path length of 1cm is 0.014.

Inputs For H_2O_2/UV Model	
Total H_2O_2 dosage, mg/L	H2O2t := 13.8
Wavelength of light, nm	λ := 254
Number of lamps	nlamp := 2
Lamp power, kW	P := 15
Lamp efficiency	η := 0.2
Absorbance of NOM at 254 nm for a cell length of 1cm	a := 0.014
Energy use for H_2O_2 production, kWh/lb	E3 := 4.9

Figure E.33. H_2O_2/UV model input portion of the main input window.

Viewing results

We can obtain the effluent concentration profile of target compound and EE/O value of the process from the "output of PFR" part. In this solution, the effluent concentration of TCE is 3 µg/L. The EE/O for H_2O_2/O_3 model is 0.264 kWh/m^3 or 1.000 kWh/kgal.

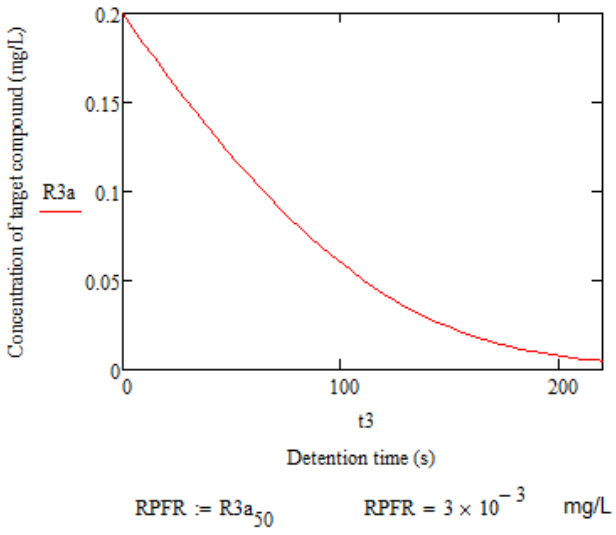

(a)

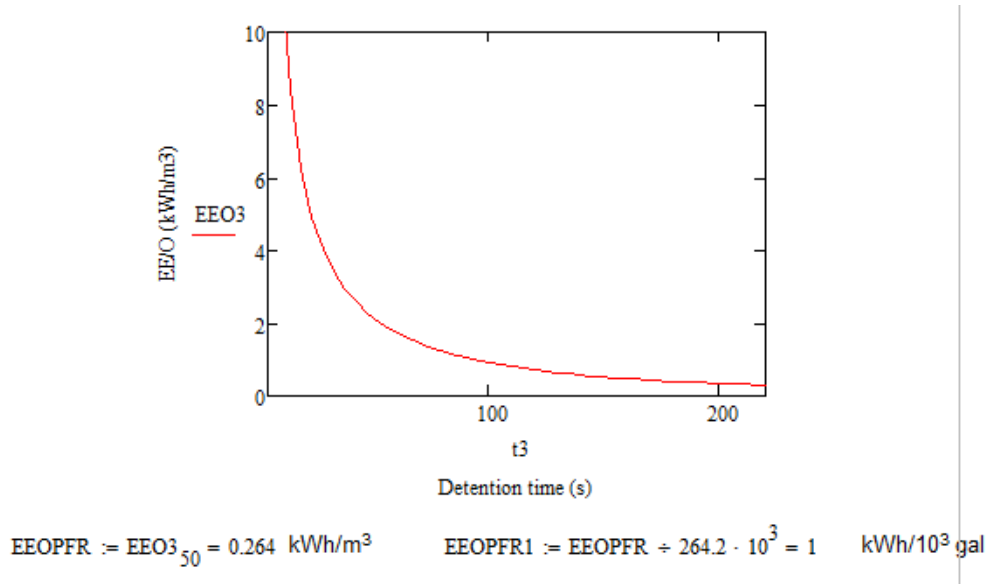

(b)

Figure E.34. UV/H_2O_2 model output portion of PFR. (a) Effluent concentration profile of target compound. (b) EE/O value profile.

We can also predict the residual H_2O_2 concentration from the "output of PFR" part. In this solution, the residual H_2O_2 concentration is 8.5 mg/L.

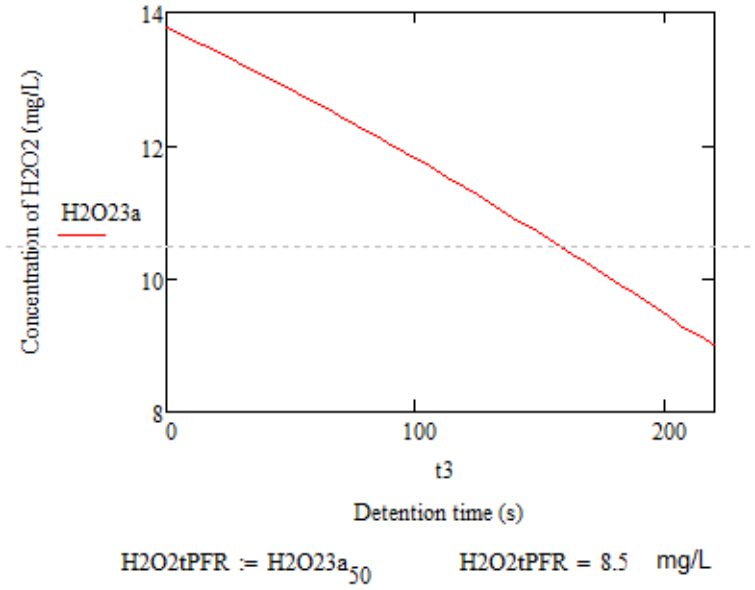

Figure E.35. The residual H_2O_2 concentration of UV/H_2O_2 model

(4) Determine the optimum H_2O_2 dosage and total lamp power

We can then compare the EE/O to get the optimum H_2O_2 dosages and total lamp

power. The EE/O values of all cases are plotted in Figure E36. From Table E5 and Figure E36, we can see that at low H_2O_2 dosage levels, the EE/O values are high even though the residual H_2O_2 concentrations are low and at high H_2O_2 dosage levels, both the EE/O values and residual H_2O_2 concentration are high. Both of these two H_2O_2 dosage levels might not be a good choice to design a cost effective UV/H_2O_2 process. At middle level of H_2O_2 dosage, the EE/O values are relatively low and the residual H_2O_2 concentrations are not very high, which might be an ideal region to choose the operational variables. The lowest EE/O value is achieved in run NO.4, when H_2O_2 dosage is 19.0 mg/L, the residual H_2O_2 concentration is 13.5 mg/L, and the total light power is 24 kW.

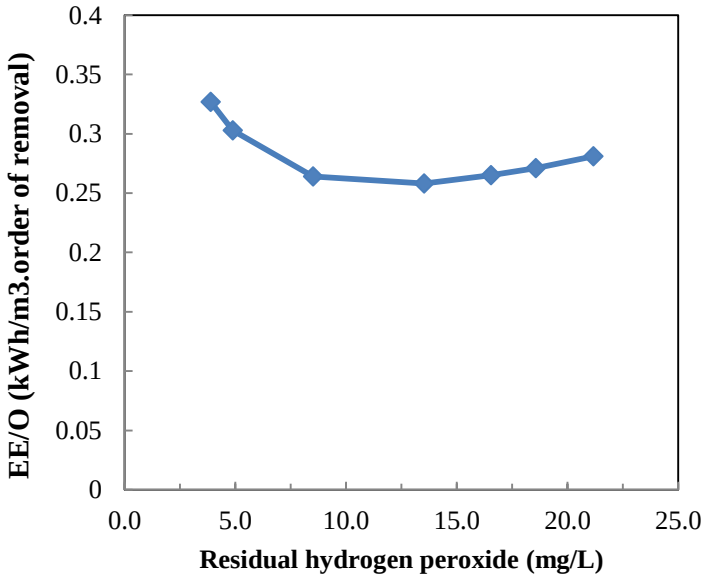

Figure E.36. The relation between the residual hydrogen peroxide and the EE/O values of H_2O_2/UV process.

(5) Conclusion

In this example, a PFR will be designed.

The design parameters are as below:

Volume of reactor: 6 m^3

Total light power: 24 kW

H_2O_2 dosage: 19.0 mg/L

REFERENCES

1. Rosenfeldt, E.J.; Linden, K.G. Degradation of endocrine disrupting chemicals bisphenol A, ethinyl estradiol, and estradiol during UV photolysis and advanced oxidation processes. *Environ. Sci. Technol*. 2004, 38, 5476-5483.
2. Huber, M.M.; Canonica S.; Park G-Y.; von Gunten U. Oxidation of pharmaceuticals during ozonation and advanced oxidation processes. *Environ. Sci. Technol*. 2003, 37, 1016-1024.
3. Stefan, M.I.; Hoy, A.R.; Bolton, J.R. Kinetics and mechanism of the degradation of acetone in dilute aqueous solution sensitized by the UV photolysis of hydrogen peroxide. *Environ. Sci. Technol*. 1996, 30, 2382-2390.
4. Stefan, M.I.; Bolton, J.R. Reinvestigation of the acetone degradation mechanism in dilute aqueous solution by the UV/H_2O_2 process. *Environ. Sci. Technol*. 1999, 33, 870-873.
5. Li, K.; Stefan, M.I.; Crittenden, J.C. Trichloroethene degradation by UV/H_2O_2 advanced oxidation process: product study and kinetic modeling. *Environ. Sci. Technol*. 2007, 41, 1696-1703.
6. Stefan, M.I.; Mack, J.; Bolton, J.R. Degradation pathways during the treatment of methyl tert-butyl ether by the UV/H_2O_2 process. *Environ. Sci. Technol*. 2000, 34, 650-658.
7. Stefan, M.I.; Bolton, J.R. Mechanism of the degradation of 1,4-dioxane in dilute aqueous solution using the UV/Hydrogen peroxide process. *Environ. Sci. Technol*. 1998, 32, 1588-1595.

8. Cooper, W.J.; Cramer, C.J.; Martin, N.H.; Mezyk, S.P.; O'Shea, K.E.; von Sonntag, C. Free radical mechanisms for the treatment of methyl tert-butyl ether (MTBE) via advanced oxidation/reductive processes in aqueous solutions. *Chem. Rev*. 2009, 109, 1302-1345.
9. Richardson, S. D. Water Analysis: Emerging contaminants and current issues. *Anal. Chem.* 2009, 81, 4645–4677.
10. Van Geem, K.M.; Reyniers, M.F.; Marin, G.B.; Song, J.; Matheu, D.M.; Green, W.H. Automatic reaction network generation using RMG for steam cracking of n-hexane. *AIChE J*. 2006, 52, 718-730.
11. Khan, S.S.; Broadbelt, L.J. Automated mechanism generation. Part 2: application to atmospheric chemistry of alkanes and oxygenates. *J. Atoms. Chem*. 2009, 63, 157-186.
12. Pfaendtner, J.; Broadbelt, L.J. Mechanistic modeling of lubricant degradation. 2. the autoxidation of decane and octane. *Ind. Eng. Chem. Res*. 2008, 47, 2897-2904.
13. Broadbelt, L.J.; Stark, S.M.; Klein, M.T. Computer generated pyrolysis modeling: on-the-fly generation of species, reactions, and rates. *Ind. Eng. Chem. Res*. 1994, 33, 790-799.
14. Li, K.; Crittenden, J. Computerized pathway elucidation for hydroxyl radical-induced chain reaction mechanisms in aqueous phase advanced oxidation processes. *Environ. Sci. Technol*. 2009, 43, 2831-2837.
15. Minakata, D.; Li, K.; Westerhoff, P.; Crittenden, J. Development of a group contribution method to predict aqueous phase hydroxyl radical (HO•) reaction rate constants. *Environ. Sci. Technol*. 2009, 43, 6220-6227.

16. Minakata, D.; Crittenden, J. Linear free energy relationships between aqueous phase hydroxyl radical reaction rate constants and free energy of activation. *Environ. Sci. Technol*. 2011a, 45, 3479-3486.
17. Minakata, D.; Song, W.; Crittenden, J. Reactivity of aqueous phase hydroxyl radical with halogenated carboxylate anions: experimental and theoretical studies. *Environ. Sci. Technol*. 2011b, 45, 6057-6065.
18. Minakata, D.; Mezyk, S.P.; Jones, J.W.; Daws, B.R.; Crittenden, J.C. Development of linear free energy relationships for aqueous phase radical-involved chemical reactions. *Environ. Sci. Technol*. 2014. Just accepted.
19. Lu, T.; Law, C.K. A directed relation graph method for mechanism reduction. *Proc. Combust. Inst.* 2005, 30, 1333-1341.
20. Office of pollution prevention and toxics, United States Environmental Protection Agency, Pollution prevention (P2) assessment framework. 1998.
21. William, W.M.; Howard, P.H. User's Guide for the ECOSAR Class Program, Syracuse Research Corporation, New York, 1998.
22. Office of Pollution Prevention and Toxics, United States Environmental Protection Agency, http://www.pbtprofiler.net/default.asp (accessed 2013).
23. United States Environmental Protection Agency, OncoLogicTM User's Manual, 2005.
24. Ervasti, H.K.; Lee, R.; Burgers, P.C.; Ruttink, P.; Terlouw, J.K. Dissociation of protonated oxalic acid $[HOOC\text{-}C(OH)_2]^+$ into $H_3O^+ + CO + CO_2$: An experimental and CBS-QB3 computational study. *Int. J. Mass Spectrom*. 2006, 249, 240-251.

25. Neta, P.; Huie, R.E.; Ross, A.B. Rate constants for reactions of peroxyl radicals in fluid solutions. *J. Phys. Chem. Ref. Data*. 1990, 19, 413-513.

26. Neta, P.; Grodkowski, J.; Ross, A.B. Rate constants for reactions of aliphatic carbon-centered radicals in aqueous solution. *J. Phys. Chem. Ref. Data*. 1996, 25, 709-1050.

27. Buxton, G.V.; Greenstock, C.L.; Helman, W.P.; Ross, A.B. Critical review of rate constants for reactions of hydrated electrons, hydrogen atoms and hydroxyl radicals ($\bullet OH/\bullet O^-$) in aqueous solution. *J. Phys. Chem. Ref. Data*. 1988, 17, 513-886.

28. Von Sonntag, C.; Schuchmann, H-P. The elucidation of peroxyl radical reactions in aqueous solution with the help of radiation-chemical methods. *Angew. Chem. Int. Ed. Engl*. 1991, 30, 1229-1253.

29. Hindmarsh, A. C.; Gear, C. W. Ordinary differential equation system solver. UCID-30001 Rev. 3 Lawrence Livermore Laboratory, Livermore, CA. 1974.

30. Schaefer, T.; Schindelka, J.; Hoffmann, D.; Herrmann, H. Laboratory kinetic and mechanistic studies on the OH-initiated oxidation of acetone in aqueous solution. *J. Phys. Chem. A.* 2012, 116, 6317-6326.

31. Russell, G.A. Deuterium-isotope effects in the autoxidation of aralkyl hydrocarbons – mechanism of the interaction of peroxy radicals. *J. Am. Chem. Soc*. 1957, 79, 3871-3877.

32. U.S. EPA, 2012 Edition of the drinking water standards and health advisories.

33. Zegota, H.; Schuchmann, M. N.; Schulz, D.; von Sonntag, C. Z. Acetonylperoxyl radicals, CH3COCH2O2 - a study on the gamma-radiolysis and pulse-radiolysis of acetone in oxygenated aqueous-solutions. *Naturforsch*. 1986, 41B, 1015-1022.
34. Schaefer, T.; Schindelka, J.; Hoffmann, D.; Herrmann, H. Laboratory kinetic and mechanistic studies on the OH-initiated oxidation of acetone in aqueous solution. *J. Phys. Chem. A.* 2012, 116, 6317-6326.
35. Elliott, A. J.; Buxton, G. V. Temperature dependence of the reactions hydroxyl-superoxide and hydroxyl-hydroperoxy in water up to 200 ℃. *J. Chem. Soc., Faraday Trans.* 1992, 88, 2465-2470.
36. Bielski, H. J.; Benon, H. J.; Cabelli, D. E.; Ravindra, L. A.; Alberta, A. B. Reactivity of perhydroxyl/superoxide radicals in aqueous solution. *J. Phys. Chem. Ref. Data.* 1985, 14, 1041-1100.
37. Holeman, J.; Bjergbakke, E.; Sehested, K. The importance of radial + radical reactions in pulse radiolysis of aqueous carbonate/bicarbonate. *Proc. Tihany Symp. Radiat. Chem*. 6(1), 149-153.
38. Eriksen, T. E.; Lind, J.; Merenyi, G. On the acid-base equilibrium of the carbonate radical. *Radiat. Phys. Chem*. 26(2), 197-199.
39. Perry, R. H.; Green, D. W.; Maloney, J. D. Chemical enginner's handbook 5th edition. McGraw-Hill, New York, 1981.
40. *CRC Handbook of Chemistry and Physics*, 86th ed.; Lide, D. R., Ed.; CRC Press, Inc.: Boca Raton, FL, 2005-2006.
41. Farhartaziz; Ross, A. B. Selected specific rate constants of transient from water in aqueous solution; U.S. Department of Commerce: Washington, DC, 1977.

42. Mertens, R.; von Sonntag, C. Photolysis (λ = 254nm) of tetrachloroethene in aqueous solutions. *J. Photochem. Photobiol*., 1995, 85, 1-9.

43. von Sonntag, C.; Schuchman, H.-P. Peroxyl radicals in aqueous solution. In *Peroxyl Radicals*; Alfassi, Z., Ed.; John Wiley & Sons: New York, 1997; pp 172-234.

44. Leitzke, A.; Reisz, E.; Flyunt, R.; von Sonntag, C. The reactions of ozone with cinnamic acids: formation and decay of 2-hydroxyperoxy-2-hydroxyacetic acid. *J. Chem. Soc., Perkin Trans*. 2, 2001, 793-797.

45. Schwarz, H. A. Reaction of the hydrated electron with water. *J. Phys. Chem*. 1992, 96, 8937-8941.

46. Maruthamuthu, P.; Padmaja, S.; Huie, R. E. Rate constants for some reactions of free radicals with haloacetates in aqueous solution. *Int. J. Chem. Kinet*. 1995, 27, 605-612.

47. Yu, X.-Y.; Bao, Z.-C.; Barker, J. R. Free radical reactions involving Cl•, Cl_2-•, and SO_4-• in the 248 nm photolysis of aqueous solutions containing $S_2O_8^{2-}$ and Cl^-. *J. Phys. Chem*. 2004, 108, 295-308.

48. Santos, L.C.; Poli, A.L.; Cavalheiro, C.C.S.; Neumann, M.G. The UV/H_2O_2 – photodegradation of poly(ethyleneglycol) and model compounds. *J. Braz. Chem. Soc*. 2009, 20, 1467-1472.

49. Santos, L.C.; Schmitt, C.C.; Poli, A.L.; Neumann, M.G. Photo-fenton degradation of poly(ethyleneglycol). *J. Braz. Chem. Soc*. 2011, 22, 540-545.

50. Aarthi, T.; Shaama, M.S.; Madras, G. Degradation of water soluble polymers under combined ultrasonic and ultraviolet radiation. *Ind. Eng. Chem. Res*. 2007, 46, 6204-6210.

51. Swift, G. Directions for environmentally biodegradable polymer research. *Acc. Chem. Res*. 1993, 26, 105-110.

52. Morlat, S.; Gardette, J.L. Phototransformation of water-soluble polymers. Part II: photooxidation of poly(ethylene oxide) in aqueous solution. *Polymer*. 2003, 44, 7891-7897.

53. Giroto, J.A.; Teixeira, A.C.S.C.; Nascimento, C.A.O.; Guardani, R. Degradation of poly(ethylene glycol) in aqueous solution by photo-fenton and H_2O_2/UV processes. *Ind. Eng. Chem. Res*. 2010, 49, 3200-3206.

54. Vijayalakshmi, S.P.; Madras, G. Photocatalytic degradation of poly(ethylene oxide) and polyacrylamide. *J. Appl. Polym. Sci*. 2006, 100, 3997-4003.

55. Guo, X.; Minakata, D.; Crittenden, J. Computer-based first-principles kinetic Monte Carlo simulation of polyethylene glycol degradation in aqueous phase UV/H2O2 advanced oxidation processes. *Environ. Sci. Eng.* 2014b, 48, 10813-10820.

56. Lin, C.C.; Lee, L.T.; Hsu, L.J. Performance of UV/S2O82- process in degrading polyvinyl alcohol in aqueous solutions. J. PhotoChem. Photobio. A. 2013, 252, 1-7.

57. Ulanski, P.; Bothe, E.; Hildenbrand, K.; Rosiak, J.M.; von Sonntag. Hydroxyl-radical-induced reactions of poly(acrylic acid): a pulse radiolysis, EPR and

product study. Part I. Deoxygenated aqueous solutions. J. Chem. Soc. Perkin Trans. 1995, 2, 13-22.

58. Janik, I.; Ulanski, P.; Hildenbrand, K.; Rosiak, J.M.; von Sonntag, C. Hydroxyl-radical-induced reactions of poly(vinyl methyl ether): a pulse radiolysis, EPR and product study in deoxygenated and oxygenated aqueous solutions. J. Chem. Soc. Perkin Trans. 2000, 2, 2041-2048.
59. Chang, C.Y.; Chen, Y.H.; Li, H.; Chiu, C.Y.; Yu, Y.H.; Chiang, P.C.; Ku, Y.; Chen, J.N. Kinetics of decomposition of polyethylene glycol in electroplating solution by ozonation with UV radiation. *J. Environ. Eng. ASCE.* 2001, 127, 908-915.
60. Ghafoori, S.; Mehrvar, M.; Chan, P.K. Kinetic study of photodegradation of water soluble polymers. *Iran. Polym. J*. 2012a, 21, 869-876.
61. Ghafoori, S.; Mehrvar, M.; Chan, P.K. Free-radical-induced degradation of aqueous polyethylene oxide by UV/H_2O_2: experimental design, reaction mechanisms, and kinetic modeling. *Ind. Eng. Chem. Res*. 2012b, 51, 14980-14993.
62. Vinu, R.; Levine, S.E.; Wang, L.; Broadbelt, L.J. Detailed mechanistic modeling of poly(styrene peroxide) pyrolysis using kinetic Monte Carlo simulation. *Chem. Eng. Sci*. 2012, 69, 456-471.
63. McDermott, J.B.; Libanati, C.; LaMarca, C.; Klein, M.T. Quantitative use of model compound information: Monte Carlo simulation of the reactions of complex macromolecules. *Ind. Eng. Chem. Res*. 1990, 29, 22-29.
64. Pinto, J.Q.; Kaliaguine, S. A Monte Carlo analysis of acid hydrolysis of glycosidic bonds in polysaccharides. *AIChE J*. 1991, 37, 905-914.

65. Platkowski, K.; Reichert, K. Application of Monte Carlo methods for modelling of polymerization reactions. *Polymer*. 1999, 40, 1057-1066.

66. Guo, X.; Minakata, D.; Niu, J.; Crittenden, J. Computer-based first-principles kinetic modeling of degradation pathways and byproduct fates in aqueous-phase advanced oxidation processes. *Environ. Sci. Technol*. 2014a, 48, 5718-5725.

67. Gillespie, D.T. Exact stochastic simulation of coupled chemical reactions. *J. Phys. Chem*. 1977, 81, 2340-2361.

68. Kaczmarek, H.; Linden, L.; Rabek, J.F. Reactions of hydroxyl (HO•) and hydroperoxyl (HO_2•) radicals generated chemically and photochemically with poly(ethylene oxide). J. *Polym. Sci. Polym. Chem.*1995, 33, 879-890.

69. McGinnis, B.D.; Adams, V.D.; Middlebrooks, E.J. Degradation of ethylene glycol in photo fenton systems. *Wat. Res.* 2000, 34, 2346-2354.

70. McCoy, B.J. Continuous-mixture kinetics and equilibrium for reversible oligomerization reactions. *AIChE J*. 1993, 39, 1827-1833.

71. Baignee, A.; Howard, J.A.; Scaiano, J.C.; Stewart, L.C. Absolute rate constants for reactions of cumyloxy in solution. *J. Am. Chem. Soc.* 1983, 105, 6120-6123.

72. Leitzke, A.; Reisz, E.; Flyunt, R.; von Sonntag, C. The reactions of ozone with cinnamic acids: formation and decay of 2-hydroxyperoxy-2-hydroxyacetic acid. *J. Chem. Soc., Perkin Trans*. 2, 2001, 793-797.

73. Behar, D.; Czapski, G.; Duchovny, I. Carbonate radical in flash photolysis and pulse radiolysis of aqueous solutions. *J. Phys. Chem*. 1970, 74, 2206-2210.

74. Bolton, J. R.; Cater, S. R. Homogeneous photodegradation of pollutants in contaminated water: an introduction, Chap. 33. *Aq. Surf. Photochem*. 1994, 0,

467-490.

75. Buhler, R. F.; Staehelin, J.; Hoigne, J. J. Ozone decomposition in water studied by pulse radiolysis. 1. HO2/O2- and HO3/O3- as intermediates. *J. Phys. Chem*. 1984, 8 (12), 2560-2564.
76. Christensen, H. S.; Sehested, K.; Corftizan, H. Reactions of hydroxyl radicals with hydrogen peroxide at ambient temperatures. *J. Phys. Chem*. 1982, 86, 15-88.
77. Crittenden, J. C.; Hu, S.; Hand, D. W.; Green, S. A kinetic model for H2O2/UV process in a completely mixed batch reactor. *Water Res*. 1999, 33 (10), 2315-2328.
78. Crittenden, J. C.; Trussell, R. R.; Hand, D. W.; Howe, K. J.; Tchobanoglous, G. Water Treatment Principles and Design, 3rd ed.; John Wiley & Sons. Ltd.: New York, 2012; pp 1415-1472.
79. DeMers, L.D. and R.C. Renner. Alternative Disinfection Technologies for Small Drinking Water Systems.; AWWARF and AWWA, Denver, CO. 1992.
80. Draganic, Z. D.; Negron-mendoza, A.; Sehested, K.; Vujosevic, S. I.; Navarro-Gonzales, R.; Albarran-Sanchez, M. G.; Draganic, I. G. Radiolysis of aqueous solutions of ammonium bicarbonate over a large dose range. *Radiat. Phys. Chem*. 1991, 38 (3), 317-321.
81. Elovitz, M. S.; Von Gunten, U. Hydroxyl radical/ozone ratios during ozonation processes. I. The RCT concept, *Ozone: Sci. Eng.* 1999, 21 (3), 239-260.
82. Glaze, W. H.; Kang, J.-W. Advanced oxidation processes. test of a kinetic model for the oxidation of organic compounds with ozone and hydrogen peroxide in a semibatch reactor. *Ind. Eng. Chem. Res*. 1989, 28 (11), 1573-1580.
83. Glaze, W. H.; Lay, Y.; Kang, J.W. Advanced oxidation processes. A kinetic

model for the oxidation of 1,2-dibromo-3-chloropropane in water by the combination of hydrogen peroxide and UV radiation. *Ind. Eng. Chem. Res*. 1995, 34, 2314-2323.

84. Kerwin, R. L. Ozone in Drinking Water Treatment - Process Design, Operation, and Optimization, 1st ed.; American Water Works Association (AWWA), 2005.
85. Lay, Y.S. Ph.D. dissertation. 1989.
86. Staehelin, J.; Hoigne, J. Decomposition of ozone in water: rate of initiation by hydroxide ions and hydrogen peroxide. *Environ. Sci. Technol*. 1982, 16 (10), 676-681.
87. Stumm, W.; Morgan, J. J. Aquatic chemistry: An Introduction Emphasizing Chemical Equilibria in Natural Waters; Wiley-Interscience: New York, 1981.
88. Westerhoff, P.; Mezyk, S. P.; Cooper, W. J.; Minakata, D. Electron pulse radiolysis determination of hydroxyl radical rate constants with Suwannee River fulvic acid and other dissolved organic matter isolates. *Environ. Sci. Technol*. 2007, 41 (13), 4640-4646.

VITA

Xin Guo

Xin Guo was born in 1987 in Taiyuan, Shanxi, China. He received a B.S. in Environmental Engineering School from Tsinghua University, China in 2010. His enthusiasm for research in environmental engineer led to his pursuing a Ph.D. in the School of Civil and Environmental Engineering at the Georgia Institute of Technology in Atlanta, GA in 2010.